Experimental Investigation of Relative Permeability Upscaling from the Micro-Scale to the Macro-Scale

Final Report

Reporting Period Start Date: August 8, 1999
Reporting Period End Date: August 15, 2003

Laura J. Pyrak-Nolte, Nicholas J. Giordano and David D. Nolte

March 2004

DOE Award: DE-AC26-99BC15207

Purdue Research Foundation
Department of Physics
1396 Physics Building, Room 166
West Lafayette, Indiana 47907-1396

Abstract: The principal challenge of upscaling techniques for multi-phase fluid dynamics in porous media is to determine which properties on the micro-scale can be used to predict macroscopic flow and spatial distribution of phases at core- and field-scales. The most notable outcome of recent theories is the identification of interfacial areas per volume for multiple phases as a fundamental parameter that determines much of the multi-phase properties of the porous medium. A formal program of experimental research was begun to directly test upscaling theories in fluid flow through porous media by comparing measurements of relative permeability and capillary-saturation with measurements of interfacial area per volume. This project on the experimental investigation of relative permeability upscaling has produced a unique combination of three quite different technical approaches to the upscaling problem of obtaining pore-related microscopic properties and using them to predict macroscopic behavior. Several important "firsts" have been achieved during the course of the project. 1) Optical coherence imaging, a laser-based ranging and imaging technique, has produced the first images of grain and pore structure up to 1 mm beneath the surface of the sandstone and in a laboratory borehole. 2) Woods metal injection has connected for the first time microscopic pore-scale geometric measurements with macroscopic saturation in real sandstone cores. 3) The micro-model technique has produced the first invertible relationship between saturation and capillary pressure—showing that interfacial area per volume (IAV) provides the linking parameter. IAV is a key element in upscaling theories, so this experimental finding may represent the most important result of this project, with wide ramifications for predictions of fluid behavior in porous media.

Table of Contents

List of Figures

Executive Summary

Direct experimental tests of upscaling theories in fluid flow through porous media will be made by comparing measurements of relative permeability and capillary-saturation with measurements of interfacial area per volume. These experiments are performed from the pore-scale (microns) to the core-scale (centimeters), spanning four orders of magnitude in size. Three experimental objectives provide the data for rigorous tests of upscaling theories. First, holographic laser imaging techniques will acquire pore-scale three-dimensional optical images of the pore geometry in reservoir sandstones. This technique uses unique properties of coherent light to see through drilling muds and into the sandstone. Second, laboratory micro-models with matched topological properties based on the data from the pore imaging will make it possible to measure interfacial area per volume in scientifically controlled imbibition and drainage experiments, combined with measurements of capillary-pressure-saturation data and relative permeability. Third, core-scale experiments of relative permeability and capillary-saturation, and metal casts of the pore geometry, will be compared with the pore-scale data of the first two objectives. The data from all these objectives will provide the first complete picture over such a large dynamic range. It will make it possible to answer the principal question concerning flow upscaling: which microscopic measurements are most useful for predicting macroscopic flow properties of an oil reservoir. The tangible outcome of this work will be explicit data connecting interfacial areas, or other relevant geometric micro-scale data, with macroscopic hydraulic properties. In addition, we show strong industrial interest in testing and commercializing the unique down-hole laser imaging technology that can be transferred to the oil-industry service-company sector.

During the course of this contract, the project on the experimental investigation of relative permeability upscaling has produced a unique combination of three quite different technical approaches to the upscaling problem of obtaining pore-related microscopic properties and using them to predict macroscopic behavior. Several important “firsts” have been achieved during the course of the project. 1) Optical coherence imaging, a laser-based ranging and imaging technique, has produced the first images of grain and pore structure up to 1 mm beneath the surface of the sandstone and in a laboratory borehole. 2) Woods metal injection has connected for the first time microscopic pore-scale geometric measurements with macroscopic saturation in real sandstone cores. 3) The micro-model technique has produced the first invertible relationship between saturation and capillary pressure—showing that interfacial area per volume (IAV) provides the linking parameter. IAV is a key element in upscaling theories, so this experimental finding may represent the most important result of this project, with wide ramifications for predictions of fluid behavior in porous media.

1.0 Introduction

1.1 Summary of Project Description

Standard expressions of multi-phase flow in porous media based on modifications of Darcy's Law (Darcy, 1856) have crippling deficiencies that make them undesirable to use for critical operations such as tertiary recovery of oil from depleted reservoirs. The primary difficulty in these empirical expressions are their violation of rigorous conservation laws. New theories based on rigorous volume averaging theorems and fundamental thermodynamic principles of phase boundaries have emerged in the past decade to replace the old empirical rules (Hassanizadeh and Gray, 1979; Gray, 1983). The most notable outcome of these theories is the identification of interfacial areas per volume for multiple phases as fundamental parameters that determine much of the multi-phase properties of the porous medium (Muccino et al., 1998).

Interfacial areas per volume provide natural descriptions of fundamental physical processes in porous media. For instance, thermodynamic energies are proportional to interfacial areas, and interfacial areas per volume represent a form of energy density. Gradients in energy densities define the dynamical pressures that drive the movement and distribution of phases within a complex topology. Interfacial areas per volume in a porous medium therefore represent a three-dimensional potential energy landscape.

Interfacial areas per volume also provide a natural yard-stick for defining the role of scale in multiphase fluid properties. The dimensional units of interfacial area per volume is a spatial frequency (inverse length) that breaks scale invariance. A useful illustration of this scale-defining role can be made by considering an image of a pore-geometry containing only a single phase. Without a measurement scale, it is impossible to state what the physical size of the system is. However, when two phases such as water and air are both present, the length scale becomes obvious. At small scales, the water-air interface is drawn into the pore throats, while at large scales the water puddles in the large void volumes.

Therefore, the interfacial areas between phases define a length scale. Whenever a physical system has an intrinsic length scale, the physics of the system can be divided into two regimes: one where sample sizes are larger than the intrinsic length scale, and the other where information is obtained on scales smaller than the intrinsic length scale. Breaking scale invariance makes it possible to define representative elementary volumes (REV) and to apply averaging theorems. Combining the averaging theorems with thermodynamics further constrains the possible types of constitutive equations that can rigorously describe multiphase fluid properties in porous media.

As a consequence of this theoretical framework, interfacial areas per volume (IAV) take on a more important role than simple volume saturation . This important role of IAV is clear because a single value of relative volume saturation can correspond to infinitely different distributions of two phases within the volume. Large values of IAV relate to a finely distributed phase that can block pore throats and seriously affect permeability, while small values of IAV relate to gross separations of phases, with large connected volumes of the phase that can flow unimpeded through the network. Significant numerical studies have been performed on the relationships between capillary-saturation and interfacial area. Reeves and Celia (1996) developed a numerical model that scans over repetitive imbibition and drainage while tracking the interfacial area for each loop. These studies pointed to a non-unique

relationship between interfacial area and partial saturation, although a family of curves did emerge that lies within a localized part of the parameter space defined by area and saturation.

The numerical studies illustrate the importance of continued and extensive experimental studies and tests of upscaling theories, and in particular tests of the role of interfacial area per volume in determining macroscopic flow properties. While oil recovery predictions should certainly include IAV as critical parameters, it is important to test whether other microscopic parameters also contribute to the macroscopic behavior. For instance, scale invariance of interfacial areas, even over restricted length scales, could present serious challenges to the averaging theorems, and could modify the presumed role of interfacial area in determining macroscopic flow properties. The principal objective of our proposed upscaling approach is to experimentally measure many microscopic geometric parameters of the flow system over many scales, and connect these microscopic measurements with macroscopic flow behavior.

1.2 PROJECT OBJECTIVES

The proposed work for this contract has three objectives that will provide rigorous experimental tests of upscaling theories. The objectives are:

1) To use holographic laser imaging techniques to acquire pore-scale three-dimensional optical images of the pore geometry in reservoir sandstones. This technique uses unique properties of coherent light to see through drilling muds and up to a millimeter into the sandstone. This data forms the basis of upscaling experiments to test theories of interfacial area per volume.

2) To construct laboratory micro-models with matched topological properties based on the data from the pore imaging. Interfacial area per volume will be measured directly in controlled imbibition and drainage experiments, together with capillary-pressure-saturation data and relative permeability data. This set of interrelated data will allow rigorous testing of upscaling theories.

3) To perform core-scale experiments of relative permeability and capillary-saturation, and to make metal casts of the pore geometry and interfacial area per volume. This core-scale data (including pore-scale from the metal casts) will be compared with the pore-scale data of the first two objectives, extending the observation scales over four orders of magnitude.

2.0 Experimental

2.1 Optical Coherence Imaging

The experimental procedures and equipment for this component of the accomplished research consist of the fabrication and characterization of holographic film, called photorefractive quantum well (PRQW) devices, and the establishment of a coherence-domain holographic imaging optical system for obtaining volumetric data on the sand grains and pores of sandstone.

2.1.1 Sample Preparation of Photorefractive Quantum Well Devices

Optical Coherence Imaging (OCI) requires high optical quality Multiple Quantum Well (MQW) devices. New sample preparation techniques were developed as part of the work for this contract. The following is a summary of the six major steps in fabrication: dicing, device/glass slide bonding, mechanical lapping, chemical etching, flashing, and contacting. The PRQW devices begin with molecular-beam epitaxy growth. The growth structure is shown in Figure 2.1.1. The quantum wells used in this project were grown, via Molecular Beam Epitaxy (MBE), by either Dr. M. R. Melloch of the Electrical Engineering Department at Purdue University, or an external company QED. The growth is done on undoped GaAs 3" wafers.

2.1.1.1 Dicing

After growth, the wafer is diced into small pieces, typically 2mm by 7 mm. The actual size, however, depended on the desired optical area of the device. No major changes were made to the previous methods of dicing up the wafer. A small change was made in hopes to reduce any possible damage to the devices during the substrate-to-glass side bonding. Any material cleaved is blown off with canned air to prevent scratches from the debris of previous cuts with future ones..

GaAs	**200 Å**	**Cap**
$Al_{0.2}Ga_{0.8}As$	**2000 Å**	**Buffer Layer**
100 period superlattice **70Å GaAs /50 Å $Al_{0.3}Ga_{0.7}As$**		**MQW Superlattice**
$Al_{0.2}Ga_{0.8}As$	**2000 Å**	**Buffer Layer**
GaAs	**100 Å**	**Cap (For Post Processing)**
AlAs	**200 Å**	**Flash Layer**
$Al_{0.5}Ga_{0.5}As$	**5000 Å**	**Stop Etch Layer**
GaAs	**5000 Å**	**Buffer Layer (MBE)**
GaAs **Q032299**	**625 μm**	**Substrate**

Figure 2.1.1 The semiconductor growth layers for the molecular-beam epitaxy of PRQW devices.

2.1.1.2 Device/Glass Slide Bonding

After the wafer was diced into usable portions, the substrate was attached to a one millimeter thick glass slide that has been cut into a one inch by ~3/4 inch piece. The side of the substrate with the MBE grown quantum wells (called the device) was glued to the slide using an optical epoxy. Several major changes were made to this step of the fabrication.

The epoxy used previously was a two part optical epoxy. It was noticed that, upon mixing the epoxy, small bubbles would become trapped within the mixture. This creates two serious problems. One is that the bubbles, due to the index mismatch of the epoxy (n=1.54) with air causes a scattering center. The other is that when fabrication is completed, these bubbles may be pushing out on the one-micron thick device causing the device to flake off in that region. A solution to this problem had two parts. First, the epoxy was heated in an 85°C oven for approximately five minutes. The heating reduces its viscosity so that upon mixing with the hardener any trapped bubbles are allowed to float to the surface and ultimately freed from the mixture. Then the mixed epoxy was placed in a desiccator for several minutes in an attempt to outgas any remaining bubbles. This solution seems to have worked because no trapped bubbles have been observed nor has any flaking of devices been seen since its use.

Even though improvements have been made to the usage of the epoxy above, a new one part epoxy was also investigated. It is made by Norland (part number 83H) and distributed by Edmund Scientific. Being a one-part epoxy, no mixing is required and is therefore less prone to problems with bubbles. Also, its curing time is ten minutes in a 125°C oven versus 1.5 hours in an 85°C oven for the two-part epoxy. Thus far the epoxy has met with good results. It adheres well to the glass slide and performs well under lapping and chemical etching. It does have two small, but surmountable issues. It is difficult to get the desired amount of epoxy from the applicator bottle. Usually too much is administered which causes lapping times to increase.

One last improvement was made to the bonding step of fabrication. Previously, the epoxy was placed on the glass slide and then the substrate was pressed onto the slide with tweezers. A rotating motion was done to displace as much epoxy as possible between the slide and substrate. Also, the motion seemed to help remove any bubbles that may have become trapped. The problem with the rotating motion was that any type of debris on the order of a micron that may have made its way into the epoxy would scratch the surface and ruin the optical quality of the device. The current method is to initially place the device at an angle in the epoxy and then push down without using a rotating motion. As the device is pushed down, the epoxy escapes from one end. This method has met with good results. No scratches or bubbles have been seen since this method was introduced.

2.1.1.3 Lapping

After the epoxy is allowed to cure, the devices are lapped to remove all but the last one hundred microns or so of the substrate. Several key changes were made in this step. The first was the attachment of the device to the lapper. Previously, materials such as black wax were used to make the attachment. However to attach and remove the device it was necessary to heat it. For attachment purposes this poses no problem. For removal purposes this could be disastrous. At less than one hundred microns thick the device may become susceptible to cracking during heating and thus ruin the device both optically and electrically.

The new method for attachment is to use double-sided transparent tape. The tape does an excellent job of holding the device to the lapper during lapping. Also, by holding the lapper under running water while gently prying, the device comes off easily. This method has solved several problems seen in the past such as scratches to the glass caused by the wax.

A second method was implemented due to problems seen in the following step of fabrication. The chemical etch would become anisotropic especially near the edges of the device. This problem is discussed in the next part. It was found that if the devices were lapped down to a thickness of 50-70 microns instead of the previous limit of 100-130 microns that the anisotropy of the etch was greatly reduced or eliminated altogether. There is a problem of lapping too far in that as the device gets thinner, the greater the risk of strain-induced cracking. However no evidence of cracking has been seen on devices that have been lapped to the smaller thickness.

2.1.1.4 Chemical Etch

Once the devices have reached the desired thickness, they are subjected to a chemical etch to remove the remaining substrate. This is the most critical step of fabrication. Many if not all device fabrication failures originate in this step. One major problem occurs in this step. Substrate is being left along the edges of the device. If this remaining substrate spans the two contacts, a short is incurred which may destroy the device once a field is applied. Attempts at allowing the device to stay in the etch longer to remove all of the substrate once the AlGaAs stop-etch layer has been reached have not worked. The stop-etch layer only slows the etch and is not thick enough to sustain prolonged periods in the etch. The result is the overetching of the device into the quantum well layer. It is felt that the anisotropy of the etch near the edges is due to the lip created by the epoxy as the device is etched. By lapping the device more, less of a lip is left as the device etches. Also, since there is a lifetime of 30-45 minutes on the etch, a thinner device etches quicker and therefore takes most advantage of the isotropy of the etch.

Another method was implemented in conjunction with the extra thinning of the devices. A magnetic stirring bar was added to the etch to increase the etchant movement over the devices, especially along the edges. However, the most notable improvement thus far has been to change the thickness of the devices.

2.1.1.5 Flash

Once the remainder of the substrate has been removed, the devices are placed into a hydroflouric acid bath to remove the remainder of the stop-etch layer which finally yields a high optical quality planar surface. The problem with using hydroflouric acid is that it attacks glass. Therefore the glass slides that the devices are mounted on must be protected. A new method of protection has been investigated. Gel-Pak Inc. sells a gel film that adheres to glass and glasslike materials but can be removed without the use of solvents.

Previously, the slides were encapsulated in black wax. The only way to remove the wax once the flash had been achieved was to use toluene. Unfortunately this leaves a residue on the surface of the device that is difficult to remove. Thus the optical quality of the device suffers,not to mention the problems the residue may cause the contacts. Thus this new film removes the need for the use of the black wax.

Several issues emerged with the use of the gel film. The first is that the top surface of the glass is not covered so that it is etched. Since this side is not necessary to device performance, this problem may be inconsequential. The second is that with the top surface unprotected, the acid attacks the epoxy. The result is that the epoxy peels off around the device. The device and the epoxy under the device seem to be unaffected. One problem that is encountered is that as the device is dried off after rinsing, some debris of the epoxy will deposit itself upon the device surface. An acetone wash with a methanol rinse has solved this problem. Device surfaces are now becoming comparable to the quality of the surface of the wafer prior to fabrication.

2.1.1.6 Contacts

The final step in fabrication is the deposition of contacts upon the devices. Only one real change was made during the proejct. A cleaner, higher vacuum evaporator is now used over an older model. Currently gold is being used for the contacts. The device masked prior to gold deposition is shown in Figure 2.1.2a, and the finished device is shown in Figure 2.1.2b. The PRQW device is mounted in an electrically insulating box, shown in Figure 2.1.3, for save use under the high voltage (up to 1 kV) typically used in the application.

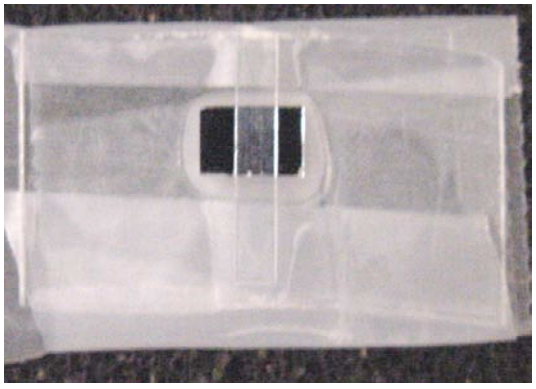

Pre-contacted device with transparency film mask

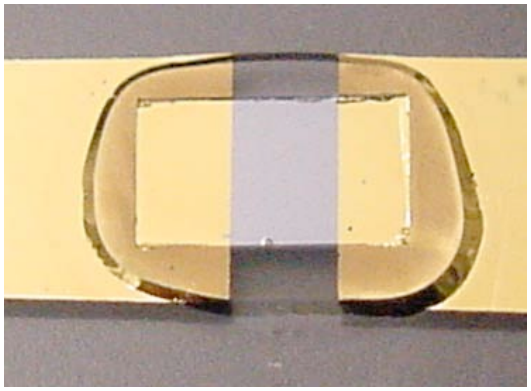

Post-contacted device (2 mm window)

Figure 2.1.2 Metallization of the PRQW devices. (a) on left shows the mask prior to metallization. (b) on right shows the finished device with gold contact and a 2 mm window.

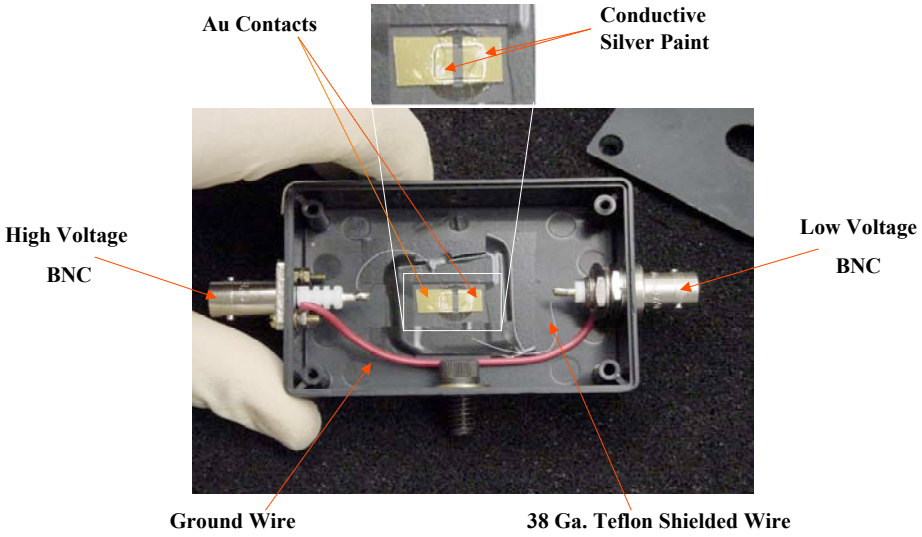

Figure 2.1.3 PRQW device mounted in a case. The box is electrically isolating ensuring safe use when high voltage (up to 1000 Volts) is applied.

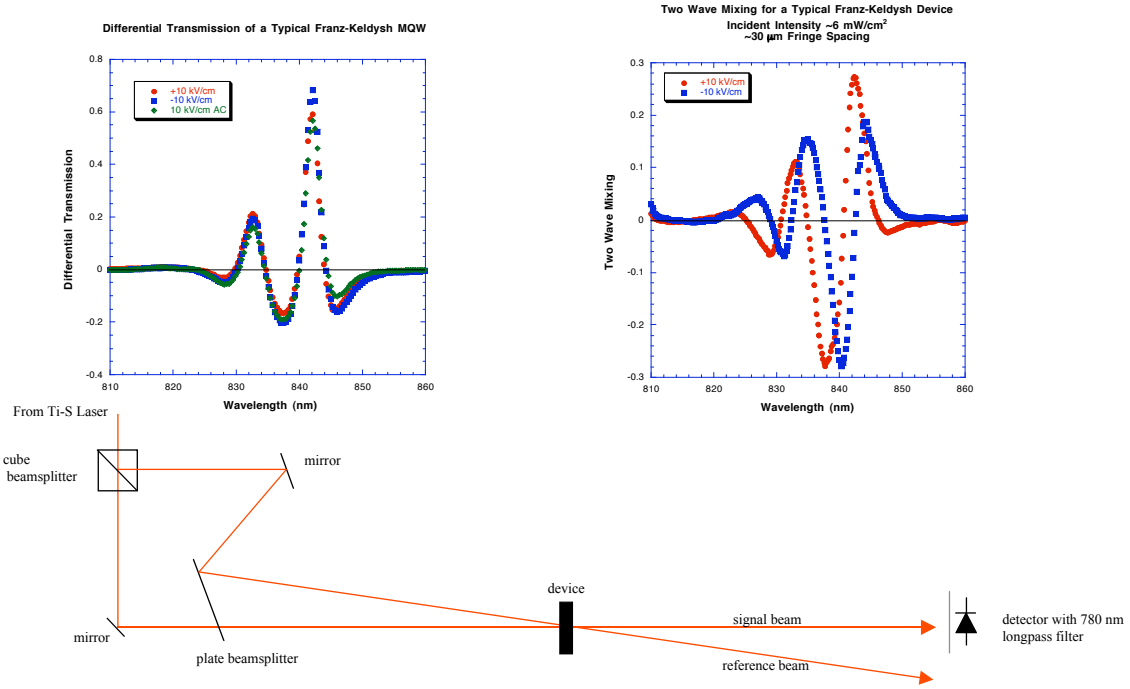

Figure 2.1.4 Characterization of the PRQW device showing electroabsorption a), two wave mixing b), and the optical set-up for two-wave mixing c).

2.1.1.7 CHARACTERIZATION

After mounting, the devices are characterized for electro-absorption, also known at differential transmission, shown in Figure 2.1.4a. Differential transmission over 40% is

considered to be excellent. The ability of the devices to perform as holographic films is characterized using two-wave mixing, shown in Figure 2.1.4b. Two-wave mixing above 25 percent is considered excellent. The optical set-up for two-wave mixing is shown in Figure 2.1.4c.

2.1.2 Experimental Set-up for Imaging on Sandstone Samples

A significant effort was centered on the development of the optical setups. Because holographic optical coherence imaging into sandstone had never been accomplished prior to this project, new experimental approaches and techniques were required. The optical systems went through many iterations with continuous improvement throughout the course of the project. The final systems were highly optimized for the acquisition of laser ranging data from at least 1 mm deep in sandstone.

Two separate optical systems were developed: Volumetric and Point-scan. The volumetric imaging acquired data volumes from regions with volumes of approximately 1 mm^3. The volumetric system used free-space optics and imagine. The point-scan acquired laser ranging data (A-scans) from a single point on the sandstone to a depth of approximately 1 mm. The point-scan system used a commercial borescope.

2.1.2.1 Optical Set-up for Volumetric Imaging of Sandstone

An Optical Coherence Imaging (OCI) system was developed for this project to image into the sandstone. The OCI system (Figure 2.1.5) consists of a mode-locked Ti:sapphire laser (120 femtoseconds (fs) pulses with 100 MHz repetition rate), a modified Mach Zehnder interferometer with a sample arm and a reference arm, and a photorefractive multiple quantum well (PRQW) device[Nolte, 1995] that is the dynamic holographic film. An electric field (DC 10 kV/cm) is applied in the plane of the device. This configuration is called the transverse-field geometry that uses the Franz-Keldysh effect. In the interferometer, a de-magnified telescope (4:1) is used in the detecting arm that decreases the beam diameter to 1.0 mm on the sample. As a result, the intensity increases about 16 times at the sample. Two lenses with the same 150 mm focal length are separated by twice the focal length to form a 4-F system prior to the PRQW device (Figure 2.1.6).

In this 4-F system, the sample is placed at the focal plane in front of the first lens and the PRQW device is placed at the focal plane in back of the second lens (Figure 2.1.6). The plane that is halfway between the lenses is called the Fourier plane or the transform plane. The 4-F system projects a 1:1 image of the sample onto the holographic film. A spatial filter is located at the Fourier plane of the 4-F system to reject part of the scattered light from the sample, and allow the ballistic components to travel to the device. The signal beam interferes with the reference beam when the optical path lengths between the signal and reference arms are matched to within a coherence length of the laser by adjusting the translation stage in the reference arm. The interference fringes are imprinted onto the holographic film. The holograms are reconstructed using a degenerate four-wave mixing configuration. The first-order diffracted signal from the reference beam is imaged onto the surface of a cooled CCD camera (RTE/CCD 1317, Princeton Instruments) with a 150 mm focal length lens, while an aperture is used to cut off the zero order beam. The efficiency of the four-wave mixing is

optimized by adjusting the wavelength and bandwidth of the laser, the size and position of the aperture, and the relative intensities between the signal and reference beams.

To obtain information from deep in the sandstone, the system must be sensitive enough to acquire weak images under highly incoherent background. According to our theoretical analysis, the intensity of the first-order diffraction used to get a hologram in degeneration four-wave mixing can be increased by increasing the reference intensity. However, two limitations must be considered in the experiments when increasing the reference intensity. The first limitation is related to the Joule heating limit of the PRQW device that limits the total intensity on the device. We measured the Joule heating limit intensity to be about 90 mW/cm^2 for the device used in this project. In the experiments during this work period, a total intensity of 60 mW/cm^2 was used. The second limitation is the saturation of the cooled CCD camera caused by scattered light from the edges of the device and scattering defects in the device itself. To reduce the effect of the second limitation, the signal beam can be positioned on the device in regions with fewer scattering defects and edge effects. The signal beam has a diameter of about 0.5mm on the 1.0 mm device. The location of the signal beam can be selected using the region of interest (ROI) function of the cooled CCD camera. With this arrangement, uniform illumination across the entire device window can be achieved.

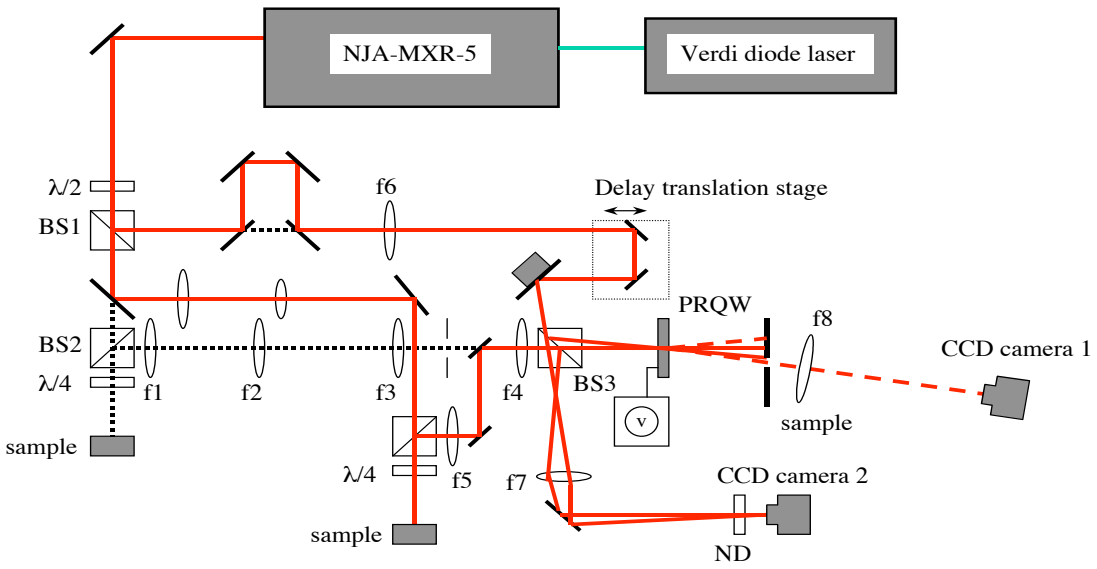

BS1, BS2: polarization beam splitter. BS3: 50/50 beam splitter.
f1=200mm, f2=100mm, f3=150mm, f4=f5=150mm, f6=500mm, f7=50mm, f8=150mm.
ND: Neutral Density Filter

Figure 2.1.5 The design and modifications of optical coherence imaging. The solid lines represent the modified setup and the dash lines are from the original setup.

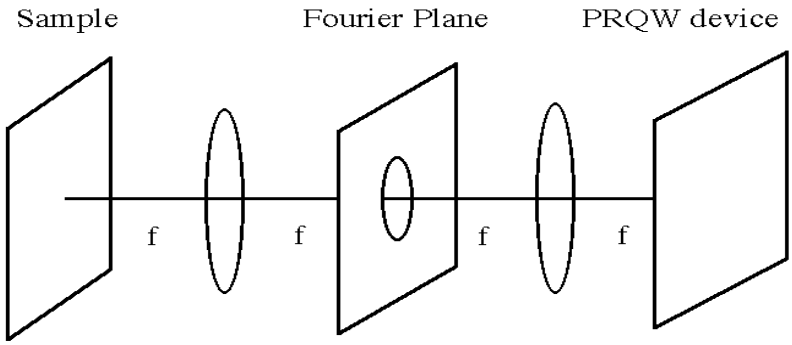

Figure 2.1.6 Two lenses form a 4-F configuration to get a 1:1 image between the sample and PRQW device.

The orientation of the sandstone sample in the OCI setup is shown in Figure 2.1.7. We define a coordinate system in the sample where each acquired image is located in the x-y plane and cross-section holograms that are reconstructed from the 3D data cube are in the x-z plane. The input femtosecond laser propagates in the z direction.

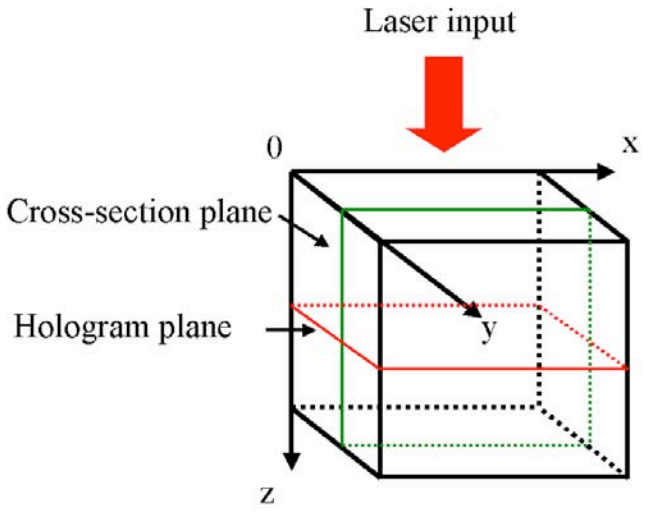

Figure 2.1.7 Orientation of sample and measurement. The image frames are xy, acquired at succesive depths z.

2.1.2.2 Optical Set-up for Point Scanning in a Synthetic Borehole

Work during this reporting period included the design and fabrication of an Optical Coherence Imaging device that uses a borescope. A borescope is traditionally used in

medicine to examine tissue that is accessible through human orifices (e.g., the lining of the esophagus). One of the objectives of this project is to determine if OCI can be developed to work through a borescope to image sandstone grains in borehole walls in the field (e.g., in oil and gas wells). As the first step toward this objective, we measured the electric field cross correlation by using a borescope in the signal arm of a low coherence interferometer. This measurement is similar to optical coherent tomography (OCT). The electric field cross correlation will give depth information of a translucent sample by the change in optical delay in the interferometer. In the sample, each dielectric discontinuity produces an optical "echo" through coherent backscattering. The results will provide parameters for the OCI.

The borescope setup consists of a low coherence light source, a modified Mach-Zehnder interferometer, and a borescope (Figure 2.1.8). A diode laser pumped self-mode-locked Ti:sapphire femtosecond laser is used as the low coherence light source. The main input beam is vertically polarized using a half-wave plate, so that it fits the Brewster window inside the borescope. The intensity in the signal beam after the borescope is 3 times as compared to the one with horizontal input polarization. A 10% beam splitter is used to divide the main beam into signal and reference. The borescope is placed in one arm of the interferometer and a delay stage controlled by a step motor is in the other arm. The interference from the signal arm and reference arm can be observed only when the path lengths of theinterferometer arms are matched to within the coherence length of the laser. The borescope can guide images from a long working length using a relay lens to reach inside tight working places such as a borehole (figure 2.1.9). A 80mm lens is used in front of borescope so that the output beam from the borescope to the sample is almost collimated. Two mirrors in the reference beam are used to overlap the reference beam with the signal beam. When a mirror is placed at the sample position, ring fringes are formed which are monitored by a CCD camera.

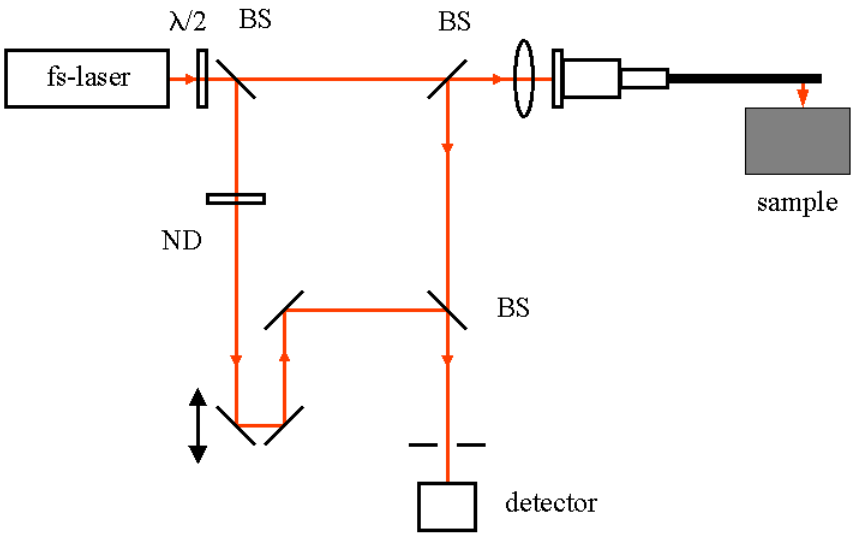

Figure 2.1.8 Experimental setup of optical coherent detection using a borescope. BS: beam splitter. ND: neutral density filter.λ/2: half wave plate.

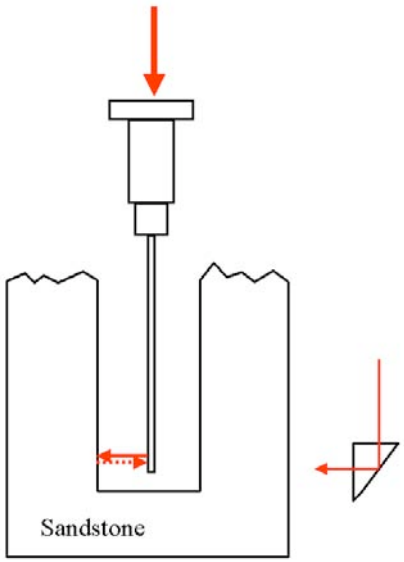

Figure 2.1.9 Schematic drawing of the borescope.

The electric field cross-correlation signals are measured by using a photoreceiver (Newfocus 1801) and a lock-in amplifier. During measurements, a pinhole is placed at center of the ring fringes. Since the signal intensity is very weak for most cases, a chopper is placed in the reference arm for lock-in detection. The time constant of the lock-in is selected to be faster than the time required for the movement of each step in the step motor. Depending on the signal beam intensities, different neutral density filters (NDs) are used in the reference arm in order to get the best modulation depth in the fringes.

The laser profile is monitored using a monochromator. The pulse with a wavelength profile of Gaussian shape is used in the electric field cross-correlation (Figure 2.1.10). Since we are doing non-adaptive homodyne detection, we need to consider the problem of laser speckle. The speckles from a filter paper are collected at the detection position with a CCD camera. The size of the pinhole is set to be large enough to cover several speckles of the signal beam figure 2.1.11.

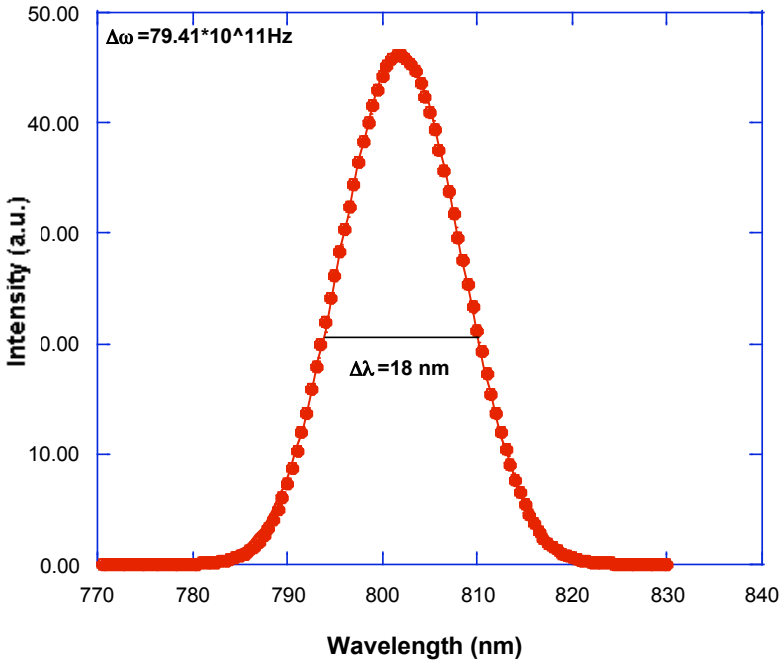

Figure 2.1.10 Laser profile measured by a monochromator.

Figure 2.1.11 Laser speckles and pin hole.

2.1.2.3 Optical Set-up for OCI in a Synthetic Borehole

In addition to point-scanning in a borehole, volumetric imaging of a region of a borehole was performed using OCI. The experimental set-up for performing OCI in a borehole is the same as that shown in Figure 2.1.15 except for the following modifications: off of beam splitter BS2, a bending mirror was placed between the quarter-wavelength plate and the sample. This modification diverted the beam to the sample with the borehole (Figure 2.1.12). The only piece of equipment sitting in the borehole is a mirror. To scan different depths along the borehole wall, the sample was placed on a translation stage and moved between images. If this was developed for field use, a device would have to be made to lower the optics into a borehole.

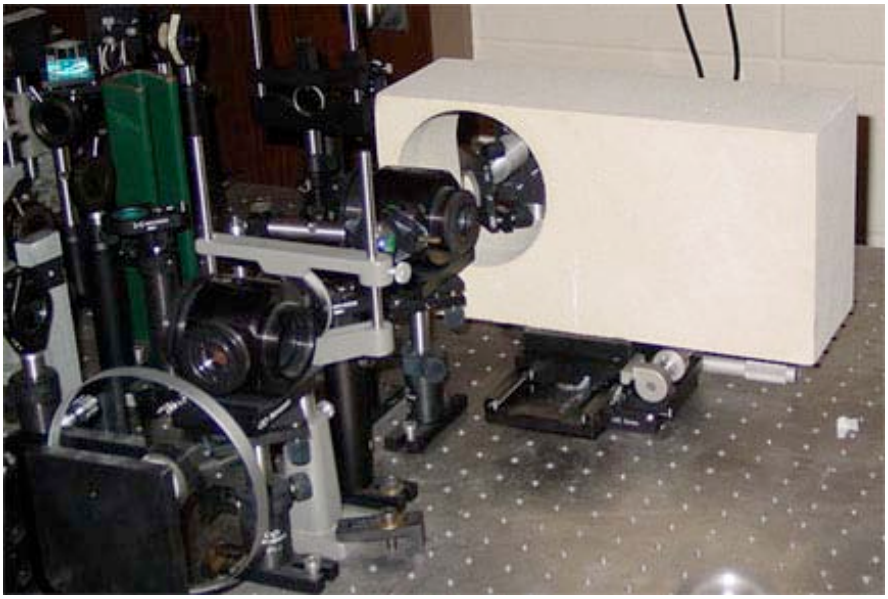

Figure 2.1.12 OCI set-up for volumetric imaging of a mock borehole in sandstone.

2.2 Micro-Model

2.2.1 Sample Preparation

This section gives a description of the procedures for performing optical lithography; complete details are given in the manufacturer's manual (Shipley, 1982) and by Thompson, Willson and Bowden (1994).

In optical lithography a pattern is transferred using a visible light image to a photo-sensitive polymer layer called photoresist. This layer acts essentially as photographic film. When a region of the photoresist is exposed to a sufficiently large integrated intensity of blue light, a photochemical reaction within the photoresist makes the region soluble in a special developer solution (usually just a base). The unexposed photoresist is not soluble, so after development the photoresist layer contains a negative image of the original light pattern. In all of our work we have used Shipley photoresist types 1805 and 1827, and their standard developer (Shipley, 1982). The image has been transferred to the photoresist in two different ways. In one method (Figure 2.2.1, left) a photomask is put in direct contact with the photoresist and the exposing light is transmitted through the mask. This mask is typically an

opaque metal layer on a glass substrate, or a small portion of an ordinary video transparency sheet onto which the appropriate pattern has been printed. With this contact configuration the mask pattern is transferred in a 1:1 fashion to the photoresist sample; i.e., without magnification or reduction in size. We use this method for making the coarse (i.e., largest scale) features of the micro-models. The smallest sample features are made by projecting the mask pattern onto the photoresist through a microscope objective. We employ a specially modified optical microscope which enables the image of the mask to be focused onto the sample at the same time as the sample is in focus to the observer. Projecting through a 50x objective yields a 50:1 reduction in the size of the image relative to the scale of the mask. In this way we can routinely achieve sub-micron feature sizes at the sample.

Construction of a complete micro-model involves several steps (Figure 2.2.2). The first is to transfer the pattern of the desired flow geometry into a photoresist layer – this is accomplished using optical lithography as just described. The resulting glass substrate/photoresist layer will form the bottom and sidewalls of the final micro-model. The top wall (ceiling) of the micro-model is formed by a second glass coverslip. This "top plate" is bonded to the bottom layer using another layer of photoresist – this bonding is accomplished by bringing the two glass coverslips into contact with gentle pressure (approximately 1 atm, applied in a special holder in which a flexible plastic sheet is pulled against the sample by an applied vacuum) immediately after application of photoresist to the top plate (Figure 2.2.2a). The top plate also contains two holes (approximately 1 mm in diameter, drilled ahead of time) that serve as inlet and outlet for the finished micro-model (Figure 2.2.2c). The inlet and outlet regions are fairly open spaces (approximately 4 mm on a side) on the micro-model, and contain "pillars" which are approximately 0.5 mm in diameter to prevent collapse of the structure (Figure 2.2.2b). The working region of the micro-model is the area labeled as "channel" in Figure 2.2.2b. This is where a percolative pattern is created in the bottom photoresist layer.

2.2.2 Flow Measurement Apparatus

A schematic of the flow measurement apparatus for the micro-models is shown in Figure 2.2.3. This apparatus is used for simultaneous measurements of flow rate and optical characterization of the geometries of the various phases within the sample. This apparatus contains (1) two pressure sensors to monitor the input and output pressures, and (2) a video camera interfaced to an optical microscope to image the two-phase displacements experiments.

To perform a flow measurement on a micro-model, the micro-model is initially saturated with a fluid decane, which is inserted through the "outlet" region in Figure 2.2.3. A second fluid, nitrogen gas, is then introduced through the inlet region. The displacement of the first phase by the second phase is measured using video microscopy. The measurement of IAV(interfacial area per volume) is accomplished with our video microscopy setup. For this we capture the image of the micro-model and do image processing with the computer interfaced to the camera. The captured image is processed using thresholding techniques to determine the areas occupied by both fluids (i.e., fluid saturation) and the interfacial area. All measurements are conducted at room temperature (temperature stability better than 0.5 degree Celsius during a measurement), with the apparatus located within one of the clean bench environments.

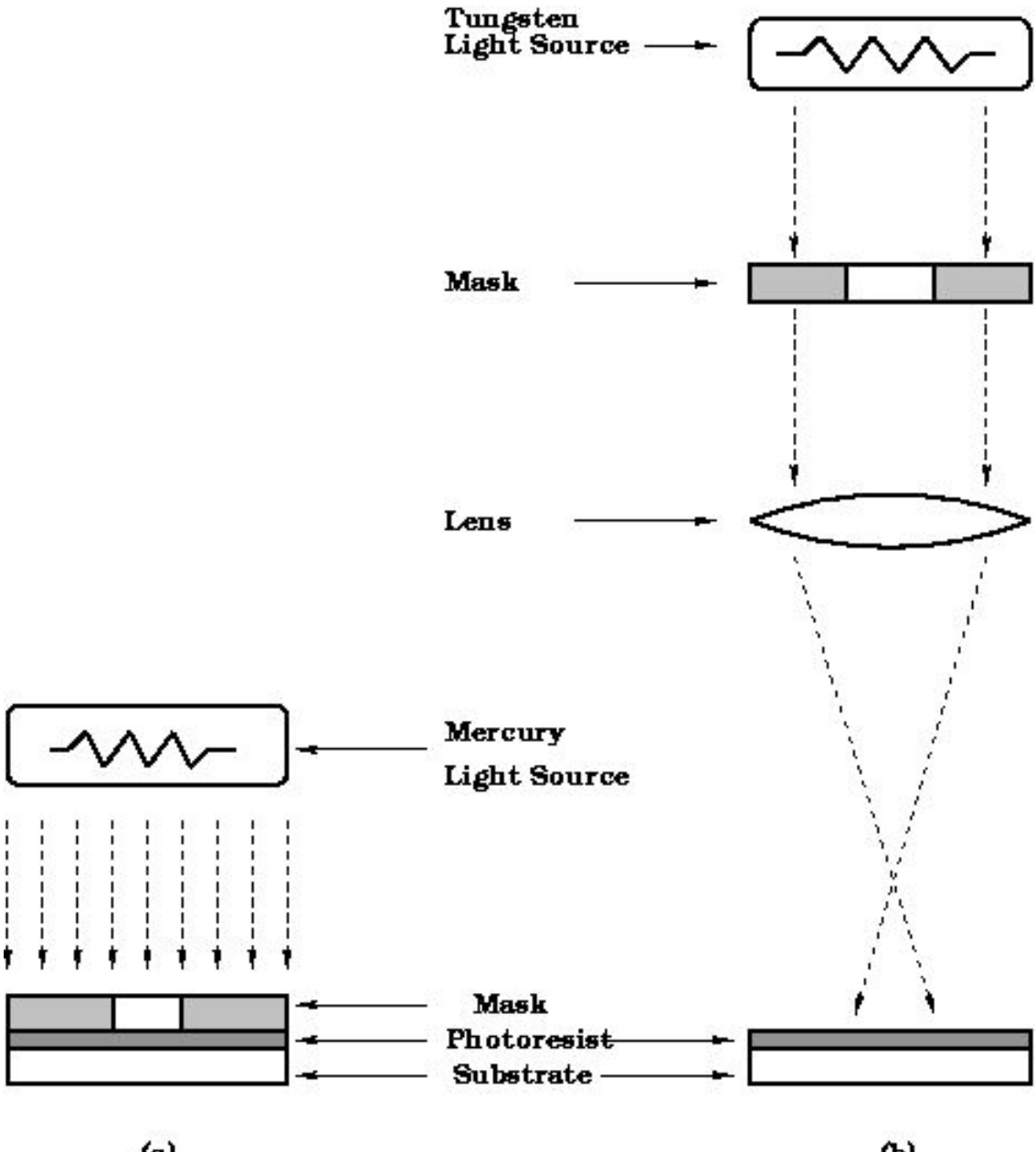

Figure 2.2.1. Schematics of the procedures used for optical lithography. Left: contact lithography. Right: projection lithography.

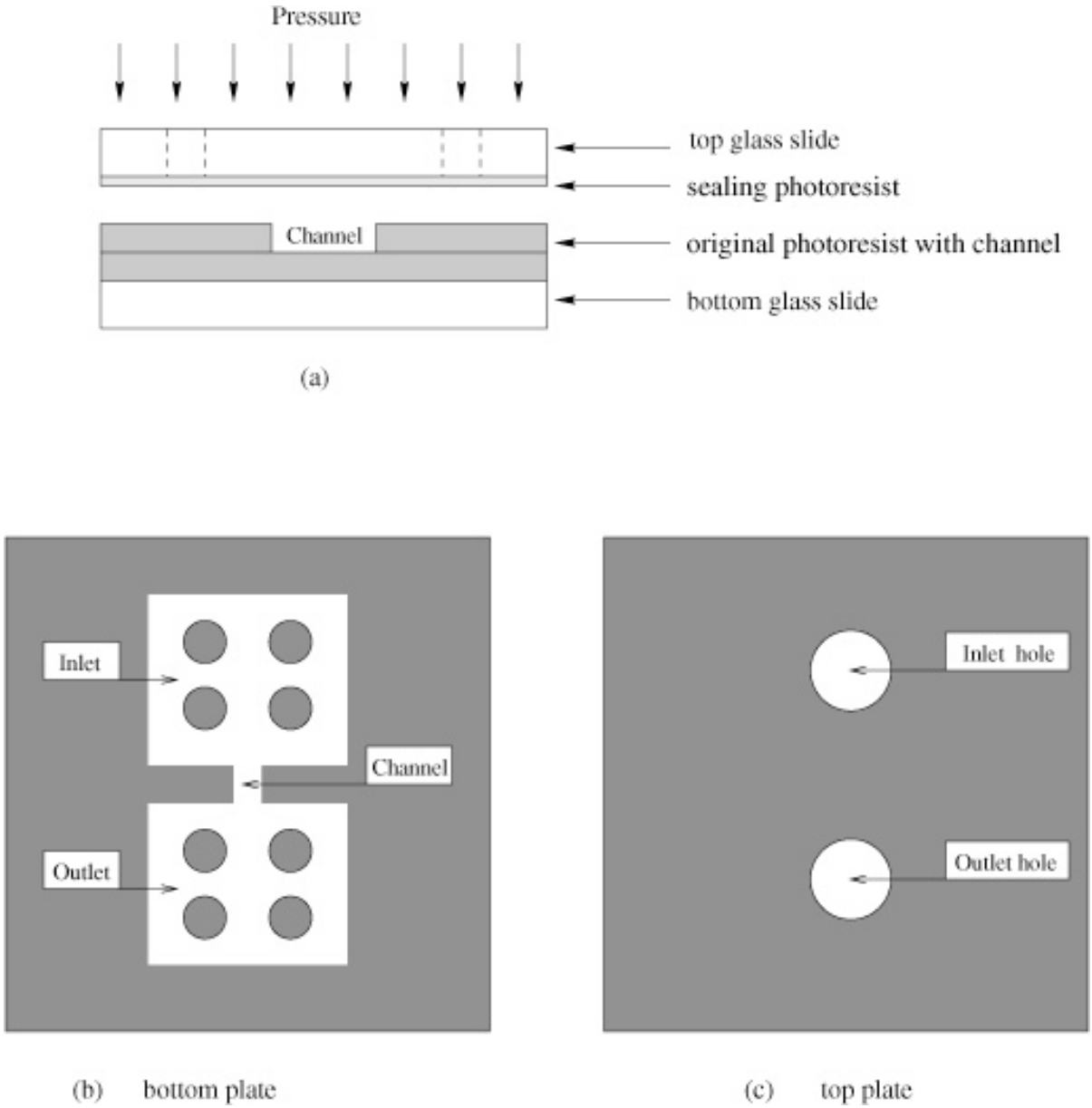

Figure 2.2.2 Micro-model layout. (a) Side view showing bottom plate containing micro-model pattern and top plate just prior to bonding. The glass slides are cover glasses 200 microns thick. The photoresist layers are 0.5 micron (type 1805 photoresist) and 2.7 microns (type 1827 photoresist). (b) Arrangement of inlet, outlet, and sample (channel) regions. (c) Inlet and outlet holes are drilled in the top plate.

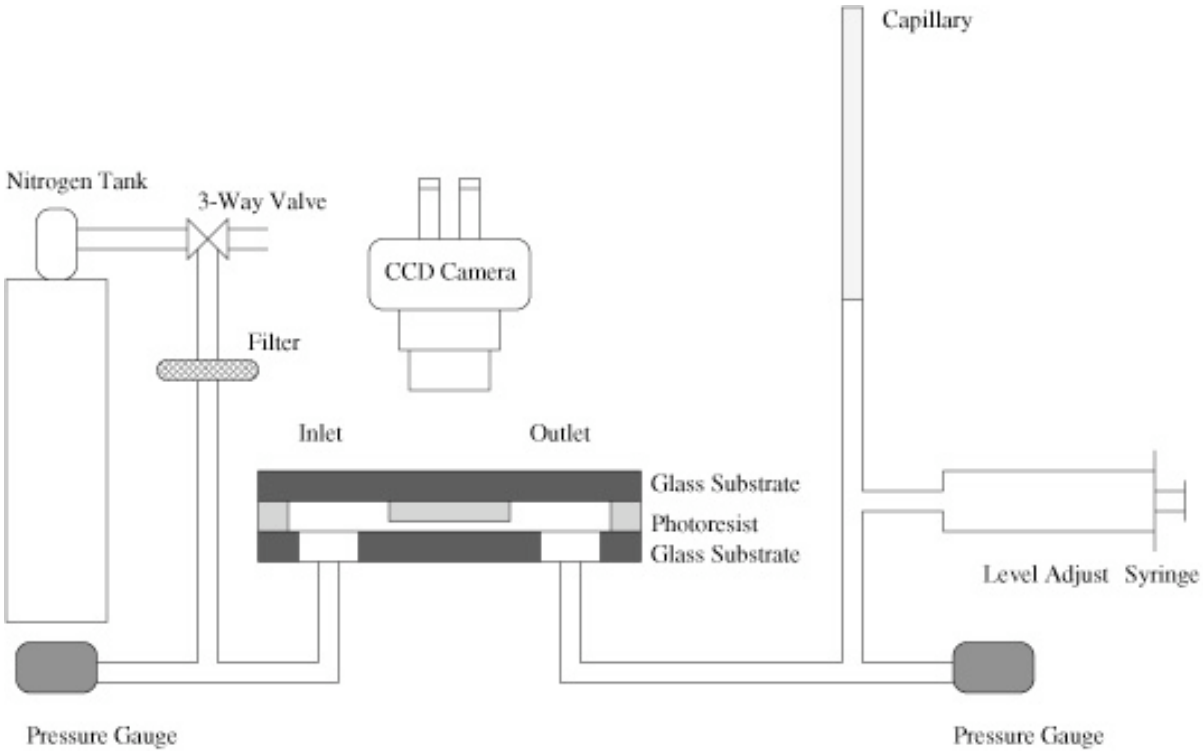

Figure 2.2.3. Apparatus used for measurement of flow rates and imaging of fluid geometry within a micro-model. The pressure sensors are piezoelectric sensors (model PX550C1 from Omega Engineering). The video camera system is a SPOT-1 RT color system (Diagnostic Instruments, Inc.) interfaced to a Macintosh G4 computer.

2.3 Wood's Metal Injection

2.3.1 Sample Preparation Procedure

2.3.1.1 Sample Preparation for Injection & Flow Measurements

For the measurement of absolute flow rate and for the Wood's metal injection experiments, whole core samples from blocks of sandstone are used. The samples are cored to a diameter of 52 mm and have a length of 25 mm or 100 mm. The short samples (25 mm in length) are used for low-injection pressure experiments to obtain equilibrium in a reasonable time. The samples are coated with epoxy. The purpose of the epoxy is two-fold. First, the epoxy is used to increase the diameter of the sample by 52 mm to provide a competent sealing surface. The second purpose of the epoxy coat is to seal the surface pores of the sample to prevent dominant flow paths forming along the surface of the sample. The procedure for applying the epoxy coats includes: (a) applying a thin layer of epoxy to the surface the sample and letting the thin coat of epoxy harden; (b) placing the thinly coated sample in the center of a tube with a diameter of 104 mm; and (c) filling the remaining space in the tube with more epoxy and letting the epoxy harden. Measurement of the sample porosity is made prior to and after coating with epoxy using a wet/dry method.

2.3.1.2 Sample Preparation for IAV Measurements

After the sample has been injected and post-injection flow measurements have been made, the sample is destructively examined to obtain information on porosity, saturation of the sample with Wood's metal, and interfacial area per volume (IAV). The Wood's metal injected sandstone core is flushed with isopropyl alcohol to remove any remnant ethylene gylcol in the sample. The flushed sample is heated in the oven at a temperature of 54 ºC for several days to evaporate the any remnant isopropyl alcohol. Then, the central portion of the sample is used for the investigation of IAV. The long samples are cut to a 25.4 mm by 25.4 mm by 100 mm rectangular prism, and then sectioned into 4 pieces measuring approximately 25.4 mm by 25.4 mm by 25.4 mm (Figure 2.3.1). The short samples are cut to a 25.4 mm by 25.4 mm by 25.4 mm cube. The size of the sample is controlled by the sample holder of the Scanning Electron Microscope (SEM). After cutting of the sample to the required size, the surfaces (perpendicular to the global flow direction during injection) of the four sections are polished on a polishing wheel (15 micron powder size) to create a flat polished surface.

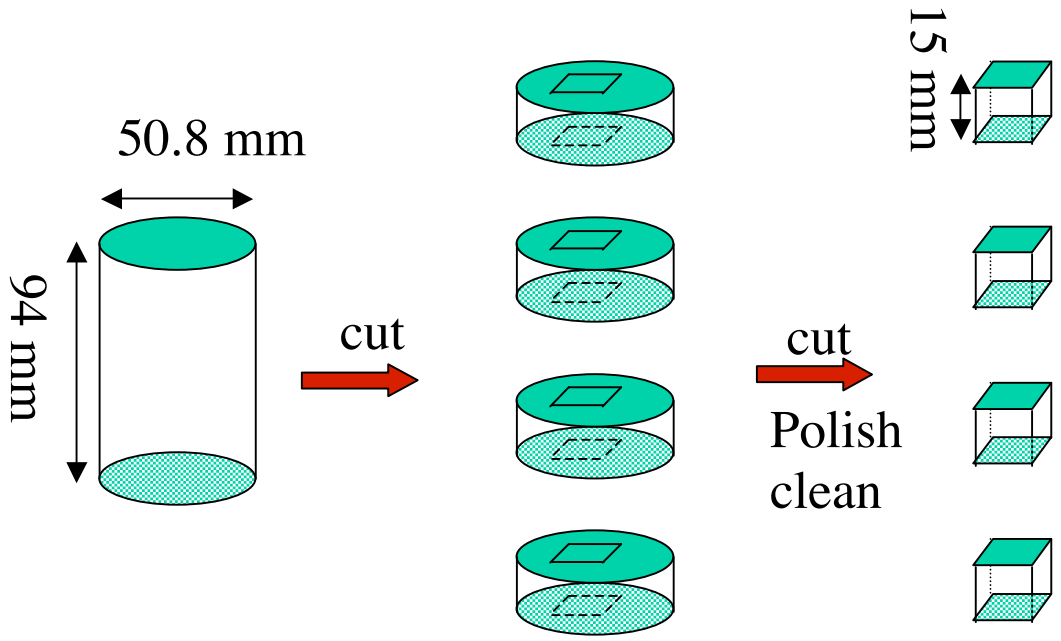

Figure 2.3.1 Sketch of SEM sample preparation that is performed after the sample has been injected with Wood's metal.

2.3.2 SEM Scanning Procedure for Sandstone Samples

Using a Scanning Electron Microscope enables the collection of high magnification images of the pore space and metal-filled pore space in the sandstone samples. The SEM used for this project is a JEOL 35CF operated with an accelerating voltage 25kv, an objective aperture setting of #2, a working distance of 39 mm and a condenser lens current of 2.00 to 3.00.

To ignore topographic information from the SEM images, the SEM is operated in a point by point scanning mode using the backscattered (Backscatter Electron Image - BEI) and COMP mode settings. A slow scanning speed is used because the signal is weak and noisy. Digital images are collected with IMIX software installed in a computer, which is connected to the SEM.

The contrast in the resulting image is determined by the material type (atomic number) on the sample surface (Wood's metal, sandstone, air). In the initial testing, the sample was injected with epoxy after being injected with Wood's metal. The epoxy-filled portions of the pore space represented the location of the ethylene gylcol. For samples with a high saturation of Wood's metal, it became difficult to inject epoxy into the sample. The epoxy injection step of the procedure has been eliminated. This requires us to assume that any portion of the pore space not filled with Wood's metal would be filled by a wetting phase.

2.3.3 Wood's metal Injection Procedure for High Injection Pressures

Wood's metal injection experiments were performed on several sandstone samples at for a range of injection pressures (0.016 MPa - 0.69 MPa). The following procedure was used for Wood's metal injection experiments for injection pressures greater than 0.69 MPa:

1. Place Wood's metal tank (Figure 2.3.2). Mount the sample in holder and install sample in the other tank and seal. Fill the holding tank with paraffin oil. Close valves 1, 2, 3, 4, and 5. Place flexible heaters on the outlet tubing leading to sample and the chamber on the tubing. Monitor the temperature and pressure of the whole system.
2. Increase the temperature of the paraffin oil to 90 ºC. Once a temperature of 90 ºC has been achieved, maintain the temperature four hours before Wood's metal injection.
3. Apply 137.9 kPa gas pressure to Wood's metal tank. Open valves 1 and 4. Open valve 2 to let melted metal flow into sample tank until the sample is completely covered by metal as indicated by the level detector.
4. Close valves 1 and 2. Heat the outlet tubing and chamber to around 90 ºC.
5. Apply desired gas pressure to sample tank. Open valves 1 and 4 for metal injection. Use scale to monitor ethylene glycol flow rate. Adjust gas pressure during the injection to maintain a constant pressure. Turn off valve 1 when steady ethylene glycol flow is reached while maintaining the pressure in sample tank. Stop heating the outlet tubing and chamber.

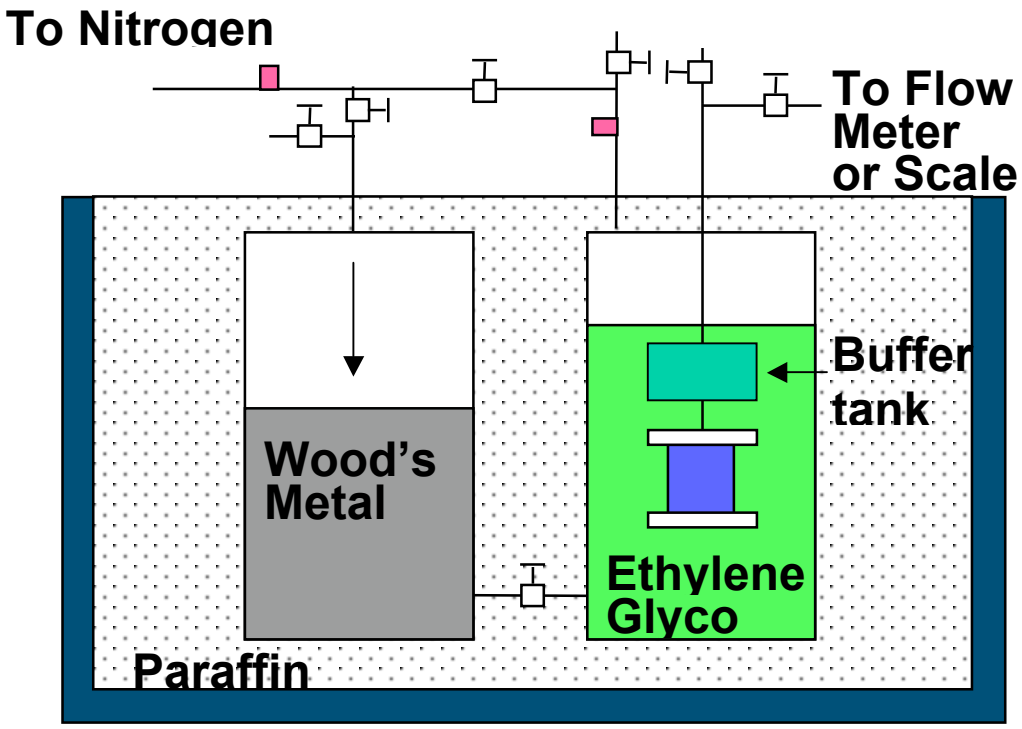

Figure 2.3.2. Schematic of Wood's metal injection system for samples 100 mm in length.

6. Open valve 3. Open valve 2 to let metal flow from sample tank to Wood's metal tank while the pressure in sample tank is maintained at the desired value. Let the metal flow until the sample is not in contact with the metal (based on level detector).
7. Drain paraffin oil from the holding tank and let the system to cool down.
8. Relieve gas pressure when temperature is lower than 50 °C. Open sample tank and remove sample out for further experiments and measurements.

2.3.4 Wood's Metal Injection Procedure for Low Injection Pressures

For low injection pressures (less than 0. 34 MPa), the time needed to reach equilibrium would require on the order of several months per sample for samples 100 mm in length. Results from experiments performed for this contract showed that saturation of Wood's metal with depth in the sample (i.e., parallel to the long axis of the core) did not vary significantly. Thus, we concluded that samples with one-quarter of the length (25.4 mm) could be used for experiments where low injection pressures are used to reach equilibrium in a reasonable time frame. To achieve low injection pressures, the Wood's metal injection system was re-configured as shown in Figure 2.3.3.

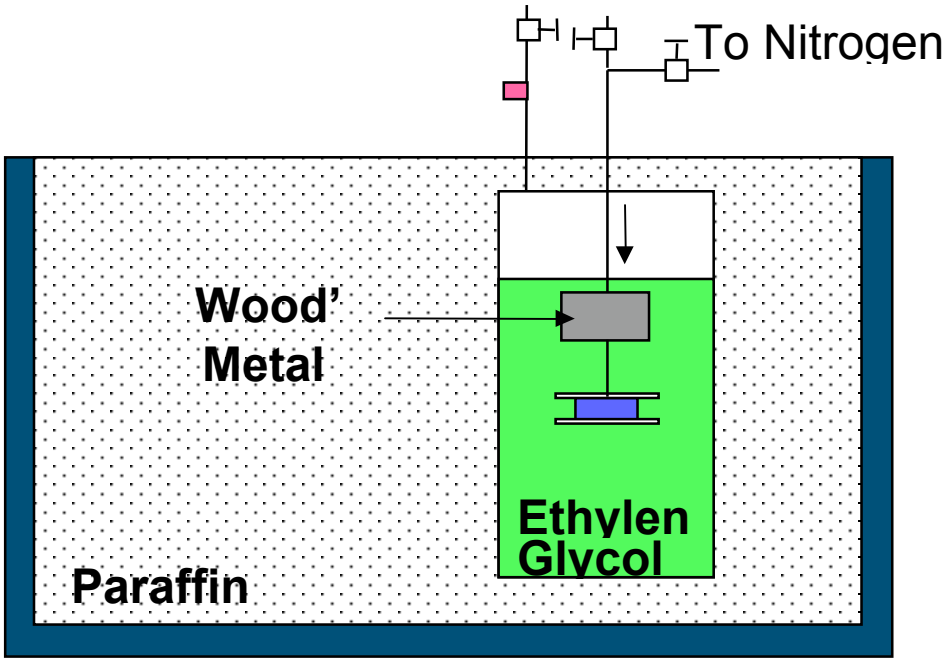

Figure 2.3.3. Wood's metal injection system for low injection pressures (i.e., less than 34.5 kPa)

For the low injection pressure experiments, only one confining pressure vessel is used. The confining vessel is initially filled with ethylene gylcol which is used to vacuum saturated the sample with a wetting phase (ethylene gylcol) and is the medium to transmit heat to the sample. After vacuum saturation, the system is heated to 95 ºC. A chamber above the sample (Figure 2.3.3), contains Wood's metal. The height of the Wood's metal above the sample is used to create the injection pressure (i.e., the pressure is equal to the density of Wood's metal times the acceleration due to gravity times the height above the inlet) in addition to an applied Nitrogen pressure of a 6.9 kPa. The injection procedure continues until equilibrium is reached. Approximate injection time for low pressure was estimated following post flow data. The flow rates at low pressures are vary low. The height of the remaining Wood's metal in the chamber is checked to determine the pressure.

3.0 Results and Discussion

3.1 Optical Coherence Imaging

Optical coherent imaging of sandstone is a laser ranging technique that extracts structure as a function of depth inside translucent media (sandstone) by measuring the time-of-flight of the optical reflections from a pulsed laser. The data exist as data volumes of approximately 1 mm^3. Within this volume many reflections from individual sand grain facets can be identified. The density of reflections and the intensity of the reflections provide statistical information about sandstone properties related to porosity as well as grain and pore size.

This section describes the basic volumetric data sets and presents characteristic results from sandstone samples in Section 3.1.1. This is followed by attempts at grain and pore geometry reconstruction in Sections 3.1.2 and 3.1.3. Facet "drop-out" is introduced and explained as a current (but potentially surmountable) limitation on the ability to identify individual grains and pores. Quantitative and statistical results are presented in Section 3.1.4 on volumetric data, followed by preliminary results on the walls of boreholes in sandstone in Section 3.1.5.

3.1.1 VOLUMETRIC IMAGING

A "flythrough" produces a data volume of back-scattered reflections. These data are acquired as sections that are acquired successively deeper into the sandstone. The stack of frames makes a data volume that can then be visualized using graphic visualization techniques. Figure 3.1.1a shows selected xy sections (see Figure 2.1.7 in Section 2.1.2.1 for orientation) from a flythrough of a dry sandstone sample with a saw-cut surface. The associated yz sections are shown in Figure 3.1.1b. There is noticeable structure in these sections, with dark representing bright reflections and light representing weak reflections. In the yz-sections there are noticeable gaps where there appear to be no reflections at all. These may arise either from the inside of very clear grains, or the insides of pores. Obviously, for sandstone with clear or translucent grains, it is not possible to tell grains from pores. However, it is still possible to identify density of grain facets and depth of penetration, which are two optically extracted indicators of the condition of the sandstone. From the yz sections, there is some evidence that the surface layer may be damaged, or is impregnated with rock dust because of the relatively strong and uniform reflections from across the whole the surface.

A volumetric rendering of the data from Figure 3.1.1 is shown in Figure 3.1.2, which is represented as an iso-surface, with the top layer capped with a section that is false-colored. The noticeable voids are apparent in this figure too, but it is not possible to assign them as pores or as grains. It is also important to keep in mind that discrete facets on grains are spread into a point-spread function by the finite longitudinal resolution (30 microns) of the laser ranging. The iso-surface rendering therefore tends to show facets as volumes that may be mistaken for grains or pores. This data shows clearly the difficult problems that are faced when trying to extract specific structure from the datasets.

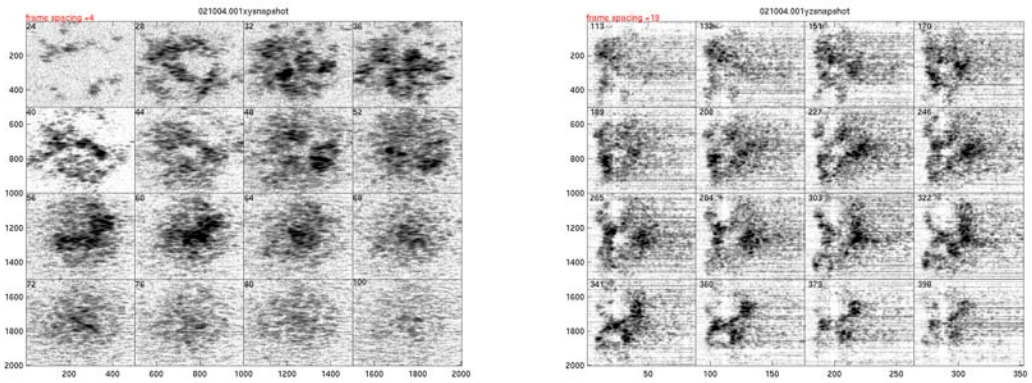

Figure 3.1.1 a) selected xy sections showing reflections from succesively deeper in the sandstone. b) selected yz sections (the top surface of the sandstone is on the left in each frame). The data volume is approximately 1 mm^3.

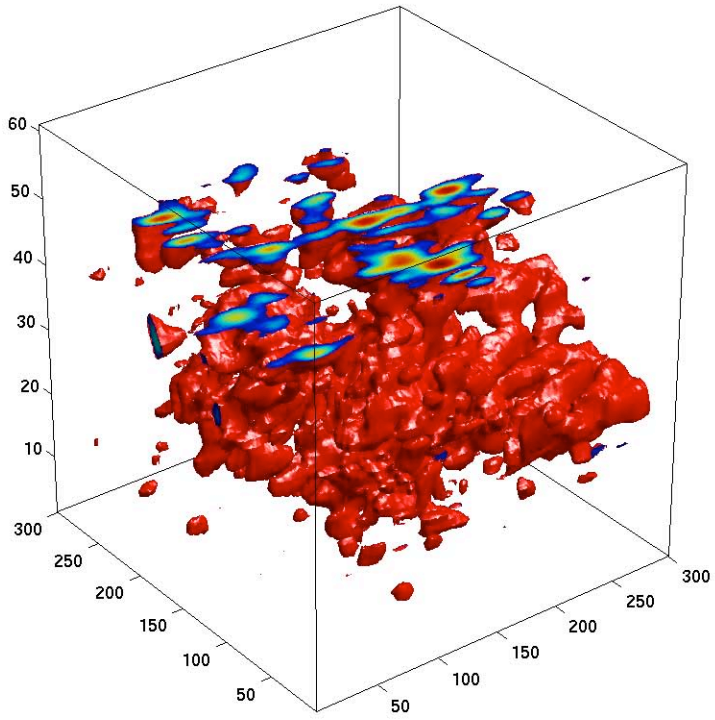

Figure 3.1.2 Volumetric rendering of 02/10/04.001 sandstone data showing the dominant backscatter with the top-surface emphasized with false color.

Despite the ambiguity between pore and grain, it is still possible to identify specific features in specific sections. Figure 3.1.3 shows a series of cross-section of dry sandstone with a distance of 12 μm in the y direction between image sequences. To better view the results, a rainbow pseudo-color is used with red being the brightest and purple being the

dimmest reflectionss, and the scale of the intensity is displayed in a color-bar. The dimensions of the images are 1.0 mm (lateral) × 1.0 mm (depth). Depth is along the horizontal axis with increasing depth to the right. Generally, the bright reflections come from the low-angle grain facets. High-angle facets (i.e., sub-parallel to the beam) generate no, or weak, reflections.

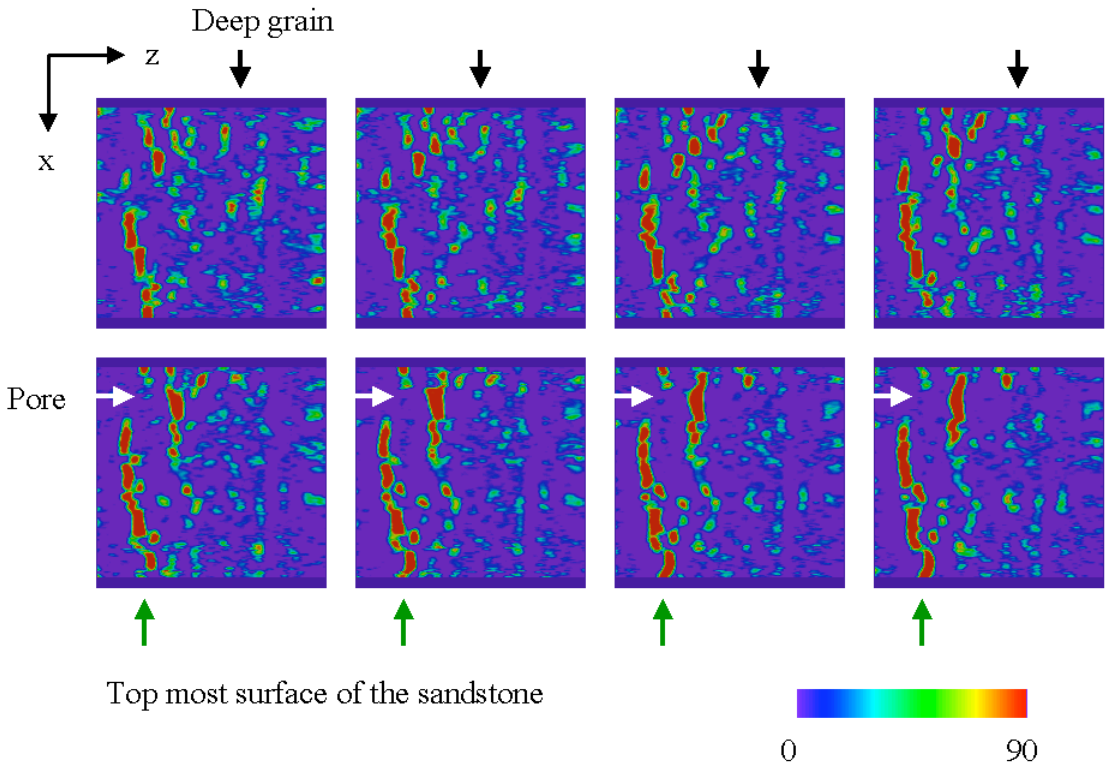

Figure 3.1.3 Cross-section holograms of dry sandstone. Frames separate in y direction with a distance of 12 μm. The dimensions of the frames are 1.0mm x 1.0 mm.

Correlative imaging using conventional microscopy compared with OCI data makes it possible to identify features in the holographic datasets that come from specific grains or voids. This is illustrated in Figure 3.1.4 which shows an SEM and optical micrograph along with sections of the volumetric holographic data. The grains are labeled in the SEM and optical micrographs. The highest grain is labeled A, with grains B and C at lower elevation. This is seen directly in the OCI sections. Note that the interior of a grain is dark, as shown for grain A when the tops of grains B and C “light up”. The y-z and x-y sections show this clearly on the right side of the figure.

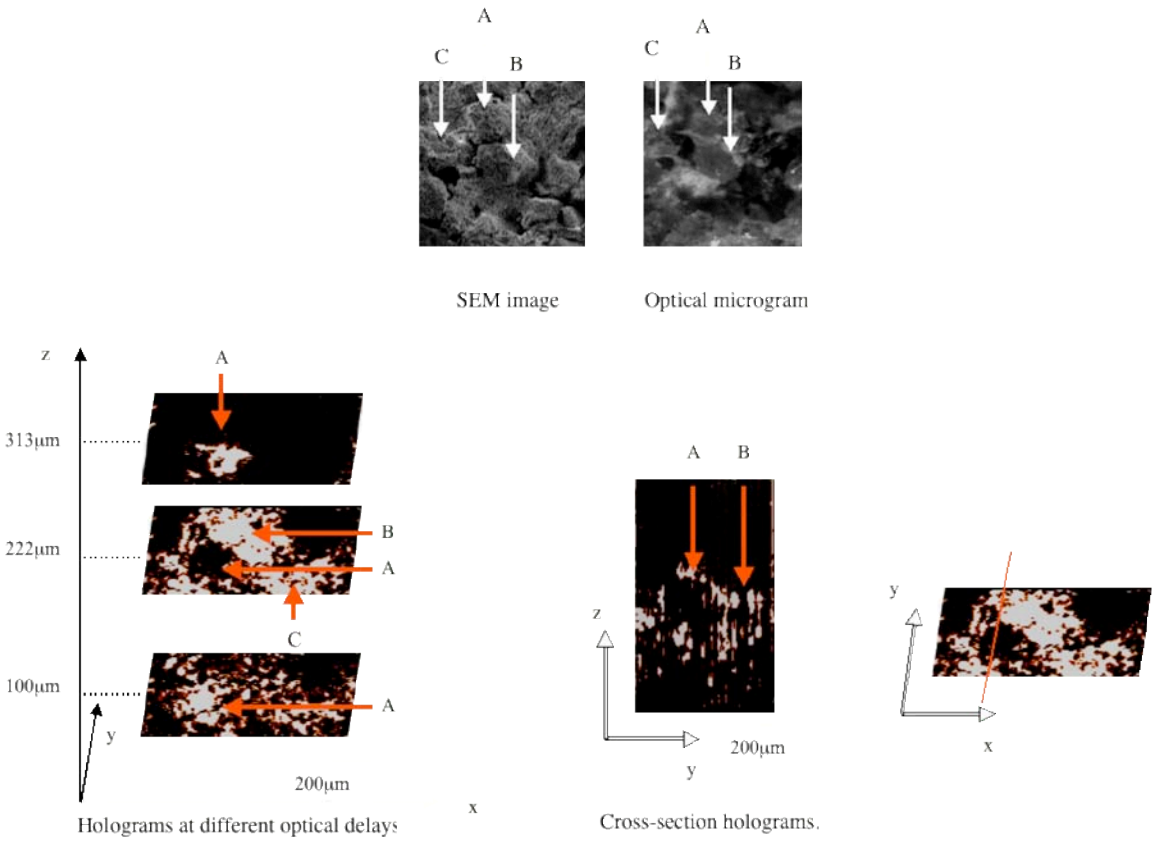

Figure 3.1.4 Comparison of OCI volumetric data with conventional optical and SEM micrographs. The lateral scale is 200 microns. The grain sizes are typically less than 100 microns.

3.1.2 Grain Reconstruction from Volumetric Data

The ultimate goal of holographic imaging into sandstone (to identify grain and pore boundaries) is made difficult by the optical properties of specular facets on sandstone grains. As shown in Figure 3.1.5, high-angle facets do not scatter light into the collecting optics and hence are not visible. This facet drop-out makes it difficult to define the perimeters of individual grains. Circumstantial evidence may be used to try to delineate grains from each other and from voids. But this approach is highly subjective and hence not easily quantifiable.

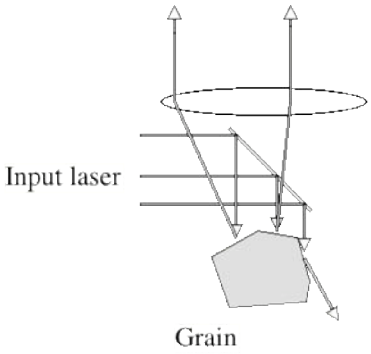

Figure 3.1.5 Showing low-angle and high-angle facets relative to the optic axis. High-angle facets do not scatter light into the collecting optics and hence are "invisible".

Careful examination of the image sequence in Figure 3.1.3 shows that there is a pore structure (or missing grain) near the sample surface marked with white arrows. In Figure 3.1.6, two grains marked as red and green arrows in each frame can be seen, which shows possible structure with one grain behind another in depth. The areas outlined with white dashed lines in Figure 3.1.10 show several reflections with large angles corresponding to the sandstone surface from some tilted facets of the grains. Also, a pore structure (or missing grain) marked with a white arrow is seen near the sample surface.

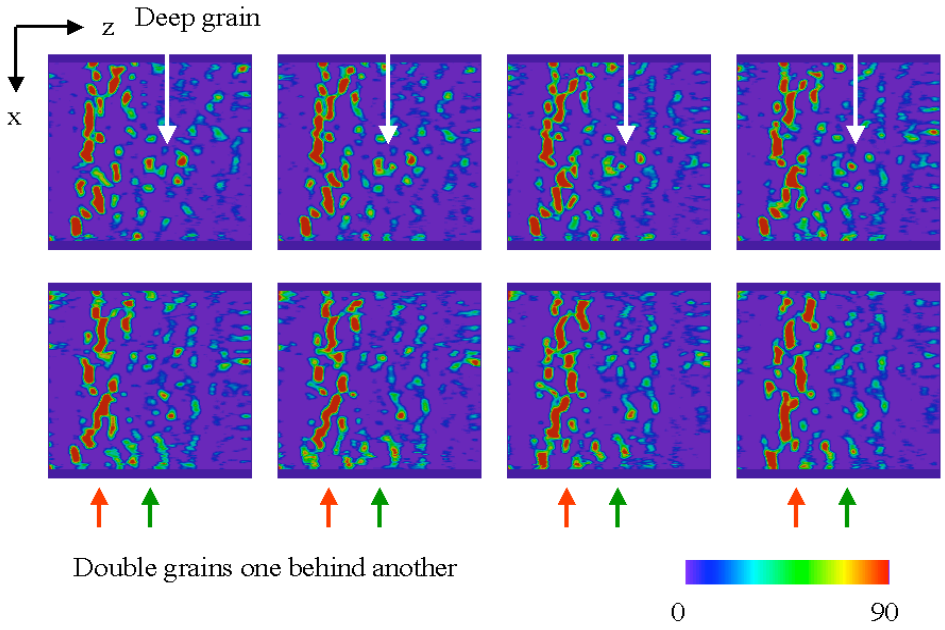

Figure 3.1.6 Cross-section holograms of sandstone. Frames separate in y direction with a distance of 12 μm. The dimensions of the frames are 1.0mm x 1.0 mm. A "deep" grain is shown by the white arrow. Two grains "stacked" are shown by the red and green arrows.

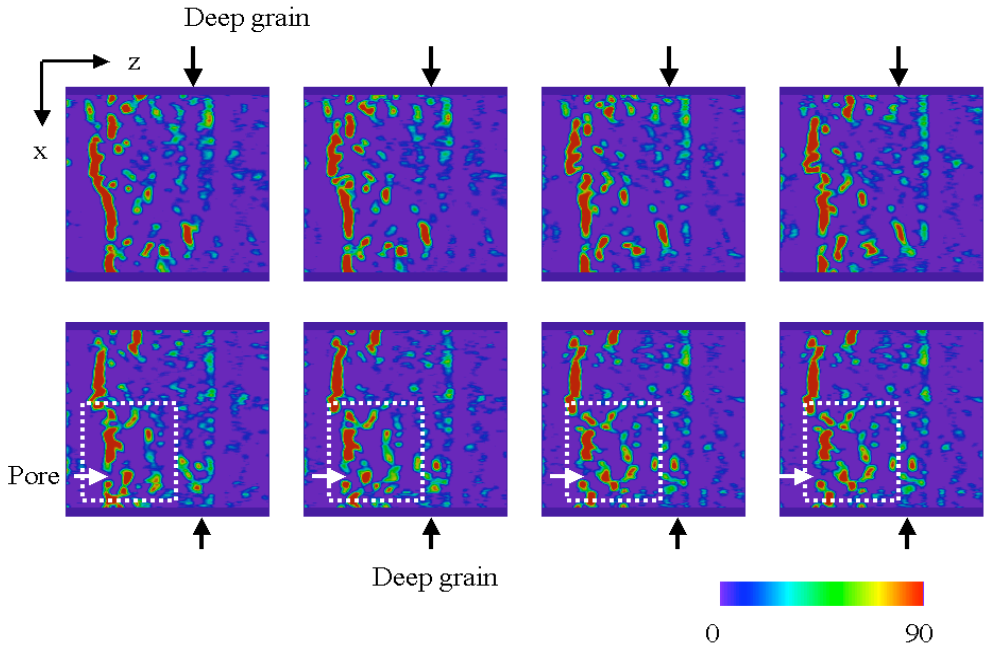

Figure 3.1.7 Cross-section holograms of sandstone. Frames separate in y direction with a distance of 12 μm. The dimensions of the frames are 1.0mm x 1.0 mm.

By looking for closely-spaced reflection peaks in the depth sections, it may be possible to measure the gaps between grains. An OCI hologram of sandstone is displayed in Figure 3.1.8a. The hologram is a cross-section of a sandstone sample in the x-z plane at y = 820 μm showing considerable structure down to 500 μm deep, extending through several grains at each position. Line sections at the location x = 75 μm and 156 μm are shown in Figure 3.1.8b. Reflections indicated by arrows from the top and the bottom of grains can be seen, as well as deeper reflections from deeper grains. Though it is not possible to determine the 3D structure from a single cross-section, the full data set may contain sufficient information to fit the positions and shapes of numerous grains in the top several layers of grains in the sandstone sample. We found some facets inside the sandstone that are stronger than the one from the topmost facet.

In a further attempt to identify grain structure, we adopted the configuration shown in Figure 3.1.9. A transparency with a hole in it is placed on top of the sandstone. The edge of the hole makes it possible to locate specific grains between optical micrographs and the OCI datasets. The optical micrographs are shown in Figure 3.1.10.

Three sections from a holographic dataset are shown in Figure 3.1.11. The section in a) is entirely through the transparency that is seen as two parallel reflections (top and bottom). The top of the sandstone is seen below the bottom of the transparency. The section in b) cuts from the transparency through the edge of the hole. The sandstone reflections are noticeably brighter through the hole than through the transparency. The section in c) is almost entirely through the hole in the transparency. The sandstone features observed through the holes are spatially registered in Figure 3.1.12 with grains observed in the optical micrograph. One of

the important conclusions from this figure is the brightness of the top of the grain, but the nearly invisible sides of the grains in the OCI datasets. While the grains can be clearly identified from the optical micrograph, in the absence of the micrograph, it is virtually impossible to identify the boundaries of the grains in their midsections.

Based on the results of this component of the research project, we must conclude that identification of individual grains and their boundaries exclusively from OCI data is not currently possible. High-angle and vertical facets are not visible in OCI. Therefore, the OCI datasets consist of only partial grain edges that cannot be distinguished in isolation from pores. However, using additional techniques described in the next section, there is still a possibility to identify pore sizes.

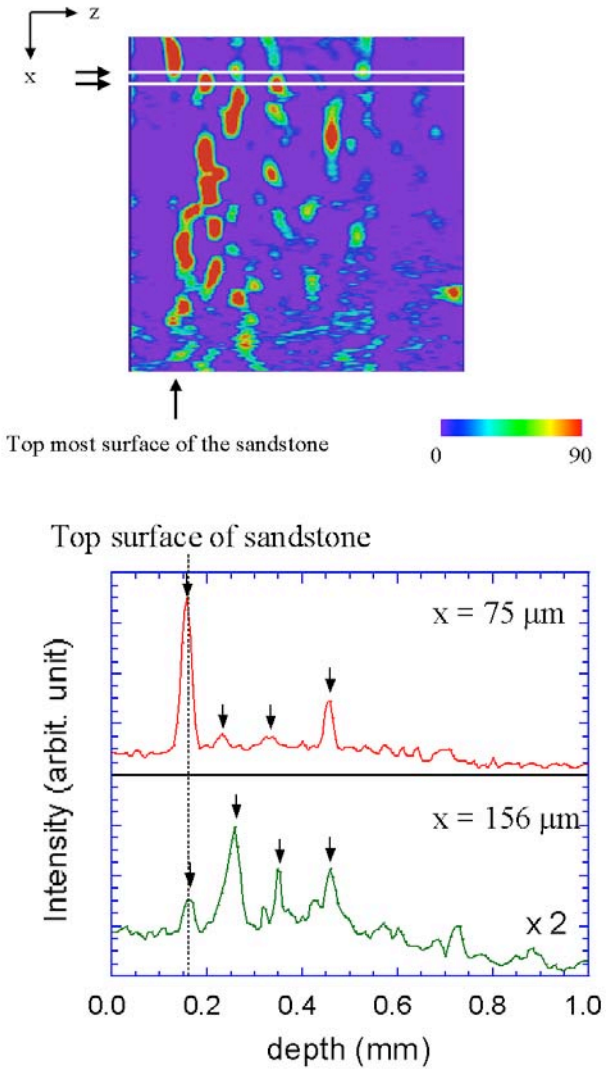

Figure 3.1.8 (a) Cross-section at location y=820 μm with dimensions 1.0 mm by 1.0 mm in the x-z plane, showing considerable structure half a millimeter deep into the sandstone sample. The bar represents the scale on both x and z axes. Marked lines show where the intensity cross sections of (b) were taken. (b) Intensity cross-section through 1.0 mm depth at x=75 μm and 156 μm.

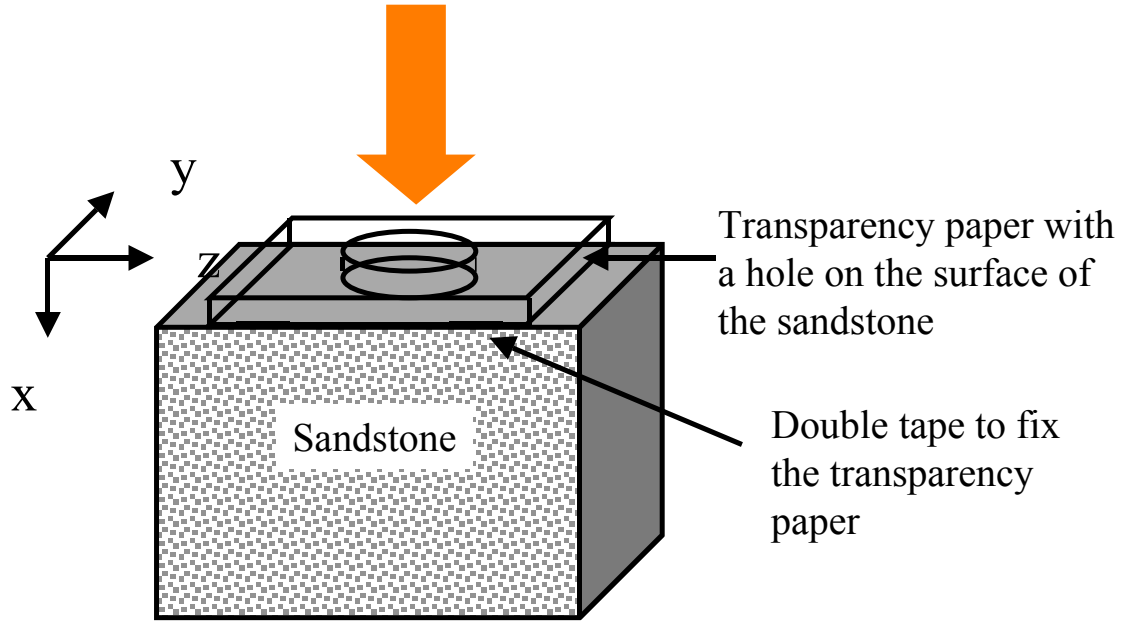

Figure 3.1.9 Transparancy with a hole to help register OCI datasets with optical micrographs.

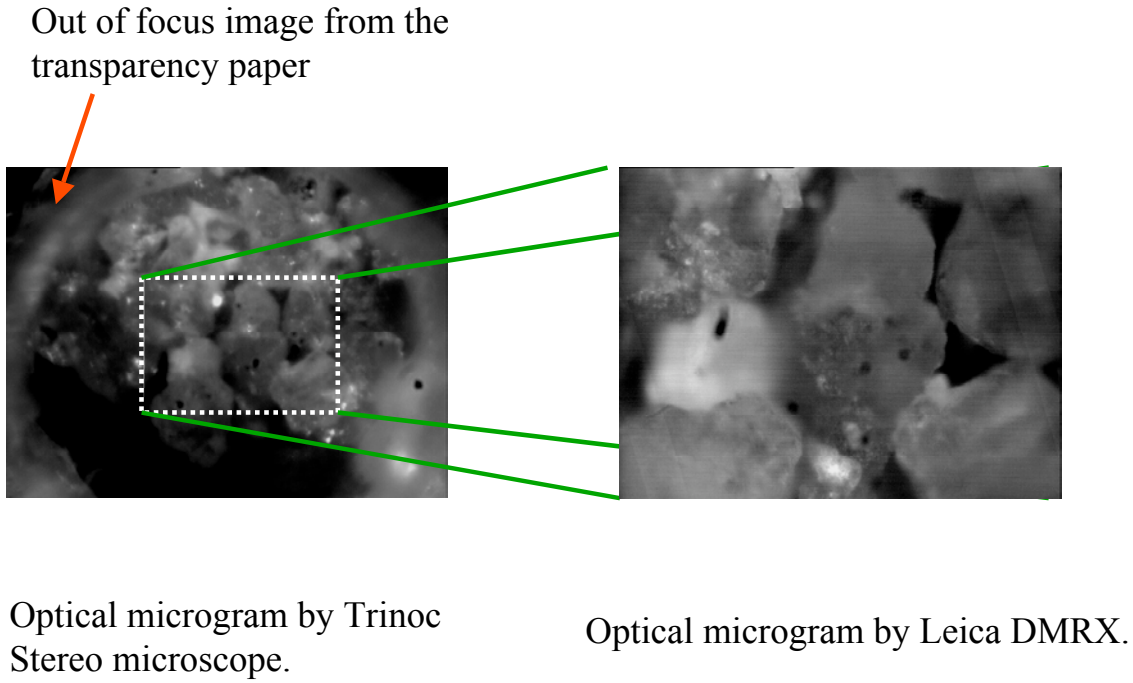

Figure 3.1.10 Optical micrographs of sandstone imaged through a hole in a transparancy

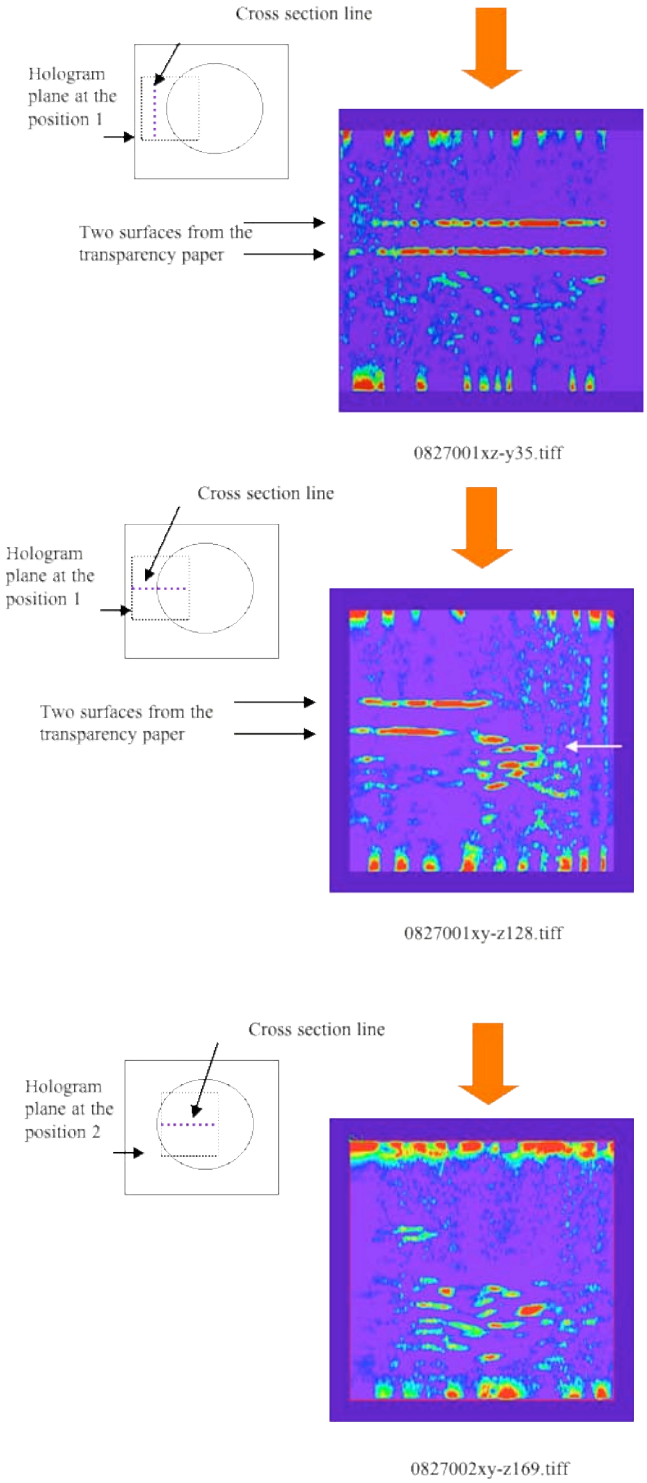

Figure 3.1.11 Selected sections through volumetric datasets that include the edge of the transparency hole for spatial registration of OCI features with optical micrographs.

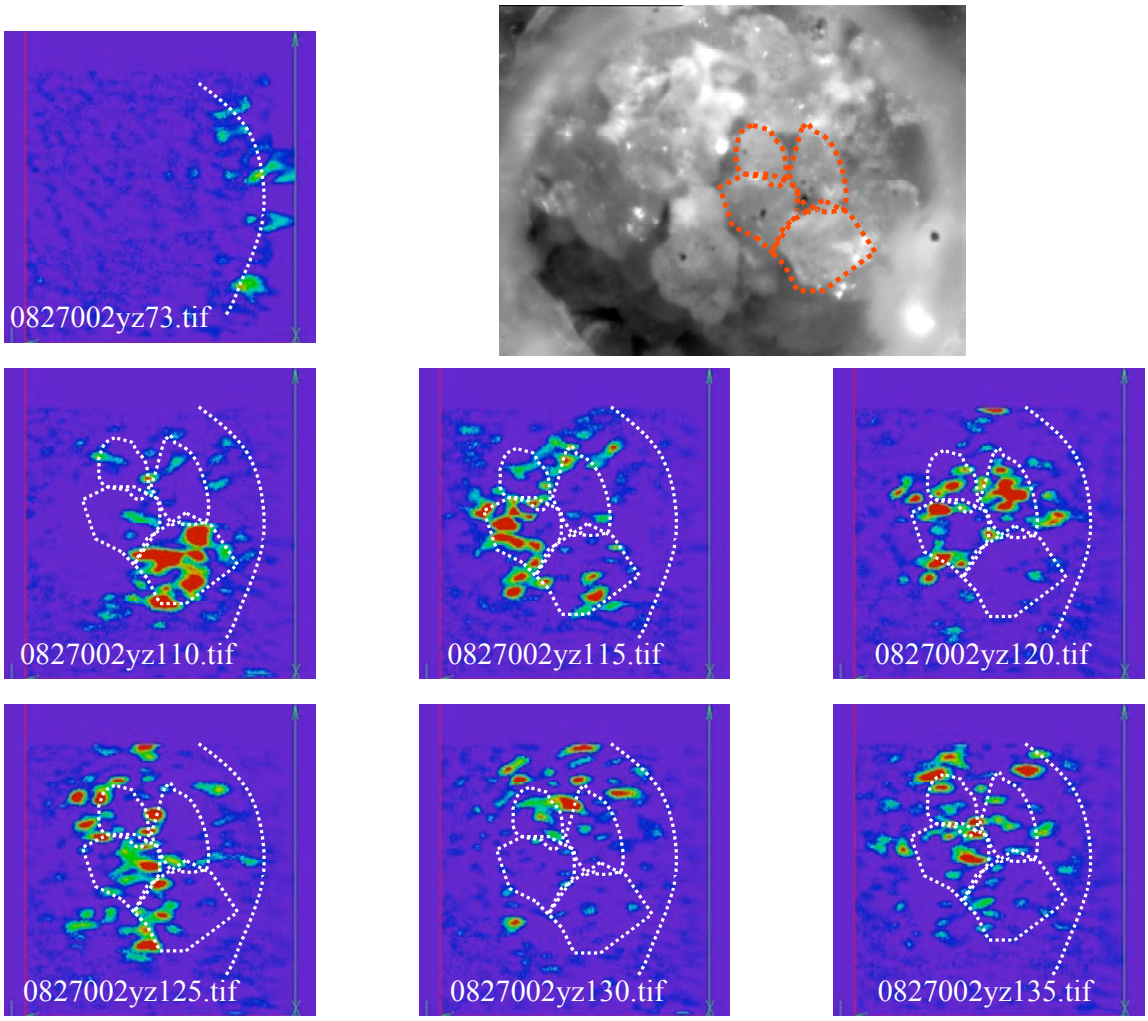

Figure 3.1.12 Spatial registration of sandstone grains observed in volumetric OCI relative to the optical micrograph.

3.1.3 Pore Reconstruction from Volumetric Data

By acquiring two volumetric datasets, one dry and the other saturated with water, it is possible to identify specific boundaries of pores separately from the boundaries of grains. Two facets bounding a void each produce reflections that are identical to the facets bounding a grain, making it impossible to identify each separately. But when water is introduced into the pore-space, the light time-of-flight through the now water-filled void increases, stretching the apparent distance between reflections. Therefore reflection doublets that stretch upon the addition of water to the pore space can be unambiguously identified as voids spaces, while doublets that do not change are identified as the grains.

Selected yz sections of a sandstone sample in the dry compared to wet condition are shown in Figure 3.1.13. The most obvious difference is the weakness of the reflections in the wet case. This is because water is more nearly index-matched to the sandstone grains than is air. This reduces the reflection at a specular grain to only about 2%. General structure is shared by each set of sections, but the wet sections do show a slight stretching. This is quantified in Figure 3.1.14 that shows the average intensity vs. depth for the dry and wet samples. The wet sample shows reflections from slightly deeper in the sandstone. The shift in the peaks corresponds to an approximately 100 micron pore width in this sample.

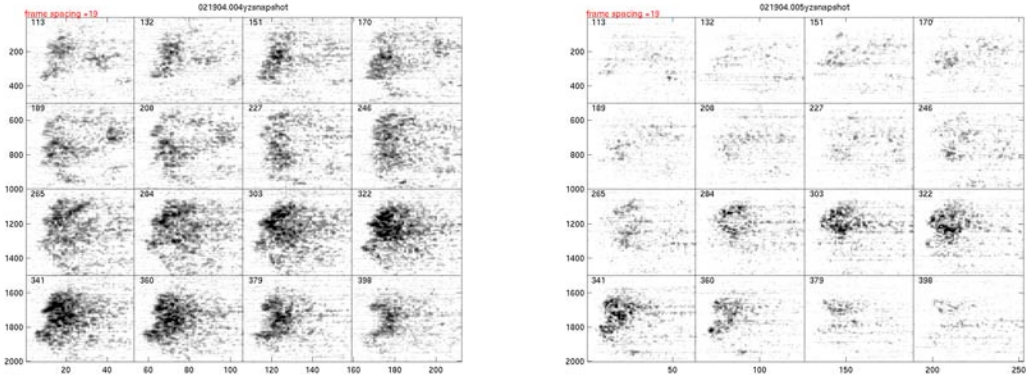

Figure 3.1.3 Selected yz sections for a single sample under dry (left) and wet (right) conditions. The water-grain interface produces a notably weaker reflection.

For a more detailed assessment, cross section holograms shown in Figure 3.1.15 demonstrate the principle of the measurement. The dimensions of the frames are 1.0 mm (lateral) × 0.7 mm (depth). Figure 3.1.15 (a) and (c) are cross-section holograms from the sample with water while Figure 3.1.15 (b) and (d) are cross-section holograms from the sample without water. Straight bright lines can be seen in the x direction in Figure 3.1.15 (a) and (c). These lines come from the water surface reflection. The dashed lines in Figure 3.1.15 (a) and (b) are from the top surface of the sandstone. We can see similarities between the frames. In Figure 3.1.15 (c) and (d), two grains are outlined by a dashed-line square and by a solid-line square. The distance between the grains is changed due to the water. Therefore we *can* recognize the pore space between these grains in this case.

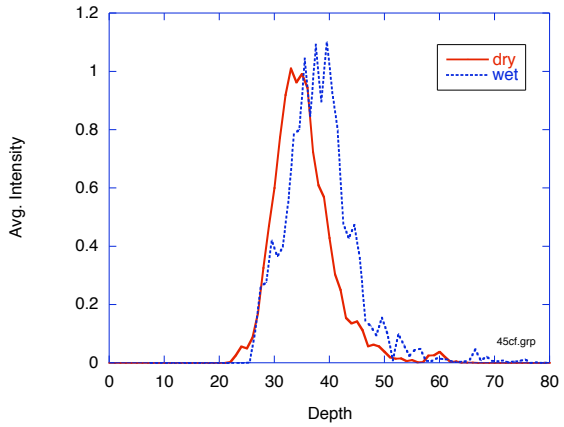

Figure 3.1.14 Average hologram intensity as a function of depth (6.7 microns per frame). The wet-condition average is shifted deeper than for the dry condition. This is caused by a "stretching" of the pores when water is introduced.

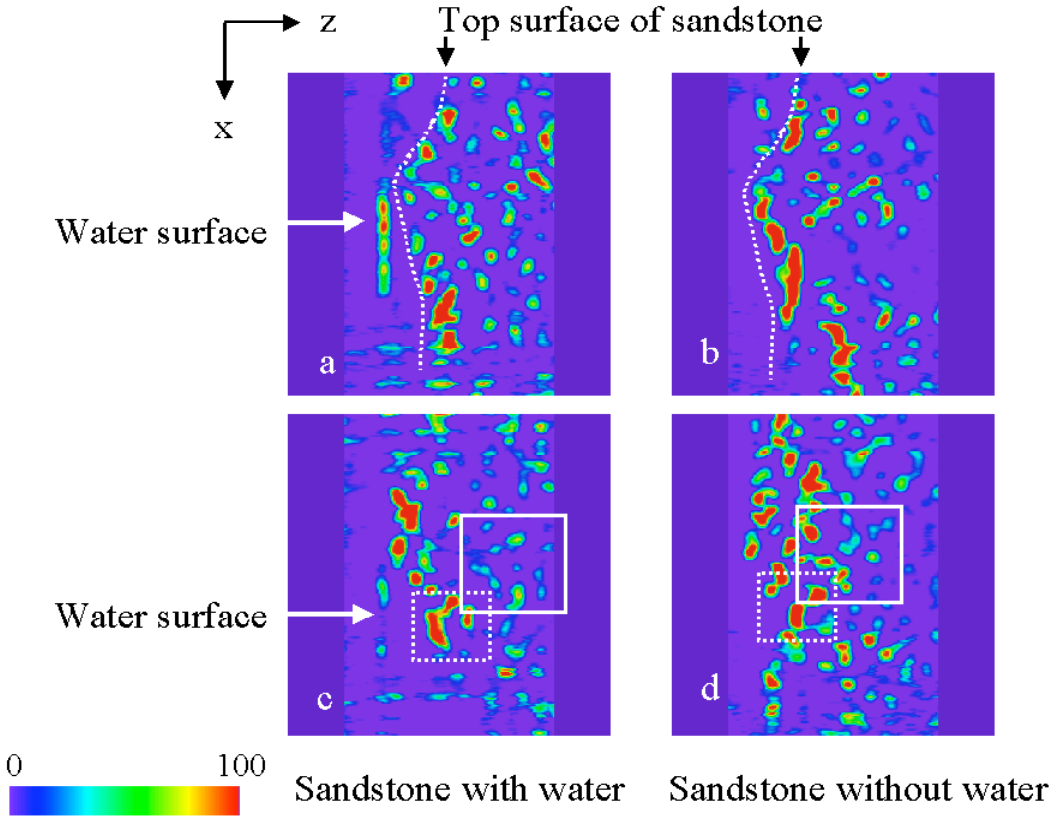

Figure 3.1.15 Cross section holograms of sandstone with (a), (c) and without (b), (d) water. The dimensions of the frames are 1.0 mm (lateral) x 0.7 mm (depth). Dashed lines are from the top most of the sandstone. Arrows show the reflection from water surface. Dashed and solid square marked two grains.

3.1.4 Quantitative Analysis of Sandstone

The key questions that are addressed in this section are what aspects of the physical properties of the sandstone we can extract from the volumetric datasets obtained through the laser ranging. The fundamental properties of porosity and average pore size are of central interest, but cannot be obtained directly from the ranging data. The ranging data provide information on overall strengths and density of backscatter, as well as correlation lengths based on the dominant backscatter. It remains an open but potentially solvable problem how to relate these statistical properties to the more fundamental ones of porosity and pore size.

3.1.4.1 Auto-correlation Analysis

The average correlation length of the volumetric data are extracted from auto-correlation analyses. Several average auto-correlation images are shown in Figure 3.1.16a for xy and Figure 3.1.16b for yz. The z and y cuts through the auto-correlation images are shown in Figure 3.1.17. Each auto-correlation trace shows a central peak that corresponds to the point-spread-function of the optical system. The shoulders are more directly related to the structure of the sandstone. The correlation lengths for both the y (transverse) and z (longitudinal) directions are between 100 and 200 microns. These correlation lengths may be taken as average facet spacing. It is not possible for dry samples alone to have this value broken down further into grain size and pore size. However, it is known that the voids in this sandstone are comparable to the grains. Therefore, both the grain and pore sizes are between 100 and 200 microns.

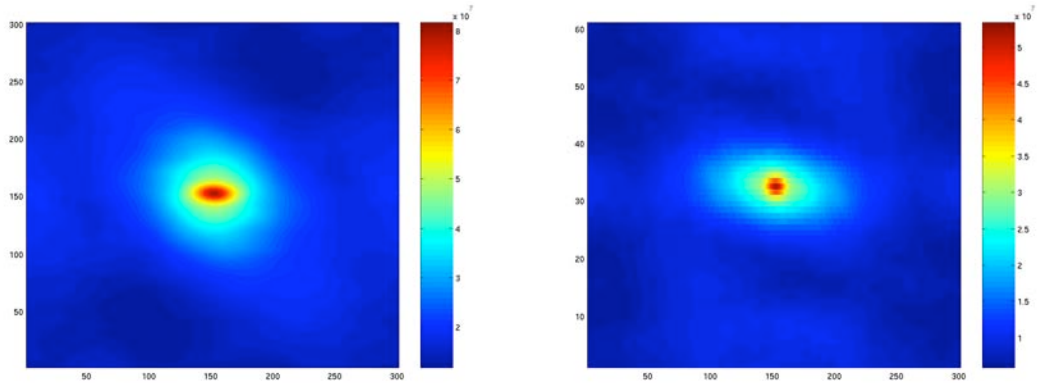

Figure 3.1.16 A) xy autocorrelation and B) yz autocorrelation plots of the laser ranging data of Figure 3.1.2.

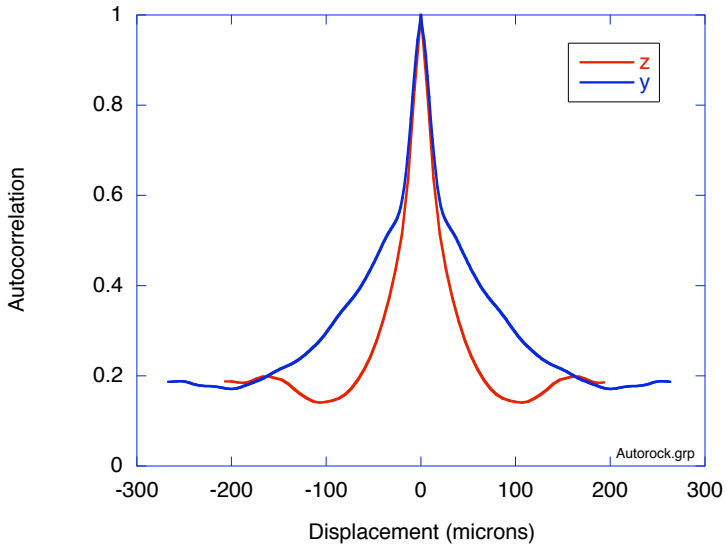

Figure 3.1.17 Autocorrelation functions for z and y directions.

3.1.4.2 Cross-Correlation Analyses

Cross correlation between dry and wet data volumes provides quantitative information on the strength of reflection and on changes that occur between dry and wet conditions. In particular, stretching intervals caused by the addition of water will produce structure or shoulders in the cross-correlation functions that are related to porosity and to average pore size. Examples of a pair of dry and wet data sets are shown in Figure 3.1.18 and Figure 3.1.19. These are "integrated" sections in which the data volume is summed along one dimension. The dry flythrough in Figure 3.1.18 is significantly brighter than the wet in Fig. 1w1 by a ratio of approximately 4:1. R(air/glass) = 4%. R(water/glass) = 1% for a ratio of 4:1. The intensity from diffuse inclusions would be the same, but from water/sand interface 4 times weaker. Therefore it is possible that the bright spots in the wet data are from diffuse inclusions. As a test of repeatability, the wet sandstone data was found to cross-correlates well in repeated wet flythroughs, with a correlation peak of 72% shown in Figure 3.1.20. This is the level of repeatability for this data acquisition technique.

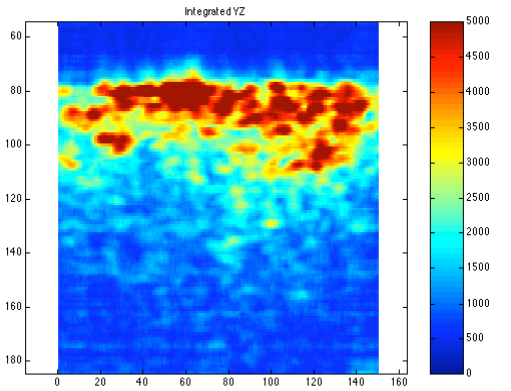

Figure 3.1.18 Integrated dry.

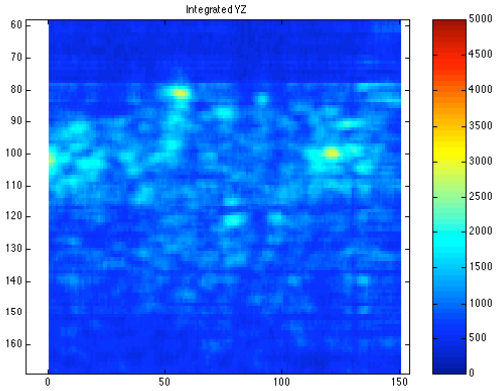

Figure 3.1.19 Integrated wet.

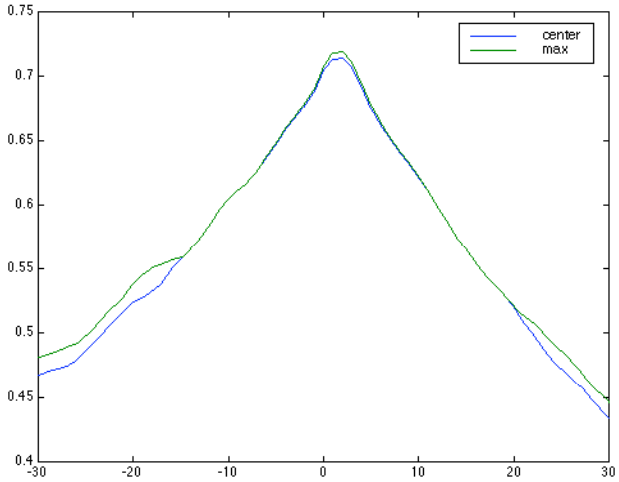

Figure 3.1.20 Crosscorrelation between 1w1 and 1w2. The correlation at no offset is 72%.

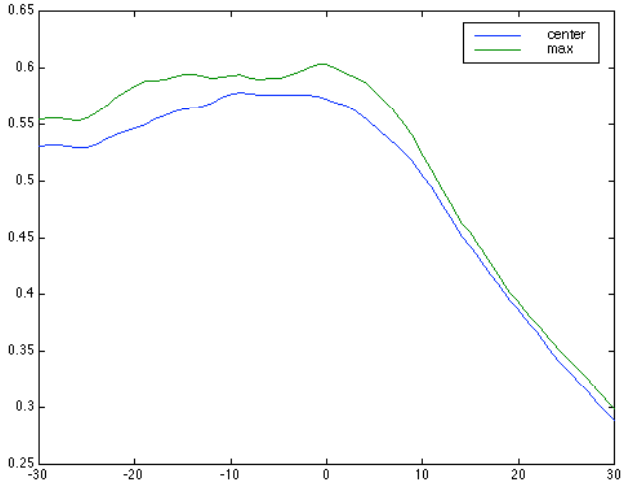

Figure 3.1.21 Crosscorrelation between 1d1 and 1w1 data from 7/29/03.

The dry and wet data cross-correlate like a delta function (dry) with a broad function (wet) as shown in Figure 3.1.21. Negative z corresponds to deeper structure in the wet that must be translated up (negative z) to match the dry case. Note the strong asymmetry. This is caused by the saturation with water. If there were no porosity, then the cross correlation of Figure 3.1.21 would look like Figure 3.1.20 The porosity of the sandstone potentially could be extracted by comparing Figure 3.1.20 to Figure 3.1.21.

After compensating for the faster decay in the dry sample (by expanding the dry data by an exponential), the cross-correlation becomes more symmetric. Again, negative z carries

information on the "stretched" interfaces. This is shown in Figure 3.1.22. Note that the negative z side of the cross correlation shows what appear to be subsidiary shoulders. The spacing of these shoulder is approximately 60 microns, which corresponds to "stretched" pore widths of about 180 microns. This value confirms the values obtained from Fig. 3.1.14 that also predicted pore widths of this scale.

In conclusion, the porosity information is buried in these data analyses, but require significant further topological and statistical development to extract quantitative values.

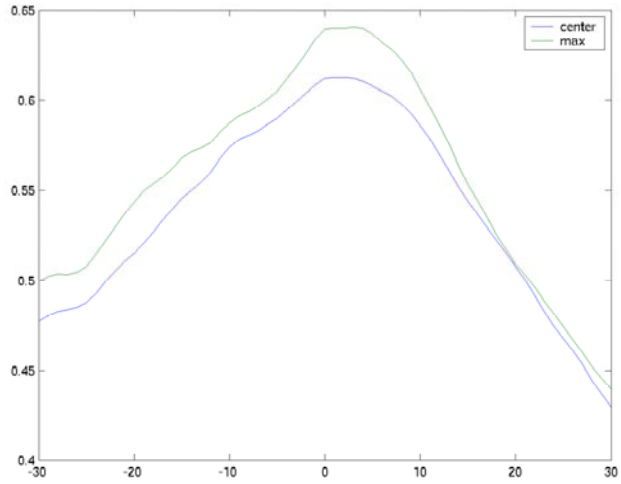

Figure 3.1.22 Crosscorrelation between 1d1 and 1w1 after the dry was exponentially expanded in the z direction. The depth is calibrated at 6.7 microns per frame.

3.1.5 Borehole Data

The final component of the research was to use the laser ranging on boreholes in the laboratory. The data were acquired in two ways: using the full-imaging approach discussed in detail above, and the point-scan method through the borescope. The point-scan method has the advantage that it can be performed down an actual borehole (in the lab) through the use of the borescope. The disadvantage is the short length of the borescope as well as the restriction to scan at only one point. Scan data (A-scans) from the borehole are shown in Figure 3.1.23. Clear facet reflections are observable, and average spacings (approximately 100 microns) are in agreement with the values obtained in the previous sections from statistical analysis of the volumetric datasets.

The point-scan method has a severe disadvantage in speed. The necessity to scan in x and y (rather than acquire full images) slows the volumetric imaging to many hours, making this approach impractical. We therefore bisected the core parallel to its axis and acquired data volumes using the free-space full-frame approach discussed in the previous sections. Selected sections from a series of continguous data volumes from the bore hole are shown in Figure 3.1.24. The sections are integrated, which means they are summed along on dimension. The data are not filtered, but represent the "raw" form that the data take prior to post-processing. The data span a length of approximately 5 mm along the core with a 2.5

mm overlap for each volume. If the individual data volumes could be registered, they would represent a data volume of 5mmx1mmx1mm of the borehole. It remains to develop algorithms that could data-mine this volume for statistical information related to porosity and pore size.

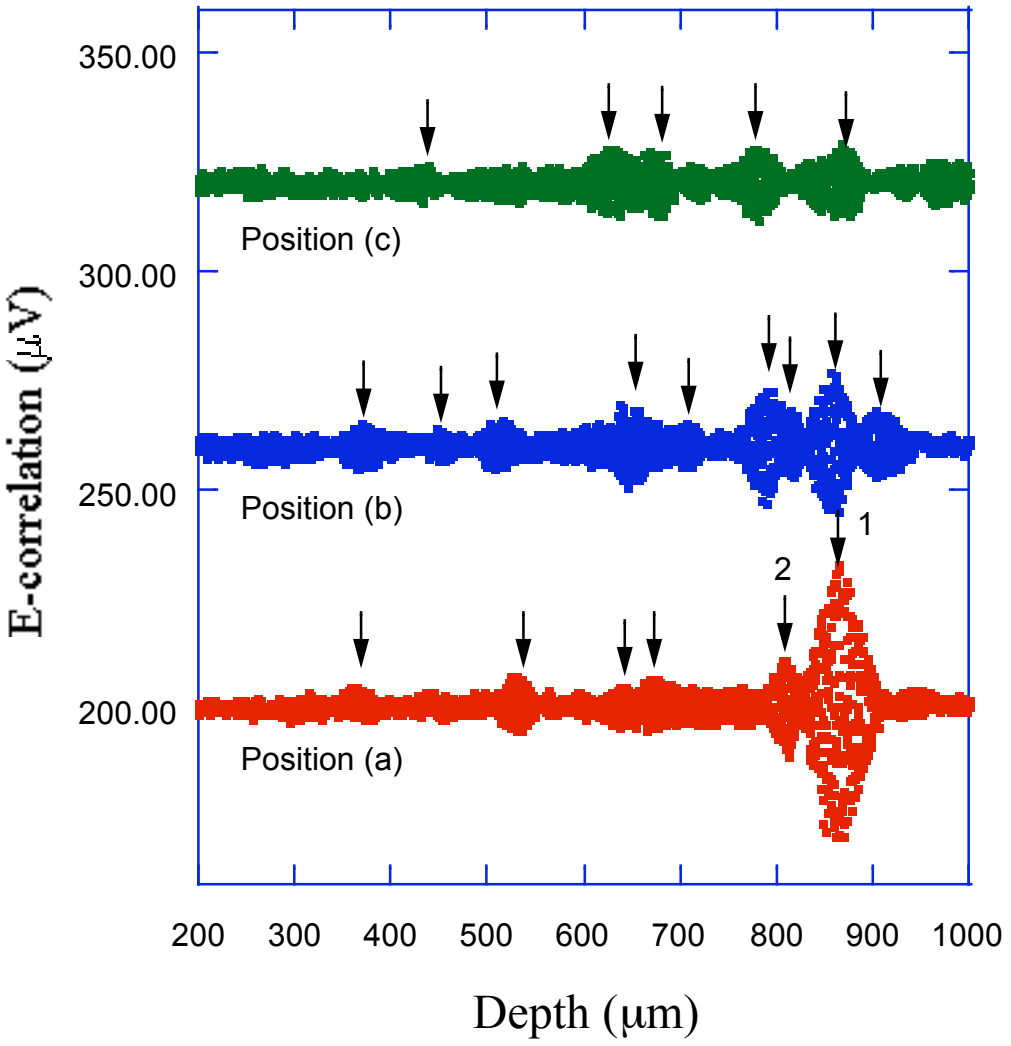

Figure 3.1.23 A-scans at three positions in a borehole. Facet reflections are clearly observed, with average spacings of 100 – 200 microns.

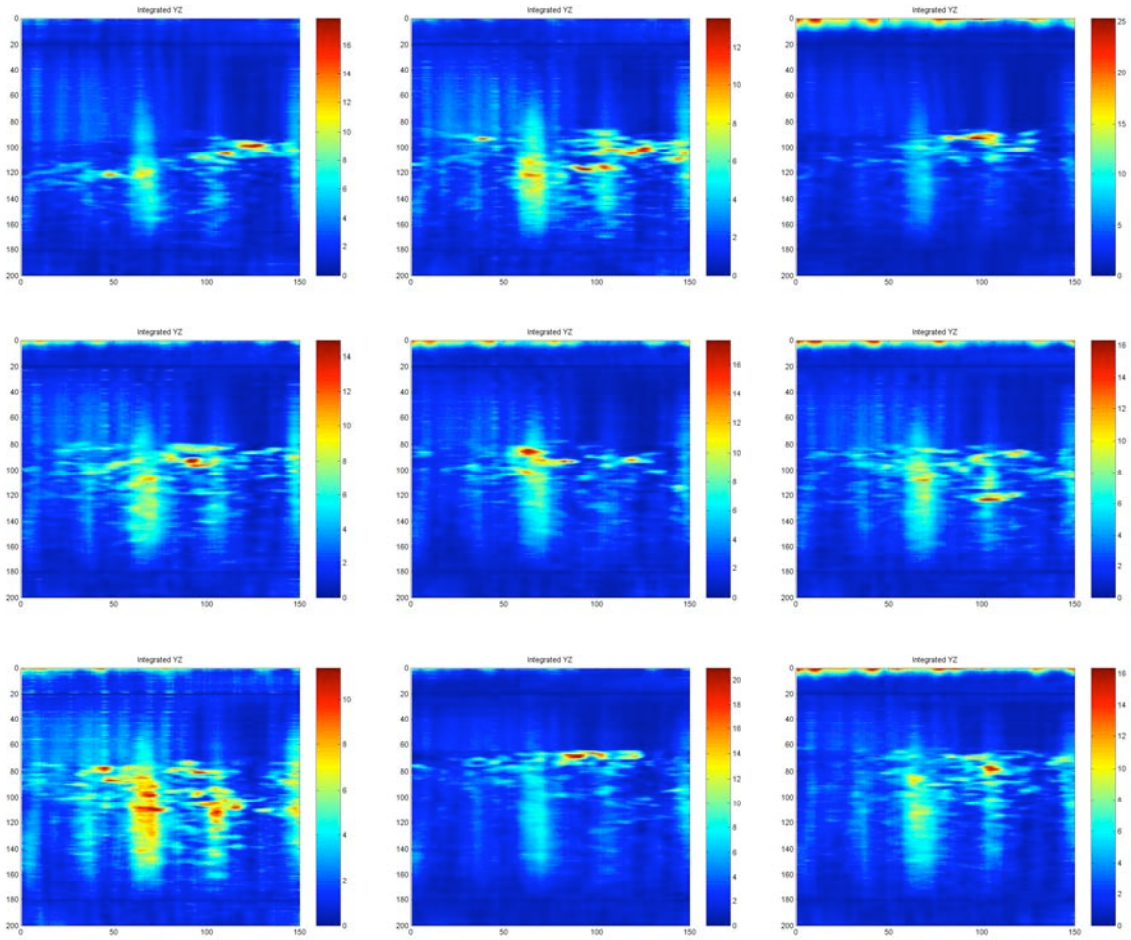

Figure 3.1.24 Nine integrated sections of contiguous data volumes along a borehole. The data span a length of approximately 5 mm along the bore with a 2.5 mm overlap for each volume. If the data could be registered, they would represent a data volume of 5mmx1mmx1mm of the borehole.

3.2 Micro-Models

A key and unique aspect of our work is the ability to obtain very high resolution optical images (0.6 micron per pixel) of the fluid phases as they invade or are forced from the system. To this end, photo-projection lithography (see section 2.2) was used to make transparent micro-models that were 600 μm x 600 μm with an aperture of 1.08 μm and in-plane features as small as 6 microns.

The work supported by this contract produced the first experimental evidence that interfacial area per volume (IAV) removes the ambiguity associated with the hysteretic relationship between capillary pressure and saturation observed for porous media (i.e., sandstone, other rocks as well as soils). In our case, with the flow patterns being really two dimensional, this is really the interfacial length per unit area, but to be consistent with common usage we will still use the term *IAV*. The results in this report (which are published in Cheng et al., 2004) are the first experimental measurements of the *IAV* in any system. In this section will we show representative data and analyses for the micro-model portion of the research.

3.2.1 Fluid-Distributions within Spatially Correlated and Uncorrelated Micro-Models

Micro-models with spatially correlated and spatially uncorrelated void geometry were used to investigated the relationship among capillary pressure, saturation and interfacial area per volume. The micro-model geometry was generated using the algorithm of Nolte and Pyrak-Nolte (1991). Sample S8 has a spatially uncorrelated void geometry (Figure 3.2.1a),i.e., a random continuum percolation pattern with a porosity of 64%. Sample S6 has a spatially correlated void geometry (Figure 3.2.1b), i.e., a stratified percolation pattern with a porosity of 55%.

The samples were initially saturated with decane. Then nitrogen gas was allowed to invade by the application of pressure. This pressure was increased in stages, with the system allowed to equilibrate for several minutes between each pressure step. Eventually, after on the order of 30 pressure steps (further details of the pressure steps will be given below), the nitrogen gas formed a continuous (geometric) phase across the sample, and flow began. Beyond this point, there was no further change in the geometry of the nitrogen and decane regions. However, there was still decane trapped in the system, in small isolated pockets. Decane was then allowed to re-enter the system, again by the application of pressure. The pressure was increased, in the same manner, and eventually decane could flow through the system.

Such drainage-imbibition cycles were traversed repeatedly for each sample. Figure 3.2.2 shows Sample S6 (spatially correlated) during imbibition (Figure 3.2.2a) and during drainage (Figure 3.2.2b). In the image the white areas represent nitrogen, the light gray regions decane

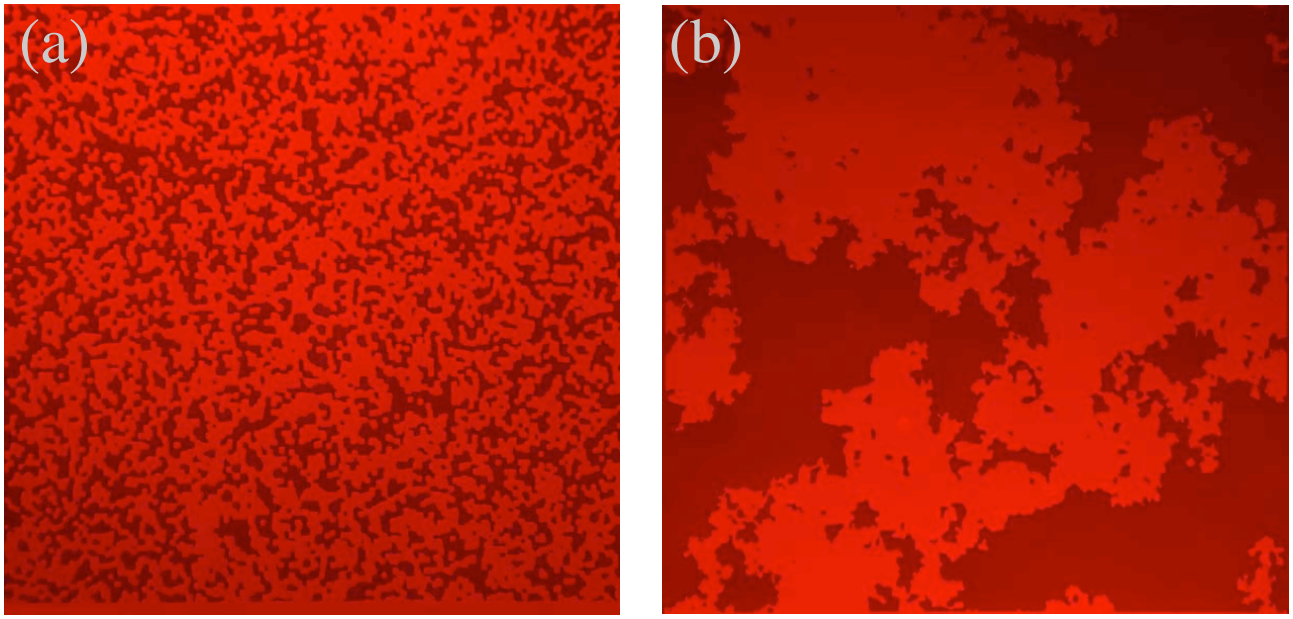

Figure 3.2.1 Examples of (a) spatially uncorrelated (Sample S8) and (b) spatially correlated (Sample S6) micro-models saturated with decane.

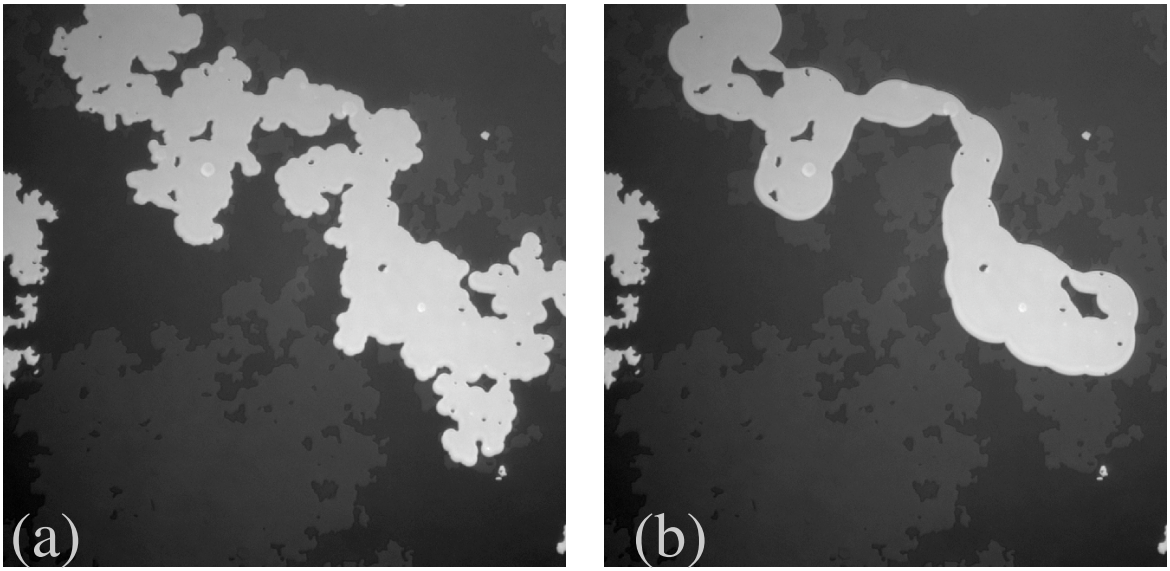

Figure 3.2.2 Photomicrographs of nitrogen gas (the brightest phase) as it displaces decane. The darkest regions are inaccessible to decane, while the phase of intermediate optical density is decane for sample S6 (same as Figure 3.2.1b). (a) Imbibition of nitrogen with a decane saturation of 55%; (b) Drainage of nitrogen with a decane saturation of 69%.

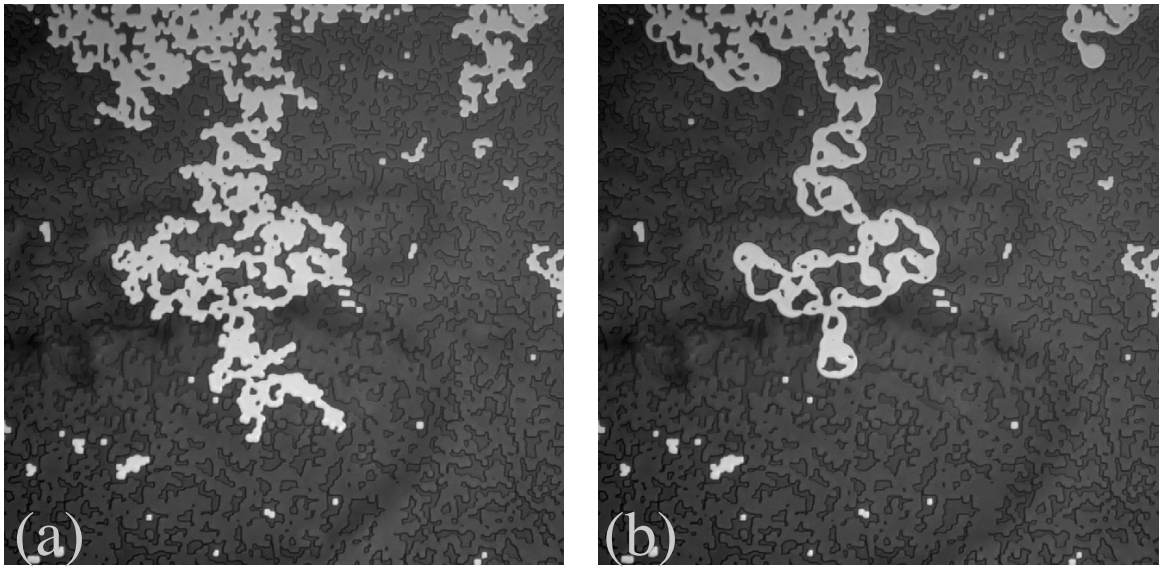

Figure 3.2.3 Photomicrographs of nitrogen gas (the brightest phase) as it displaces decane. The darkest regions are inaccessible to decane, while the phase of intermediate optical density is decane for sample S8 (same as Figure 3.2.1a). (a) Imbibition of nitrogen with a decane saturation of 74%; (b) Drainage of nitrogen with a decane saturation of 83%.

and the dark gray regions represent photoresist (solid regions where no flow can occur). Figure 3.2.3 contains images of Sample S8 (spatially uncorrelated) in the imbibition and drainage conditions. By comparing the shape of the nitrogen-decane interfaces between imbibition and drainage in the raw images shown in Figures 3.2.2 & 3.2.3, the potential importance of IAV can be discern. For example, during imbibition (Figures 3.2.2a & 3.2.3a) when the nitrogen is forced into the micro-model under pressure, the nitrogen-decane interface is "rough" and follows the geometry of the void space (Figure 3.2.1). However, as the pressure is reduced to drain the nitrogen (Figures 3.2.2b and 3.2.3b), the nitrogen-decane interface "smooths" out as the nitrogen retracts from the smallest pores. During drainage, the nitrogen-decane interface is more bulbous. A more quantitative description of the interfacial area per volume will be discuss later in this section.

3.2.2 Capillary Pressure - Saturation Relationship for the Micro-Models

For each micro-model several imbibition-drainage cycles were performed. These drainage-imbibition cycles can be considered more quantitatively using a plot of capillary pressure, P_{cap} , as a function of saturation, S. Here P_{cap} is the nitrogen pressure and S is the fraction of the accessible space which is filled with decane. In this work on the micro-models, nitrogen is the non-wetting phase relative to photoresist and decane. Decane is the wetting phase.

Figures 3.2.4 & 3.2.5 show the capillary pressure - saturation relationship for micro-models S6 (Figure 3.2.1b) and S8 (Figure 3.2.1a). The different symbols in Figures 3.2.4 & 3.2.5 show successive cycles for the samples. Within each cycle the pressure was increased in steps, and then held constant for on the order of 5 minutes before taking a photograph (as in Figures 3.2.2 & 3.2.3) from which the value of S was obtained through image analysis.

Different cycles could be realized by changing the size of the pressure steps and/or changing the speed with which the pressure was changed.

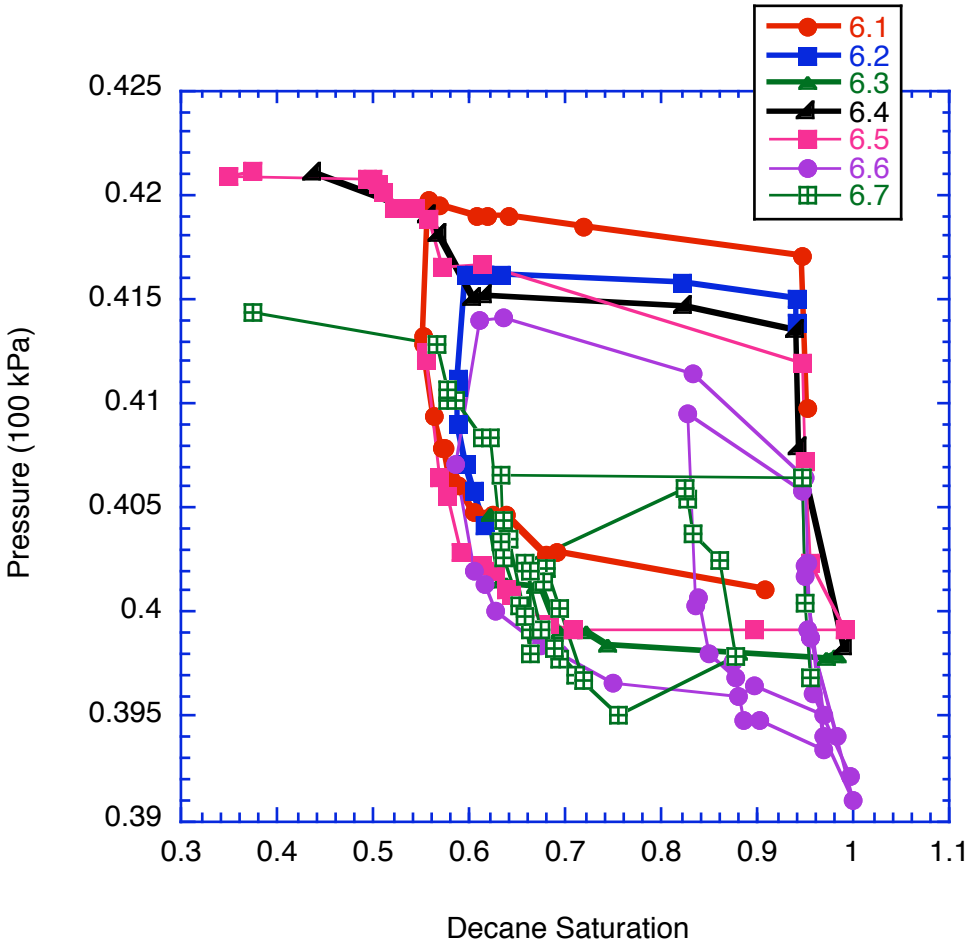

Figure 3.2.4. P_{cap} versus S for a series of drainage-imbibition cycles for the sample S6 in Figure 3.2.1b.

From Figures 3.2.4 & 3.2.5, it is observed that the capillary pressure - saturation behavior is hysteretic, as the system does not follow a unique trajectory in terms of pressure and saturation. Even the drainage and imbibition branches are not unique, i.e., the system does not follow a unique trajectory during drainage and the same is true during imbibition. Note that during these measurements, the flow rate was zero, as the nitrogen did not extend fully from the inlet side of the sample to the outlet side. However, the strong hysteresis implies that knowledge of pressure and saturation does not fully specify the state of the system.

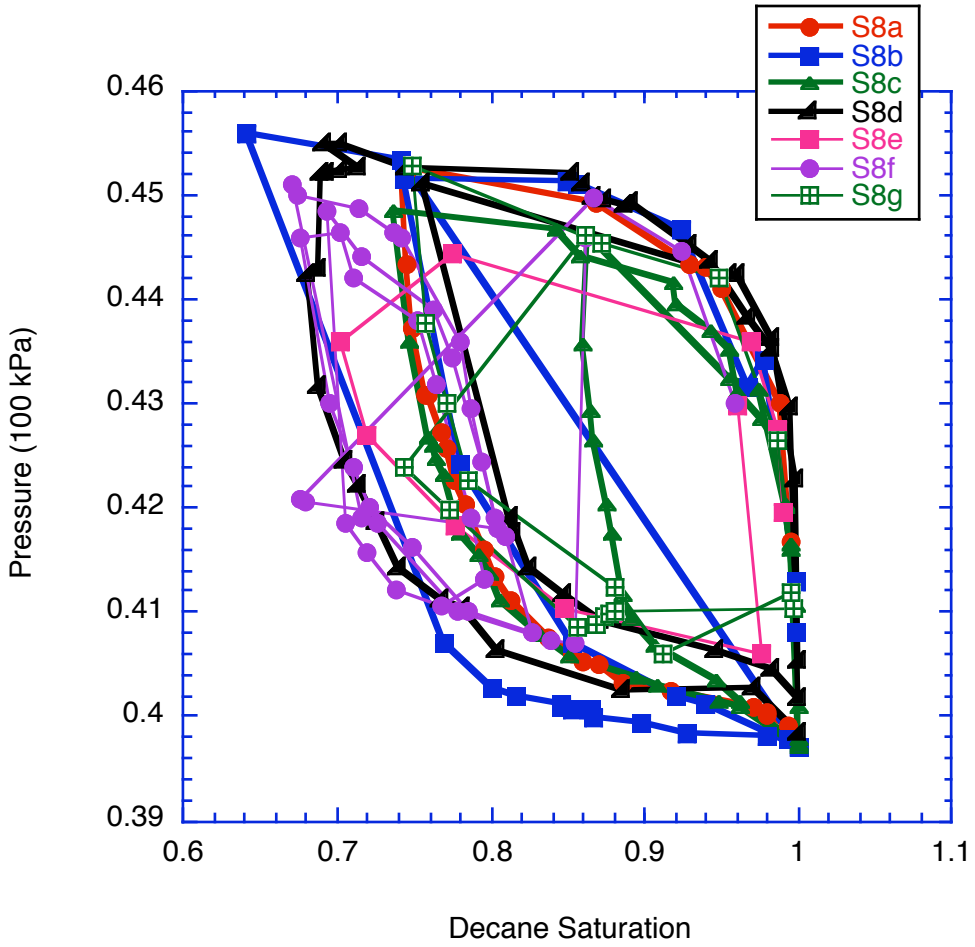

Figure 3.2.5. P_{cap} versus S for a series of drainage-imbibition cycles for the sample S8 in Figure 3.2.1a.

While several investigators [Rapoport, & Leas, 1951; Gvirtzman & Roberts, 1991; Powers et al., 1991; Bradford & F. J. Leij, 1997; Hassanizadeh & Gray, 1990; Gray & Hassanizadeh, 1991,1998ab] have recognized that an accurate description of multiphase flow in a porous medium must account for the thermodynamics and the geometry of the interfaces between the fluids (and between the fluids and the solid phase), these are properties that have eluded direct experimental measurement. Interfaces are hard to measure in a porous medium because they represent microscopic features at a small scale and usually are hidden from view. The physics of the interfaces enters as an interfacial area per volume (IAV), which when combined with capillary pressure and saturation is hypothesized to lead to a unique description of the thermodynamic energy state. If this approach is correct, the hysteretic relationship universally observed between capillary pressure and saturation for equilibrium conditions should be a unique and invertible relationship when interfacial area per volume is included as a third variable. The micro-models provide a unique opportunity to explicitly test this hypothesis.

3.2.3 *Interfacial Area per Volume for the Micro-Models*

The theoretical motivation for including interfacial area per volume in the capillary-pressure - saturation relationship is based on the way capillary pressures are defined on the pore scale and how they relate to the macroscale measurements of capillary pressures and saturations. On the pore scale, capillary pressure (p_c) between a wetting phase fluid and a non-wetting phase fluid is given by

$$p_c = \gamma^{wn}\left(\frac{1}{R_1} + \frac{1}{R_2}\right) = \gamma^{wn} J$$

where γ^{wn} is the interfacial tension between the wetting and non-wetting phase and J is the mean curvature of the interfaces based on the principal radii of curvature of the surface, R_1 and R_2. This definition shows how p_c depends on the geometry of the interfaces. Capillary pressure at equilibrium p_{ceq} can also be defined as a balances of forces between the fluids on either side of the interfaces and is defined as

$$p_{ceq} = p_n - p_w$$

where p_w and p_n are the pressures of the wetting and nonwetting phases, respectively. The equation for p_{ceq} is generally assumed to be applicable on the macroscale (core or field scale) as long as p_{ceq} is taken to be a function of the wetting phase saturation, S_w. However, it has been shown by numerous experimental investigations that p_{ceq} has a hysteretic relationship with saturation [Bear, 1979; Dullien, 1992]. Experiments have shown that the capillary pressure - saturation relationship depends on the drainage and imbibition history of the system and is not single valued. Hence, capillary pressure cannot be determined simply from saturation or vice-versa.

Muccino et al. [1998] hypothesized that the capillary-pressure - saturation relationship is a two-dimensional projection of a more extensive functional dependence, i.e., a third variable is needed to explicitly define the state of the system. They pointed out that the interfacial area per volume (IAV) is a parameter that includes the distribution of the fluid phases within the system. For any porous system with wetting and non-wetting phases, three interfacial areas can be defined: between the two fluid phases and between each fluid phase and the solid.

3.2.3.1 METHOD TO DETERMINE INTERFACIAL AREA PER VOLUME, CURVATURE OF INTERFACES AND NORMALS TO THE INTERFACES

Image analysis programs were written in IDL to extract phase saturation, interfacial area per volume (IAV), curvature of the interfaces and normals to the interfaces from images such as though shown in Figures 3.2.4 & 3.2.5. The first step in the analysis is to separate the image into three separate images, i.e., one binary image representing each phase (nitrogen, decane, and photoresist). The individual phase images are used to determine the fraction of the micro-model composed of each phase. The fraction of the micro-model composed of photoresist (i.e., the solid portion of the micro-model where no flow occurs) is constant for all drainage-imbibition cycles. Nitrogen and decane saturations of the pore space (i.e., non-photoresist regions of the micro-model) are calculated as a fraction of total pore space.

Once the saturation of each phase is determined, the interfacial length of each interface is determined. Three interfacial lengths are calculated: (i) between nitrogen and decane; (ii) between decane and photoresist; and (iii) between nitrogen and photoresist. Sobel and thinning operators are applied to each individual phase image at a given nitrogen pressure. The length of each interface is totaled. At this point in the analysis, the interfacial length from an individual phase image contains the phase in contact with both other phases. For example, for a nitrogen phase image, both the interface between nitrogen and decane and nitrogen and photoresist are included. The interface between two phases is obtained through the following relationships:

$$L_{nd} = L_n + L_d - L_p$$
$$L_{np} = L_n + L_p - L_d$$
$$L_{dp} = L_d + L_p - L_n$$

where is L_n is the length of the nitrogen interface, L_d and L_p are the lengths of the decane and photoresist interfaces, respectively. L_{nd} is the length of the interface between nitrogen and decane. L_{np} is the length of the interface between nitrogen and photoresist. L_{dp} is the length of the interface between decane and photoresist.

The curvature of the interfaces and the normal to the interfaces are calculated using level set methods (Sethian, 1985). The curvature is obtained from the image using:

$$K = \frac{\Phi_y^2\Phi_{xx} - 2\Phi_x\Phi_y\Phi_{xy} + \Phi_x^2\Phi_{yy}}{(\Phi_x^2 + \Phi_y^2)^{3/2}}$$

where K is the curvature of the interface. Φ_i is the derivative of the image with respect to i where i is either x or y. Φ_{ii} is the second derivative of the image with respect to ii where ii can be xx, yy or xy. The derivatives of the two dimensional images are taken using a kernel method. Because of ambiguities in the gray images, the curvature analysis is performed on the phase image convolved with a gaussian blur of the image. This provides a gray scale or gradient at each interface so derivatives can be taken. After computing the curvature, a mask

of the interface relevant to each phase is applied. This results in a two-dimensional array containing the curvature of the interfaces for a given image.

Computation of the normals to the interfaces was also performed. Theoretical models assume that the interfaces between each fluid (as well as each fluid and the solid) are randomly distributed. A random distribution of the normals makes the application of averaging theorems for upscaling relative permeability more tractable. The calculation of the normals begins by using the following equations:

$$n_x = \frac{\Phi_x}{\sqrt{\Phi_x^2 + \Phi_y^2}}$$

$$n_y = \frac{\Phi_y}{\sqrt{\Phi_x^2 + \Phi_y^2}}$$

and then applying

$$n_{xx} = \text{Image} \times n_x n_x$$

$$n_{yy} = \text{Image} \times n_y n_y$$

$$n_{xy} = \text{Image} \times n_x n_y$$

where n_{xx}, n_{yy} and n_{xy} are the normals to the interfaces and image is a two-dimensional image of the interface between two phases.

3.2.3.2 Interfaces, Curvature and Normal Analysis of Interfaces

The experiments on the micro-models start with the micro-model saturated with decane, i.e., the wetting phase. This means that the models are "pre-wetted" and a thin film of wetting phase might always be present. In our micro-models, we had a resolution of 0.6 microns per pixels, yet we could not easily delineate thin films. We performed the image analysis of our data in two ways: (1) assuming that a thin film of wetting fluid always exists; and (2) the a thin film of wetting fluid can be ignore. By assuming condition (1), the IAV_{ws} between the wetting phase (decane) and the solid is constant but the IAV_{ns} between the non-wetting phase (nitrogen) and the solid is equal to zero. Only IAV_{wn} between the wetting and non-wetting phases varies with pressure and saturation. By assuming condition (2), IAV_{ws} IAV_{ns} and IAV_{wn} vary as a function of pressure and saturation.

Figures 3.2.6 & 3.2.7 are images of smaples S6 and S8, respectively, that show the nitrogen-decane interface assuming conditions (1) and (2). In Figures 3.2.6 & 3.2.7, black represents the photoresist, red represents the nitrogen and blue represents decane. The interfaces indicated in white are the capillary-dominated interfaces, i.e. the interfaces between bulk fluids. The interfaces indicated in bright red represent the interface between nitrogen and a thin film of decane (condition 1). Figures 3.2.6 & 3.2.7 represent only a quarter of the micro-model images so details of the interfaces can be observed. From visual inspection, it is clear that the interfacial geometry between nitrogen and decane is very different depending on whether nitrogen is imbibed into the sample or drained.

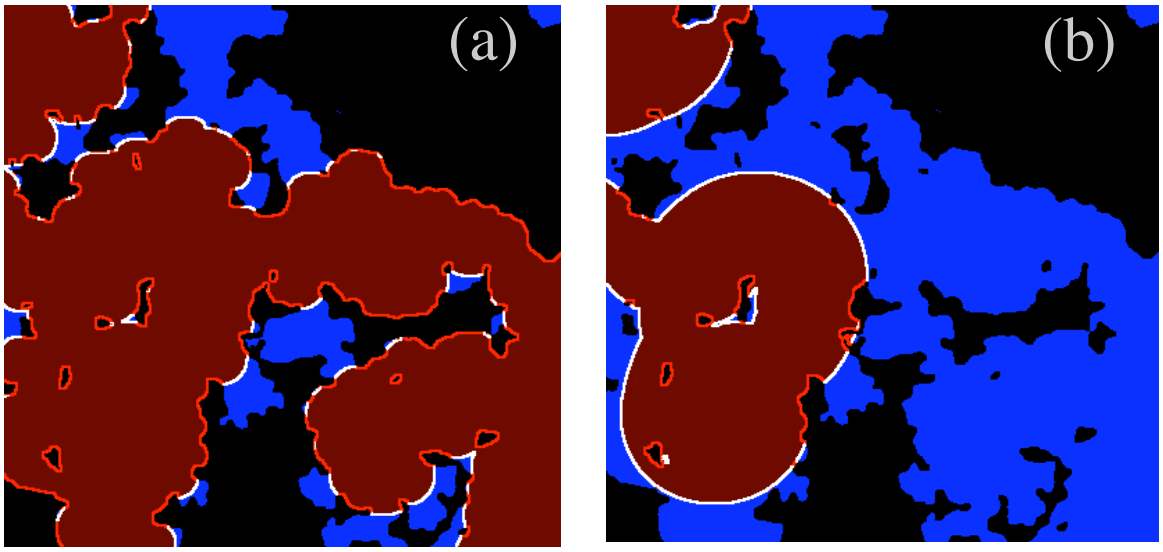

Figure 3.2.6. An image of one-quarter of micro-model sample S6 partially saturated with decane (blue) and nitrogen (maroon) during drainage. Photoresist is represented by the black regions. The capillary-dominated interfaces are shown in white, and the disjoining-pressure dominated interfaces are shown in light red. (a) Imbibition and (b) Drainage.

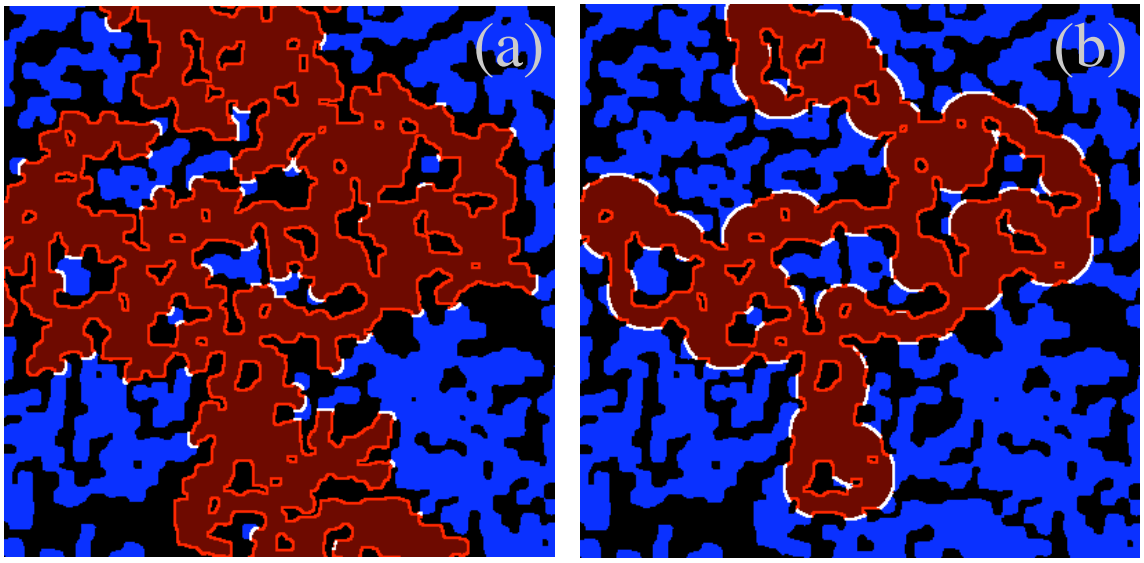

Figure 3.2.7. An image of one-quarter of a micro-model sample S8 partially saturated with decane (blue) and nitrogen (maroon) during drainage. Photoresist is represented by the black regions. The capillary-dominated interfaces are shown in white, and the disjoining-pressure dominated interfaces are shown in light red. (a) Imbibition and (b) Drainage.

The histograms of the curvatures of the interfaces for sample S6 and S8 are shown in Figure 3.2.8. The histogram is based on the full image not just the quarter image as shown in Figure 3.2.6 or Figure 3.2.7. The histogram for the full set of nonwetting interfaces is shown

along with one subset: the subset of capillary-dominated, nonwetting-wetting interfaces (interfaces between bulk fluids). The striking feature that emerges in Figure 3.2.8 is the differentiation of the curvature. The subset of nonwetting-wetting interfaces has a nearly unique negative curvature (by convention), while the nonwetting-solid interfaces has a broad distribution of curvatures, many of which are positive. Furthermore, the average curvature of the nonwetting-wetting interface agrees with measurements of capillary pressure (Figure 3.2.9).

These results present an important finding of our micro-model and interface visualization work with regard to the critical issue of thin films and their role in porous media. Because we are invading into a pre-wet micro-model, a thin film of wetting phase remains between the non-wetting phase and the photoresist. Hence, there are strictly only two interfaces: between the non-wetting phase and the wetting phase which changes during imbibition-drainage cycles, and that between the wetting phase and the photoresist which is constant throughout the experiment. However, the lateral optical resolution (0.6 microns) of the imaging system prevents direct resolution of the thin film. In this context, it is evident that the striking difference between the curvature distributions presents a means of distinguishing between the physical processes that dominate the interfaces. For instance, the non-wetting-wetting interface can be divided unambiguously into two subsets, one that is dominated by capillary pressure (the narrow peak), and the other that is dominated by disjoining pressure associated with the proximity of the solid interface (Deriagin et al., 1987). The capillary-dominated interface is the interface between bulk fluids, while the disjoining-pressure-dominated interface is the interface between a bulk fluid and a fluid film. As is presented in the next section, it is the interfacial area per volume of the capillary dominated interfaces that removes the ambiguity in the capillary pressure - saturation relationship.

Finally, the mean values of the normals to the interface between the nitrogen and decane (based on condition 2) for samples S6 and S8 are:

$$\begin{pmatrix} n_{xx} & n_{xy} \\ n_{yx} & n_{yy} \end{pmatrix} = \begin{pmatrix} 0.47 & 0.011 \\ 0.011 & 0.51 \end{pmatrix}$$

$$\begin{pmatrix} n_{xx} & n_{xy} \\ n_{yx} & n_{yy} \end{pmatrix} = \begin{pmatrix} 0.40 & 0.013 \\ 0.013 & 0.51 \end{pmatrix}$$

which indicates that the interfaces are roughly randomly oriented. A random distribution of the normals makes the application of averaging theorems for upscaling relative permeability more tractable.

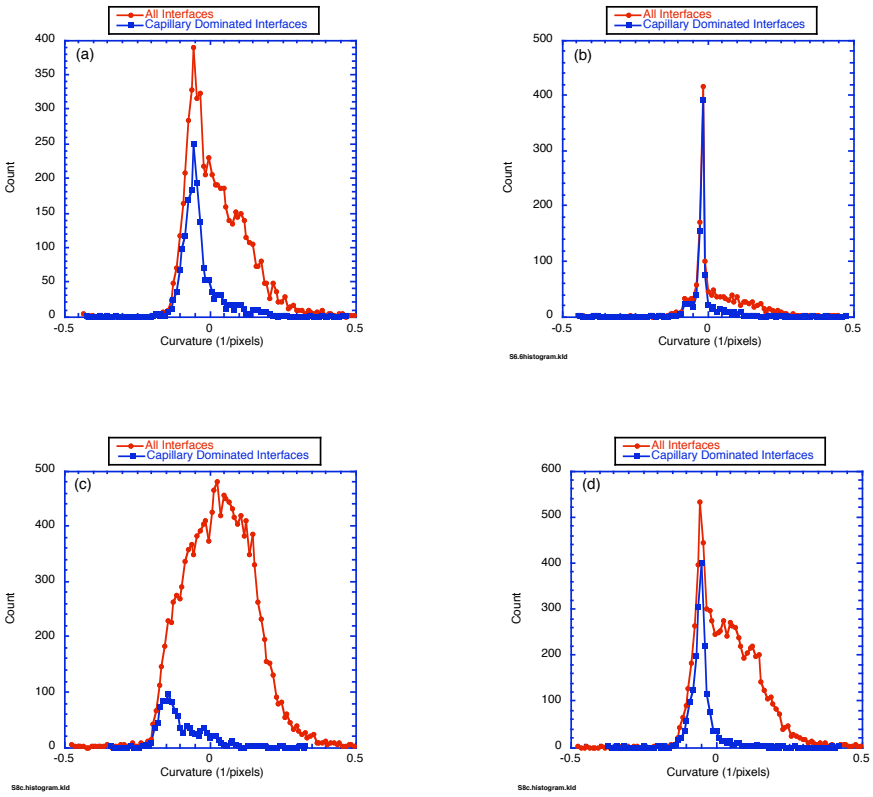

Figure 3.2.8. The histograms of the curvatures of the interface between nitrogen and decane are for the all interfaces (red) and for the subset that is capillary dominated (blue) for (a) Sample S6 for imbibition; (b) Sample S6 for drainage; (c) Sample S8 for imbibition; and (d) Sample S8 for drainage.

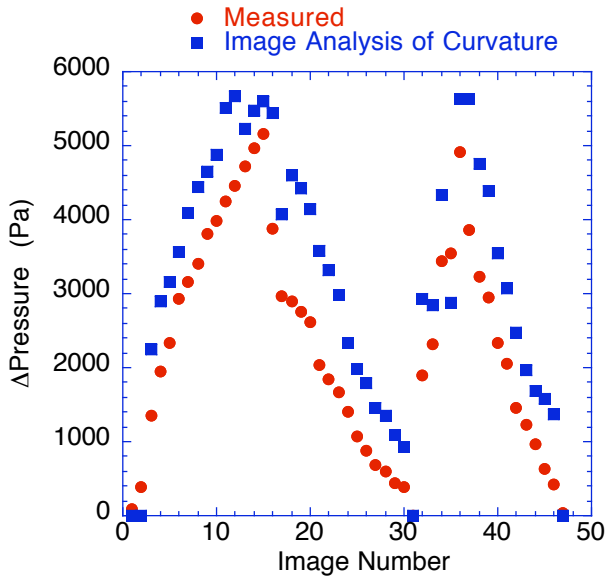

Figure 3.2.9 Comparison of capillary pressures measured with pressure transducer (red) and that calculated from image analysis (blue).

3.2.4 Capillary Pressure - Saturation -Interfacial Area per Volume Relationship

Several investigators (Rapoport & Leas, 1951; Gvirtzman & Roberts, 1991; Bradford & F. J. Leij, 1997; Hassanizadeh & Gray, 1990; Gray & Hassanizadeh, 1991,1998ab) have recognized that an accurate description of multiphase flow in a porous medium must account for the thermodynamics and the geometry of the interfaces between the fluids and between the fluids and the solid phase. Fluid flow and the distribution of multiple fluid phases are controlled by the movement of the interfaces that results from changes in pressure and saturation. The physics of the interfaces is accounted for in these theories by explicitly introducing interfacial area per volume in combination with capillary pressure and saturation as an indicator of the thermodynamic energy state. Based on this hypothesis, the hysteretic relationship univerally observed between capillary pressure and saturation for equilibrium conditions should be a unique and invertible relationship when interfacial area per volume is included. In this section, we present the results and discussion of the role of IAV in the capillary pressure - saturation relationship.

3.2.4.1 Interfacial Area per Volume assuming a Thin Film of Wetting Fluid is always Present.

As described in section 3.2.3.2, the micro-models are initially saturated with the wetting phase, i.e., decane. We performed our analysis of the role of IAV in the capillary pressure - saturation relationship in two ways: (1) assuming that a thin film of wetting fluid always exists; and (2) the a thin film of wetting fluid can be ignore. In this section, we present the results of our study based on codition (1) and the results for condition (2) can be found in section 3.2.4.2.

By assuming condition (1), the IAV_{ws} between the wetting phase (decane) and the solid is constant but the IAV_{ns} between the non-wetting phase (nitrogen) and the solid is equal to zero. Only IAV_{wn} between the wetting and on-wetting phases varies with pressure and saturation. Figures 3.2.10-3.2.13 show the relationship among capillary pressure, saturation and interfacial area per volume for condition 1 for samples S6 and S8. Figures 3.2.10 & 3.2.12 show the surface defining the relationship among capillary pressure, saturation and interfacial area per volume for condition 1. The surface is smooth and single-valued. However, when the two-dimensional projections of the three-dimensional surface are examined (Figures 3.2.11 & 3.2.13), it is found that for condition (1), IAV between the wetting and non-wetting phases provides no additional information, i.e., the relationship between IAV_{wn} and saturation is linear. Thus, if a thin film of wetting fluid always exists, measurement of IAV does not lift the ambiguity in the capillary pressure - saturation relationship. However, by assuming a film of wetting fluid always exists, we are mixing fluid-fluid interfaces that are controlled by different microscale mechanisms, i.e. capillary dominated interfaces and disjoining pressure dominated interfaces. In the next section (3.2.4.2), we present our findings when we limit our analysis to interfaces dominated only by capillary forces.

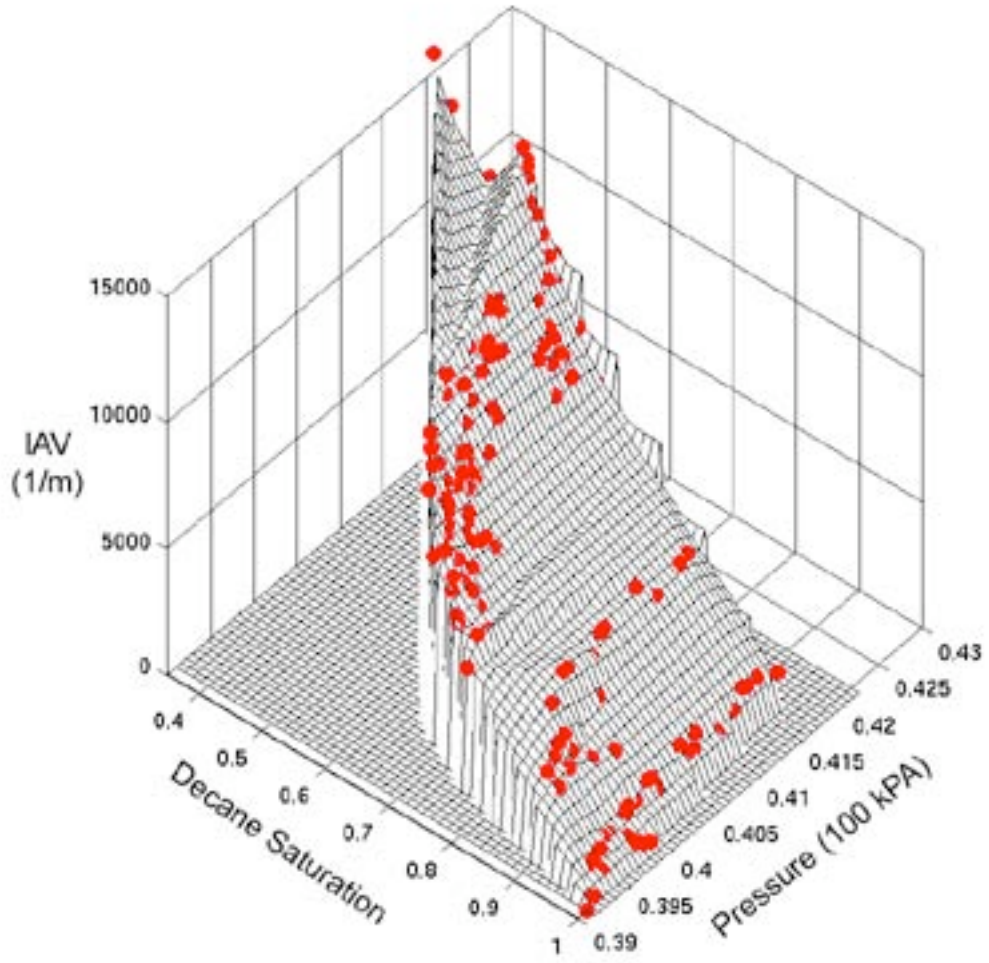

Figure 3.2.10 Interfacial area surface as a function of Pressure and Saturation for sample S6. These results were obtained during the drainage-imbibition cycles shown in Figure 3.2.4.

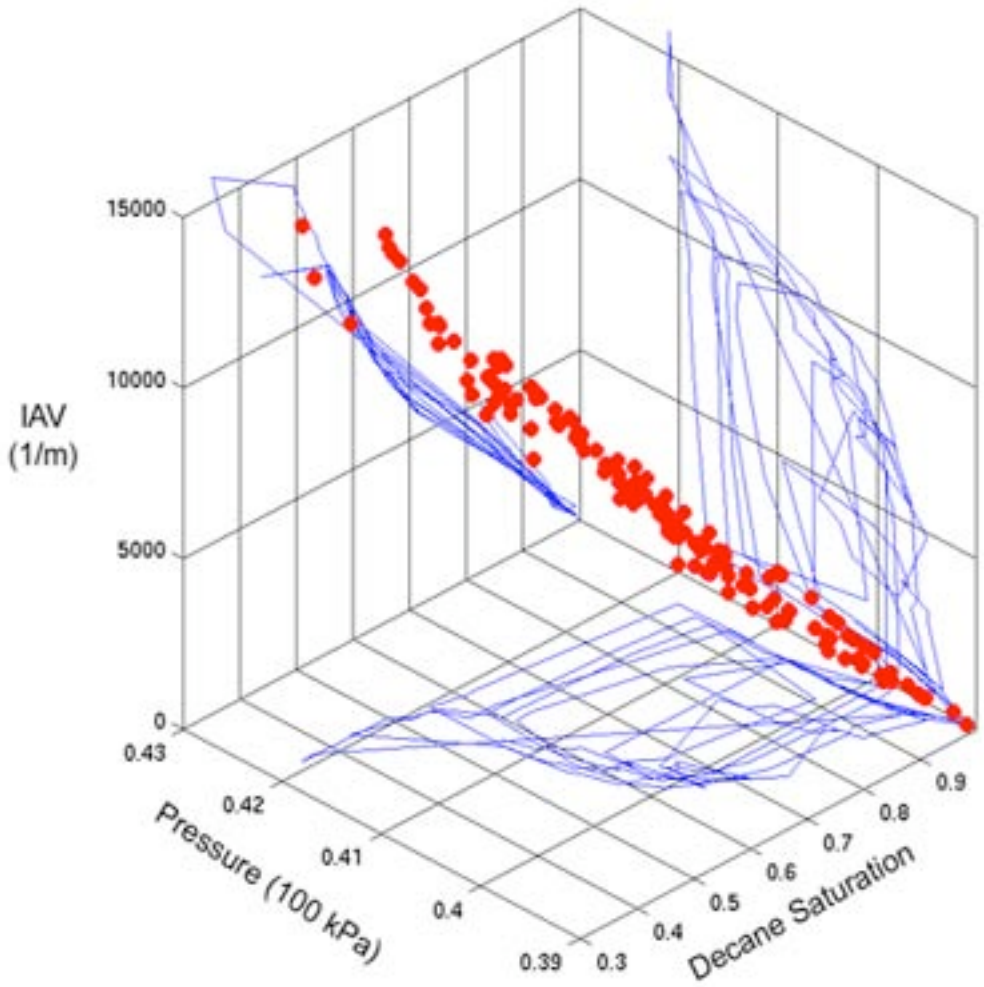

Figure 3.2.11 Interfacial area surface as a function of Pressure and Saturation for sample S6 obtained during the drainage-imbibition cycles shown in Figure 3.2.4. The data points are the same as those on shown in Figure 3.2.10 but the axes are rotated to show the lack of strong hysteresis in the projection of IAV - Saturation.

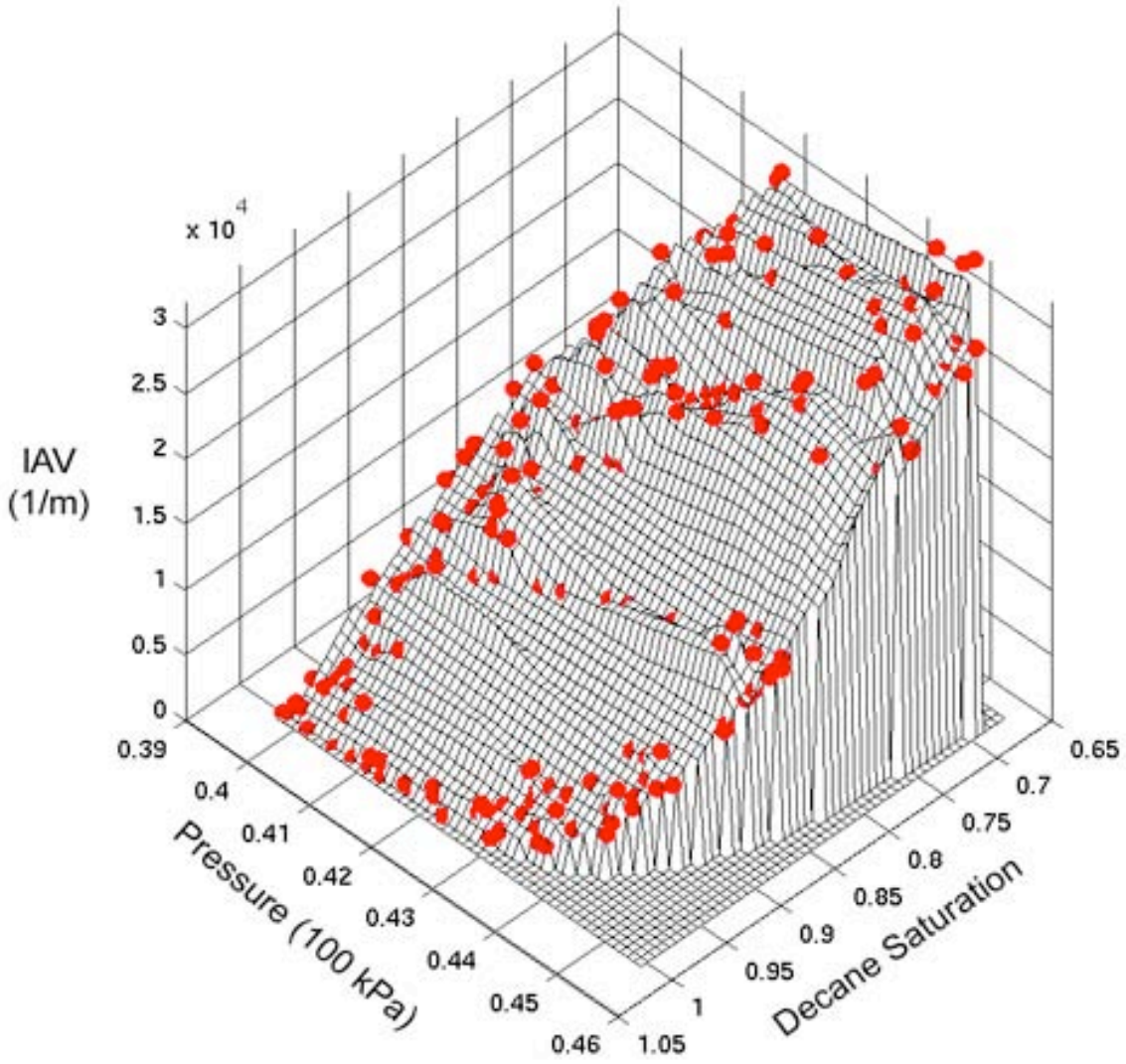

Figure 3.2.12 Interfacial area surface as a function of Pressure and Saturation for sample S8. These results were obtained during the drainage-imbibition cycles shown in Figure 3.2.5.

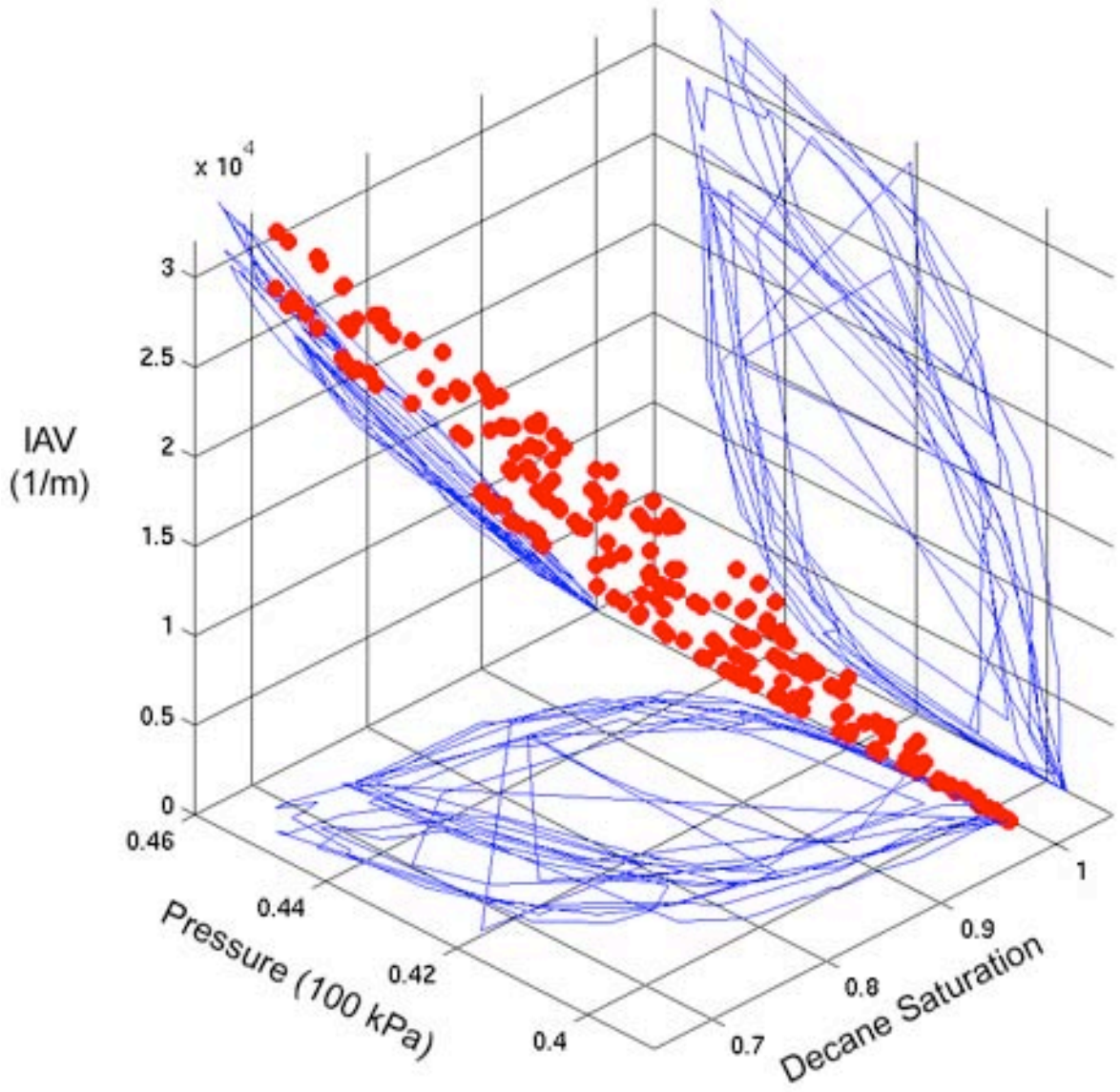

Figure 3.2.13. Interfacial area surface as a function of Pressure and Saturation for sample S8 obtained during the drainage-imbibition cycles shown in Figure 3.2.5. The data points are the same as those on shown in Figure 3.2.12 but the axes are rotated to show the lack of strong hysteresis in the projection of IAV - Saturation.

3.2.4.2 Interfacial Area per Volume for Capillary-Dominated Interfaces

As presented in section 3.2.3.2, capillary-dominated interface (i.e., interfaces between bulk fluids) are a distinct subset of all wetting-nonwetting interfaces and the distinction is based on the curvature of the capillary-dominated interfaces (Figure 3.2.8). The capillary-dominated interfacial area per volume (IAV between nitrogen and decane) values for samples S6 and S8 are shown in Figures 3.2.14-3.2.17 as functions of pressure and saturation along with all three 2D projectionsx. Although each 2D projection (Figures 3.2.15 & 3.2.17) of

the surface is hysteretic (P vs. S, IAV vs. S, and IAV vs. P), the surface is invertible: for a given degeneracy between two data points in P and S, the IAV differentiates between them. In other words, given any two measured parameters, the third can be found uniquely. Furthermore, the surfaces are unique for a given percolation pattern. When multiple data fall within small regions of the P-S plane, regardless from which of numerous cycles, we find they have similar IAV to within 5%. Different patterns will have different IAV surfaces, and hence the surfaces are not "universal", but the invertibility for each pattern provides a powerful new tool for the study of porous media. These results provide initial support for the theoretical and numerical arguments that IAV (between wetting and non-wetting phases) must be treated as a state variable in descriptions of multiphase flow. The work described here represents a fundamental advance in the field that will lead to important new insights into multiphase fluid flow in many types of random media across many disciplines

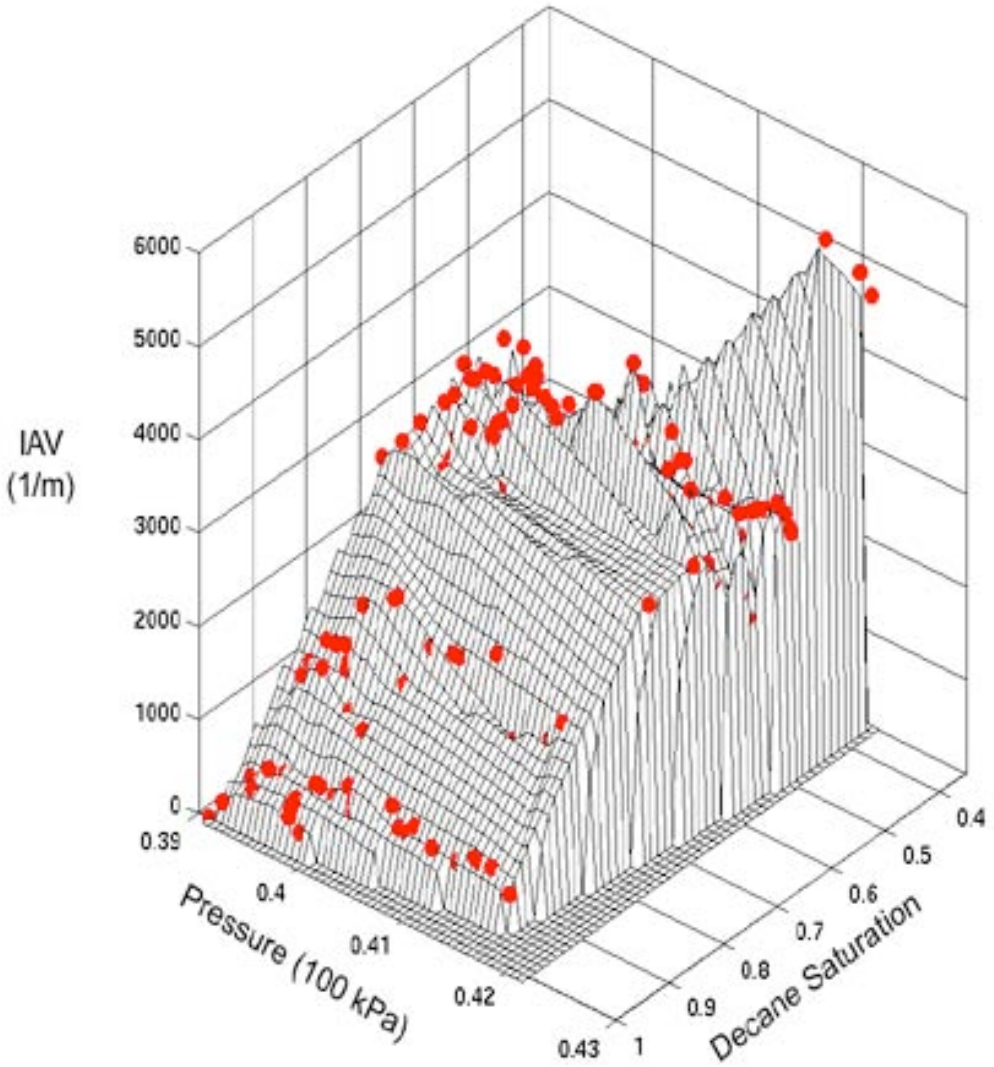

Figure 3.2.14. Interfacial area surface as a function of Pressure and Saturation for sample S6 using only capillary-dominated interfaces. These results were obtained during the drainage-imbibition cycles shown in Figure 3.2.4. The IAV is between the wetting phase (decane) and the non-wetting phase (nitrogen).

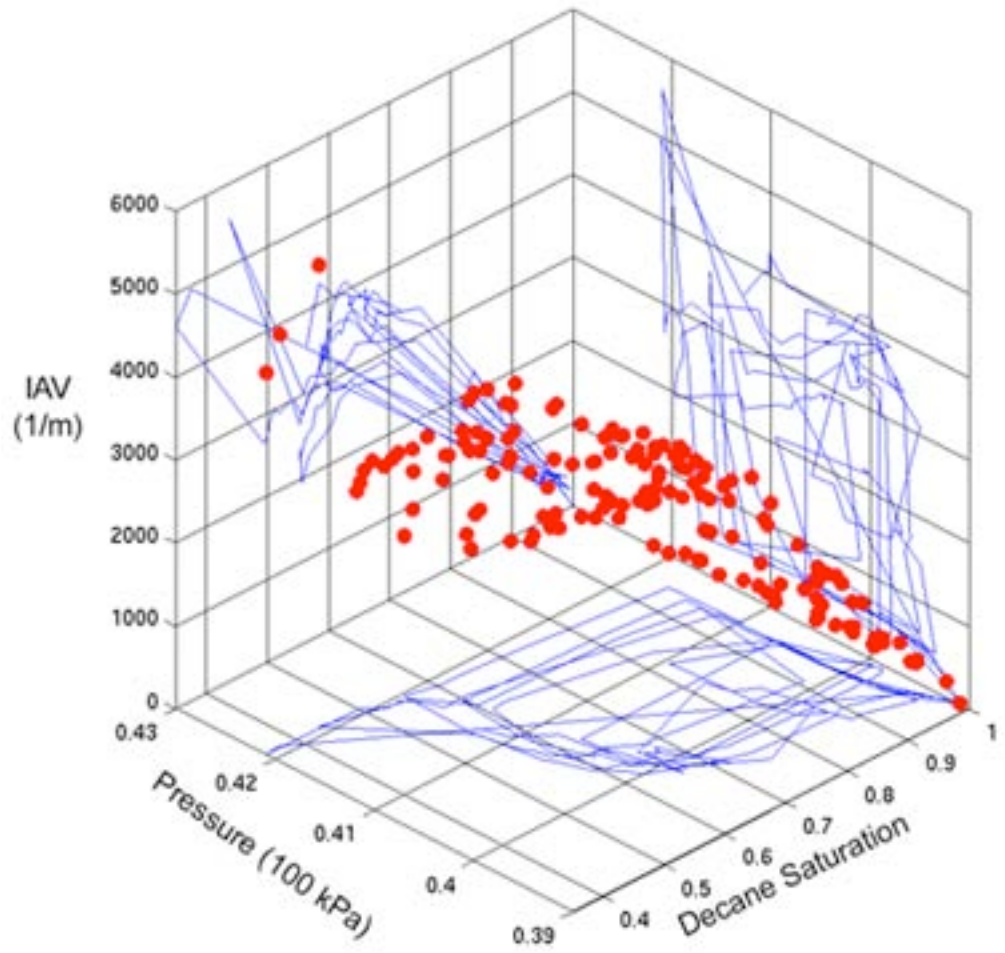

Figure 3.2.15 Interfacial area surface as a function of Pressure and Saturation for sample S6 obtained during the drainage-imbibition cycles shown in Figure 3.2.4 using only capillary-dominated interfaces. The data points are the same as those on shown in Figure 3.2.14 but the axes are rotated to show the strong hysteresis in all two-dimensional projections. The IAV is between the wetting phase (decane) and the non-wetting phase (nitrogen).

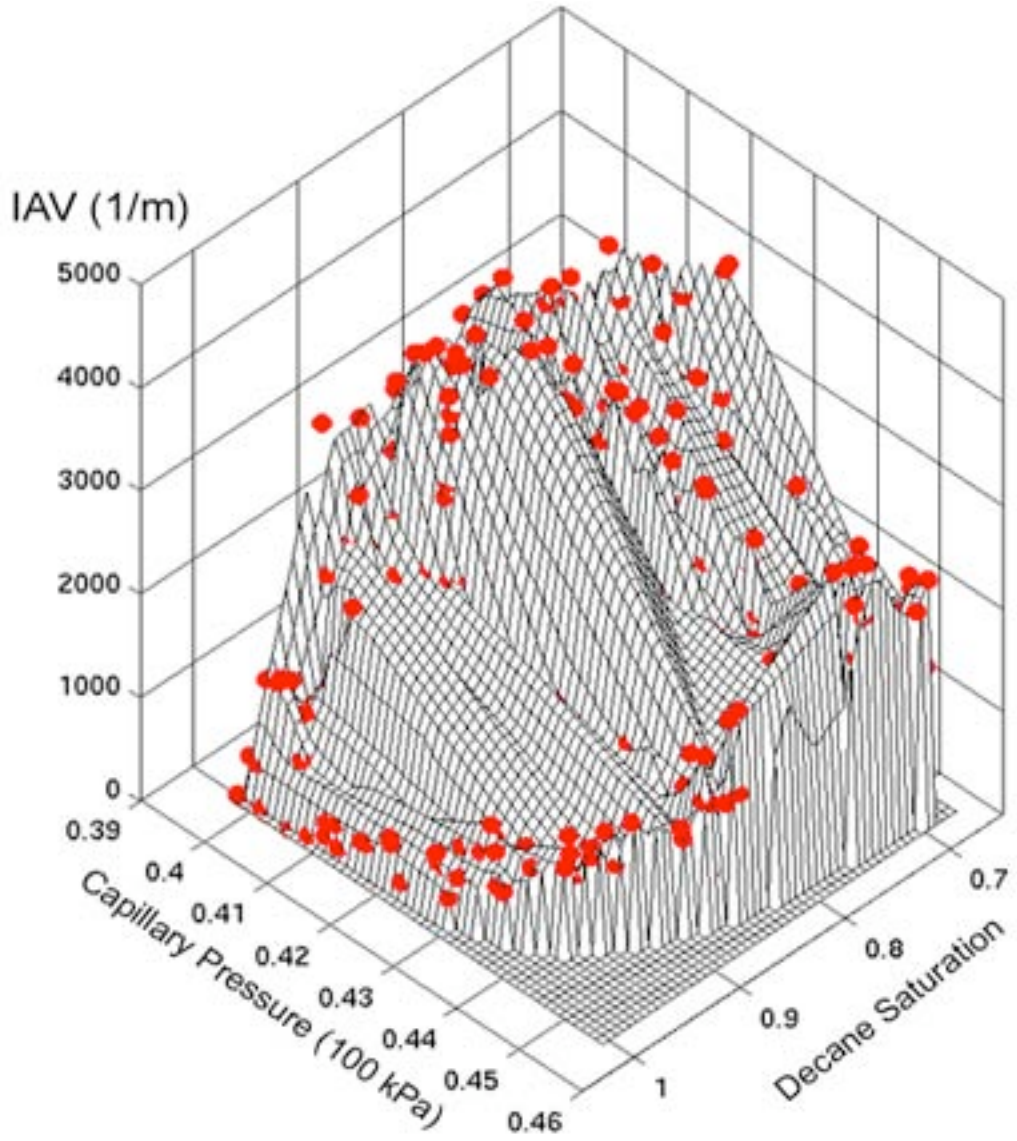

Figure 3.2.16 Interfacial area surface as a function of Pressure and Saturation for sample S8 using only capillary-dominated interfaces. These results were obtained during the drainage-imbibition cycles shown in Figure 3.2.5. The IAV is between the wetting phase (decane) and the non-wetting phase (nitrogen).

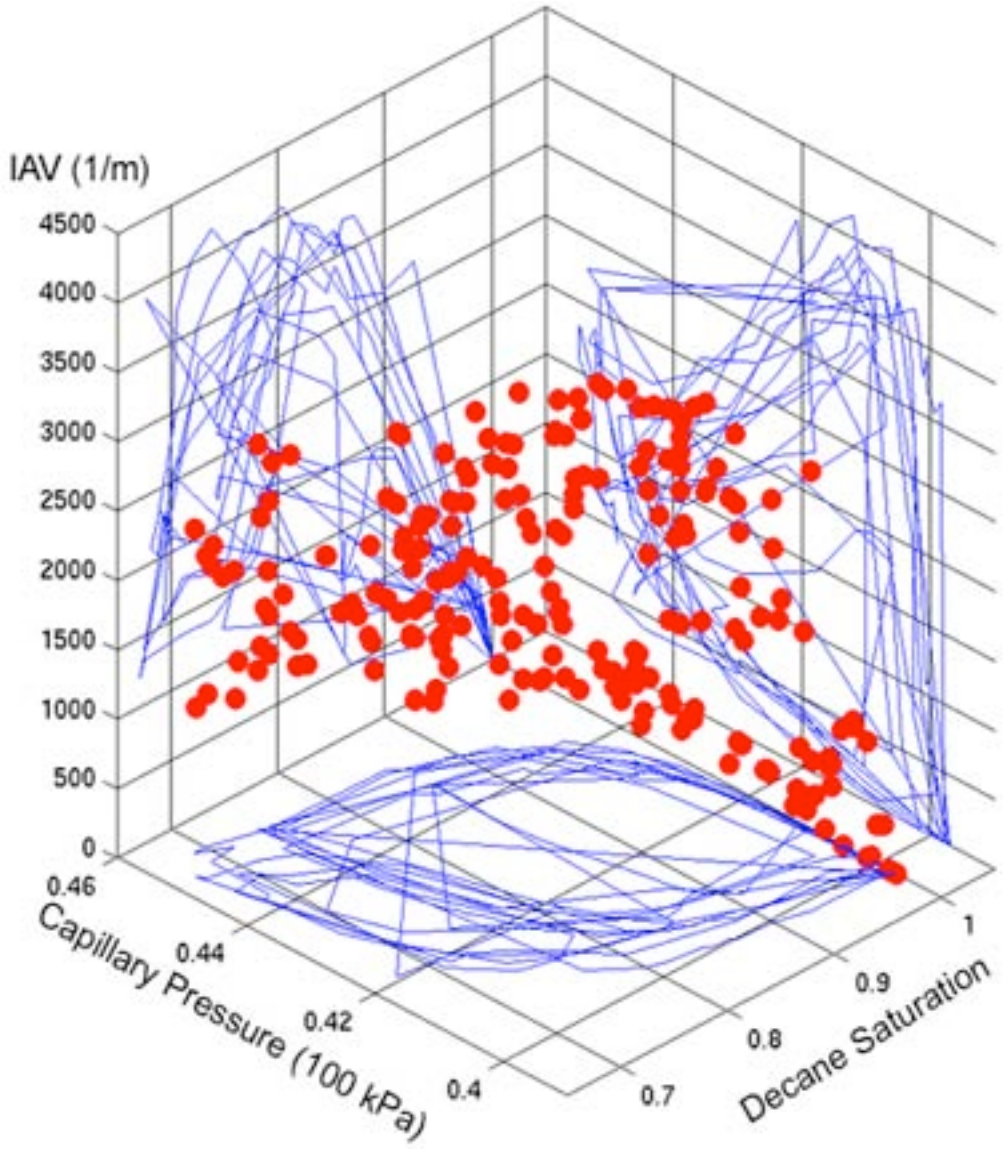

Figure 3.2.17 Interfacial area surface as a function of Pressure and Saturation for sample S8 obtained during the drainage-imbibition cycles shown in Figure 3.2.5 using only capillary-dominated interfaces. The data points are the same as those on shown in Figure 3.2.16 but the axes are rotated to show the strong hysteresis in all two-dimensional projections. The IAV is between the wetting phase (decane) and the non-wetting phase (nitrogen).

3.2.4.3 Interfacial Are per Volume for the Interfaces between each Fluid phase and the Solid for the Capillary-Dominated Condition

For completeness, we present results from the study of the interfaces between each fluid phase and the solid for condition (2), i.e., assuming no thin film exists. This analysis is not performed for condition (1) (i.e., a thin wetting film always exist) because by assuming condition (1), IAV_{ws} is constant and IAV_{ns} is equal to zero.

Figures 3.2.18 & 3.2.19 contain the surface for the relationship among capillary pressure, saturation and IAV between the wetting phase and the solid for samples S6 and S8. While, Figures 3.2.20 & 3.2.21 show the surface for the relationship among capillary pressure, saturation and IAV between the non-wetting phase and the solid for samples S6 and S8. The interfacial area per volume between the wetting phase and the solid is roughly three times greater than the IAV between the non-wetting phase and the solid.

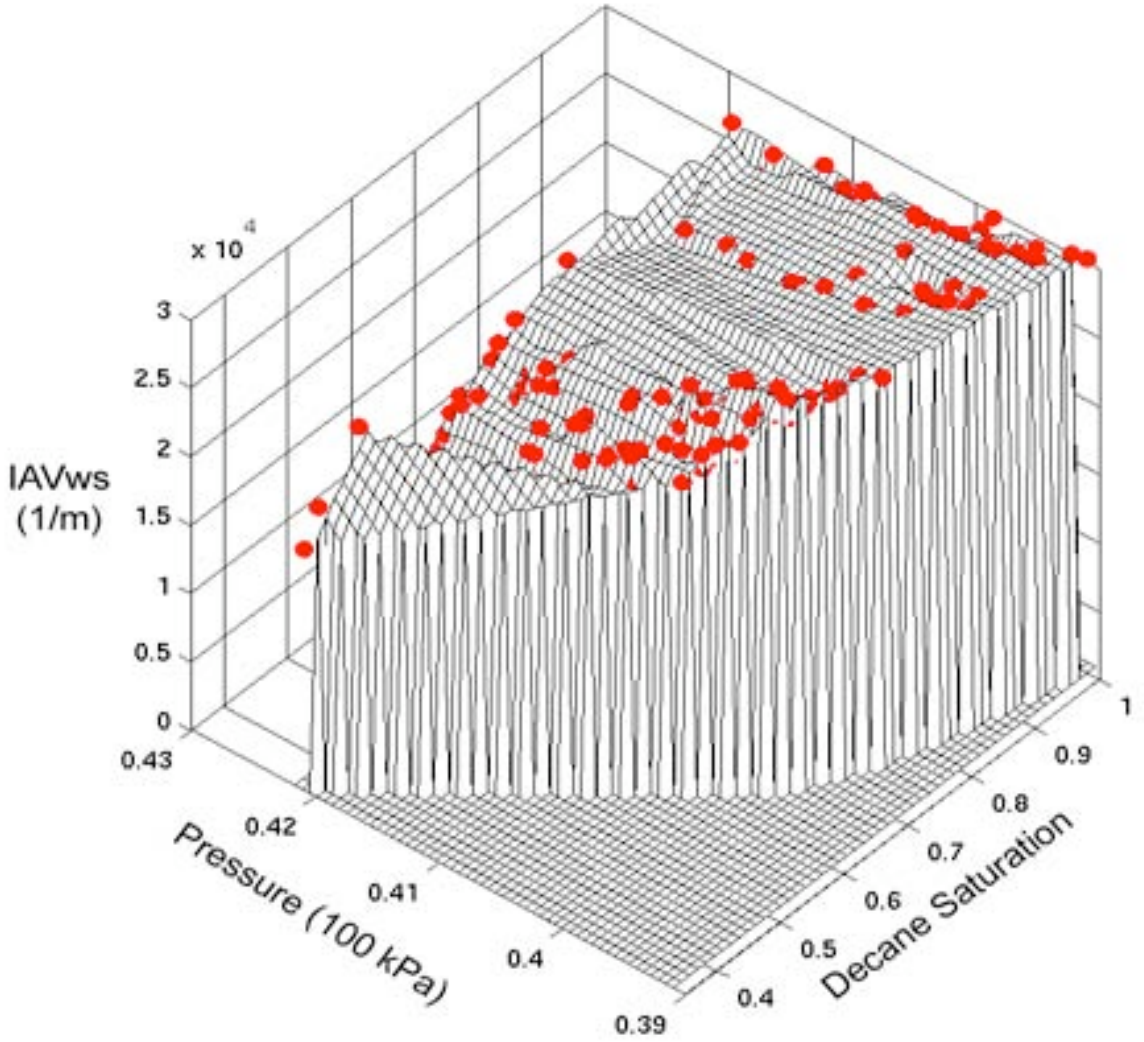

Figure 3.2.18. The surface representing the relationship among capillary pressure, saturation and interfacial area per volume for the interface between the wetting phase (decane) and the solid for sample S6 obtained during the drainage-imbibition cycles shown in Figure 3.2.4.

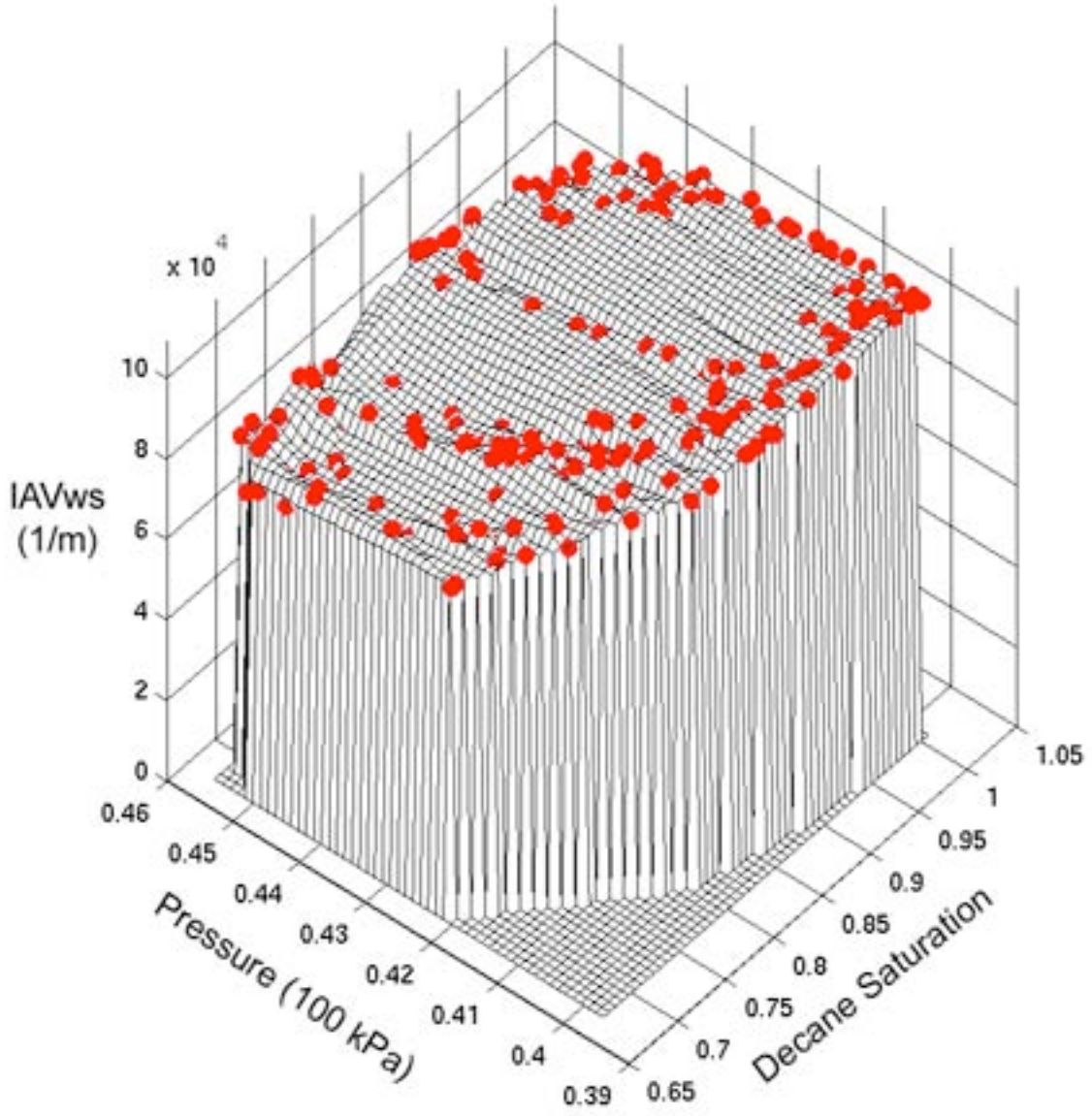

Figure 3.2.19 The surface representing the relationship among capillary pressure, saturation and interfacial area per volume for the interface between the wetting phase (decane) and the solid for sample S8 obtained during the drainage-imbibition cycles shown in Figure 3.2.5.

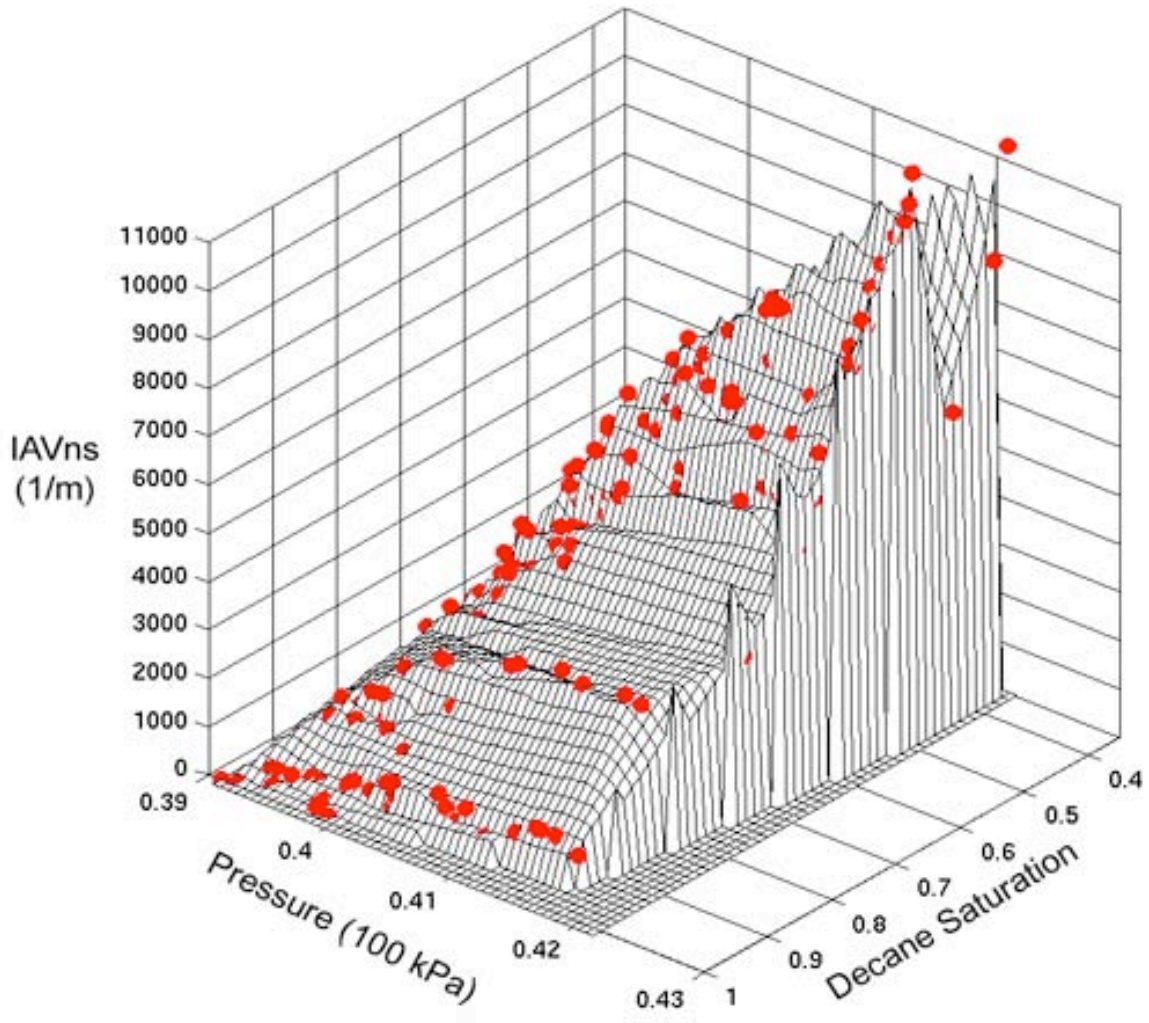

Figure 3.2.20 The surface representing the relationship among capillary pressure, saturation and interfacial area per volume for the interface between the non-wetting phase (nitrogen) and the solid for sample S6 obtained during the drainage-imbibition cycles shown in Figure 3.2.4.

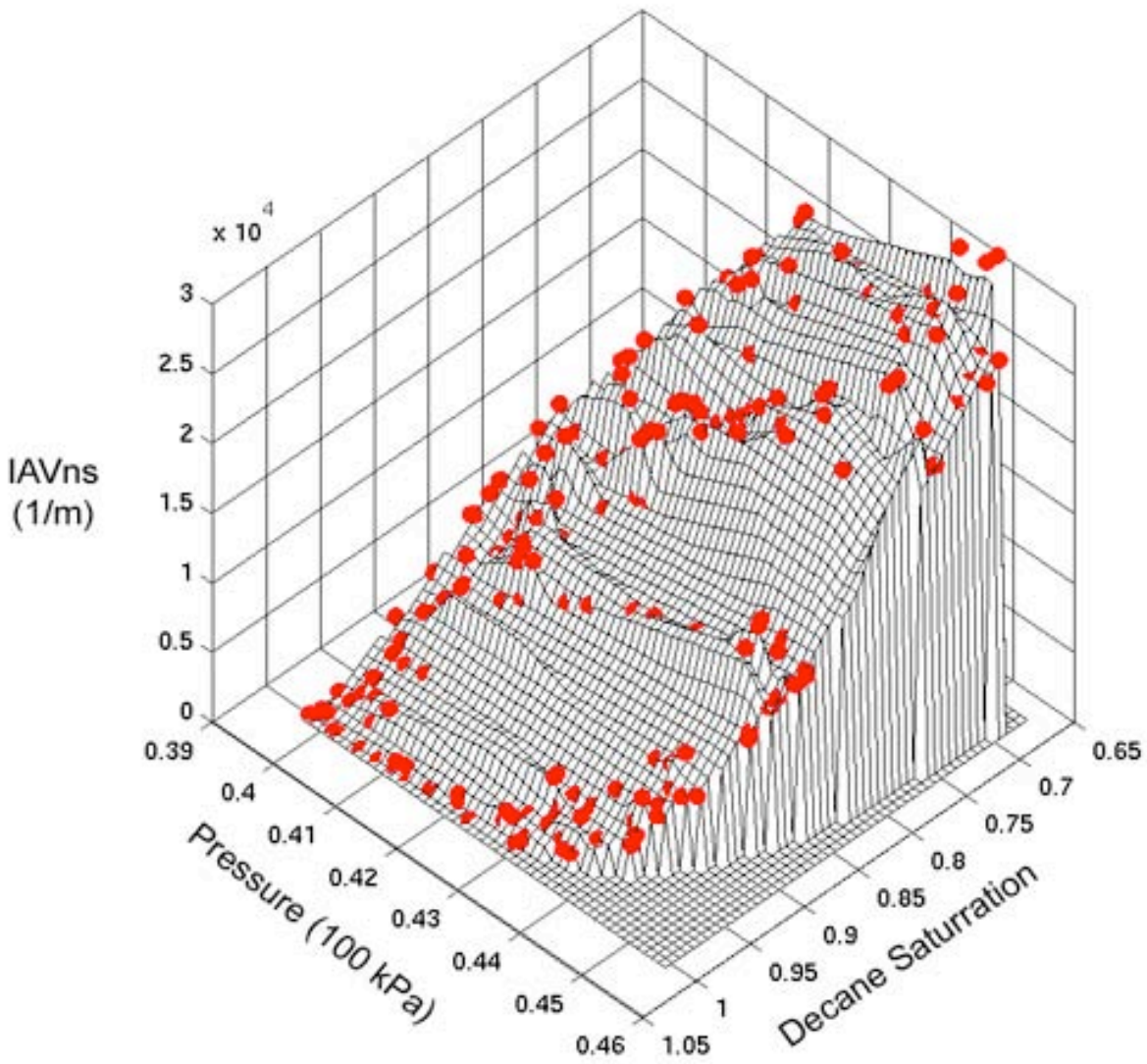

Figure 3.2.21 The surface representing the relationship among capillary pressure, saturation and interfacial area per volume for the interface between the non-wetting phase (nitrogen) and the solid for sample S8 obtained during the drainage-imbibition cycles shown in Figure 3.2.5

3.3 WOOD'S METAL METHOD

The Wood's metal injection method was used to acquire interfacial area per volume (IAV) data for sandstone cores with the goal of comparing them with the results of the micromodel work. This required destructive sectioning (see section 2.3.1.2) of the core after the sample had been injected with Wood's metal. To find reliable IAV values, many images of the sample were used to discern the different phases filling the pore space.

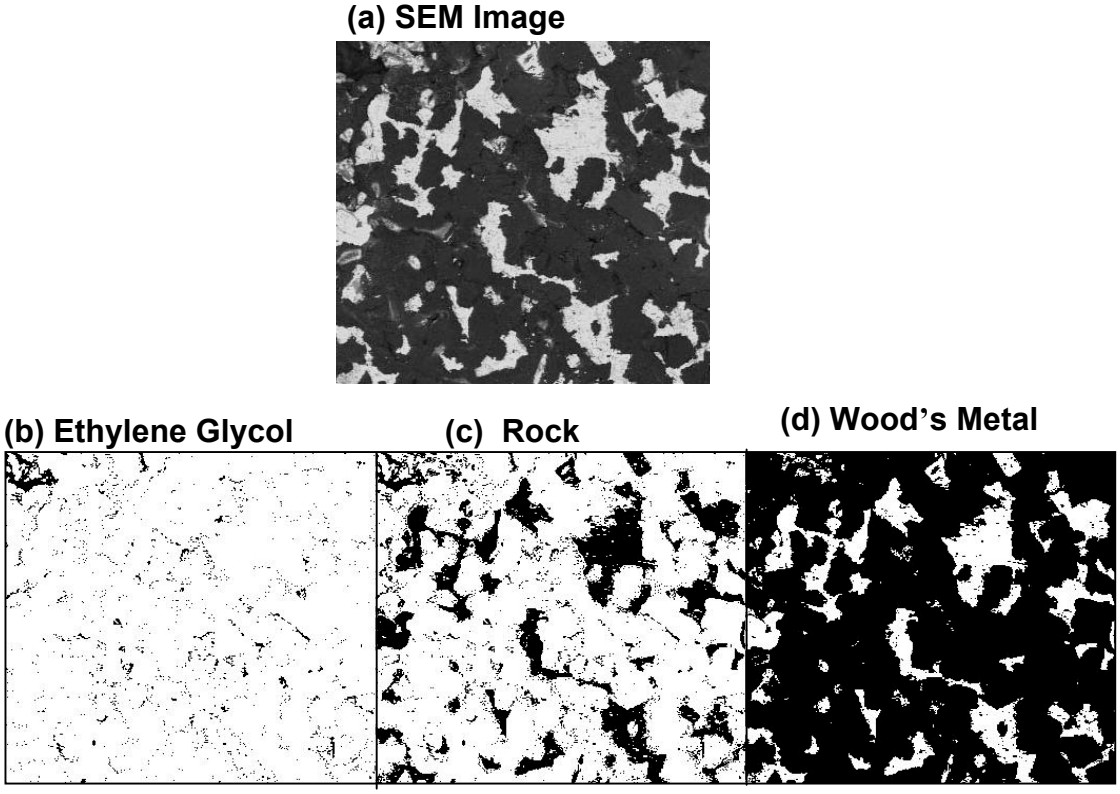

FIGURE 3.3.1 (A) SCANNING ELECTRON MICROGRAPH (SEM) OF SANDSTONE WITH WOOD'S METAL AND ETHYLENE GLYCOL FILLED PORES. (B-D) THRESHOLD IMAGES OF THE IMAGE SHOWN IN (A) WITH BLACK REGIONS REPRESENTING (B) ETHYLENE GLYCOL, (C) SANDSTONE ROCK AND (D) WOOD'S METAL FILLED PORTIONS OF PORES. THE RESOLUTION IS APPROXIMATELY 5.5 MICRONS PER PIXEL. THE REGION SHOWN IS APPROXIMATELY 2.7 MM BY 2.5 MM.

3.3.1 Image Analysis for IAV

Figures 3.3.1 & 3.3.2 contain examples of images from the Scanning Electron Microscope (SEM) that were used to extract saturation and interfacial area per volume from the sandstone experiments. Figure 3.3.2 is a mosaic of SEM images that shows the approximate region analyzed for each face of the SEM sample (see sample preparation section 2.3.1.2). The magnification was selected so that each image contained a representative area, i.e., a porosity that was the same as that measured experimentally.

After acquiring SEM images from the Wood's metal injected sandstone samples at several depths and locations, the images were processed to identify the different phases in the

sample. A custom-developed code was used to threshold the images for each of the phases (Figure 3.3.1). There are three phases (ethylene glycol, rock and Wood's metal). First the saturation and the edge length of each phase, S1, S2, S3, L1, L2, L3 are obtained. Then based on the assumption that each phase contacts either the second or the third phase,

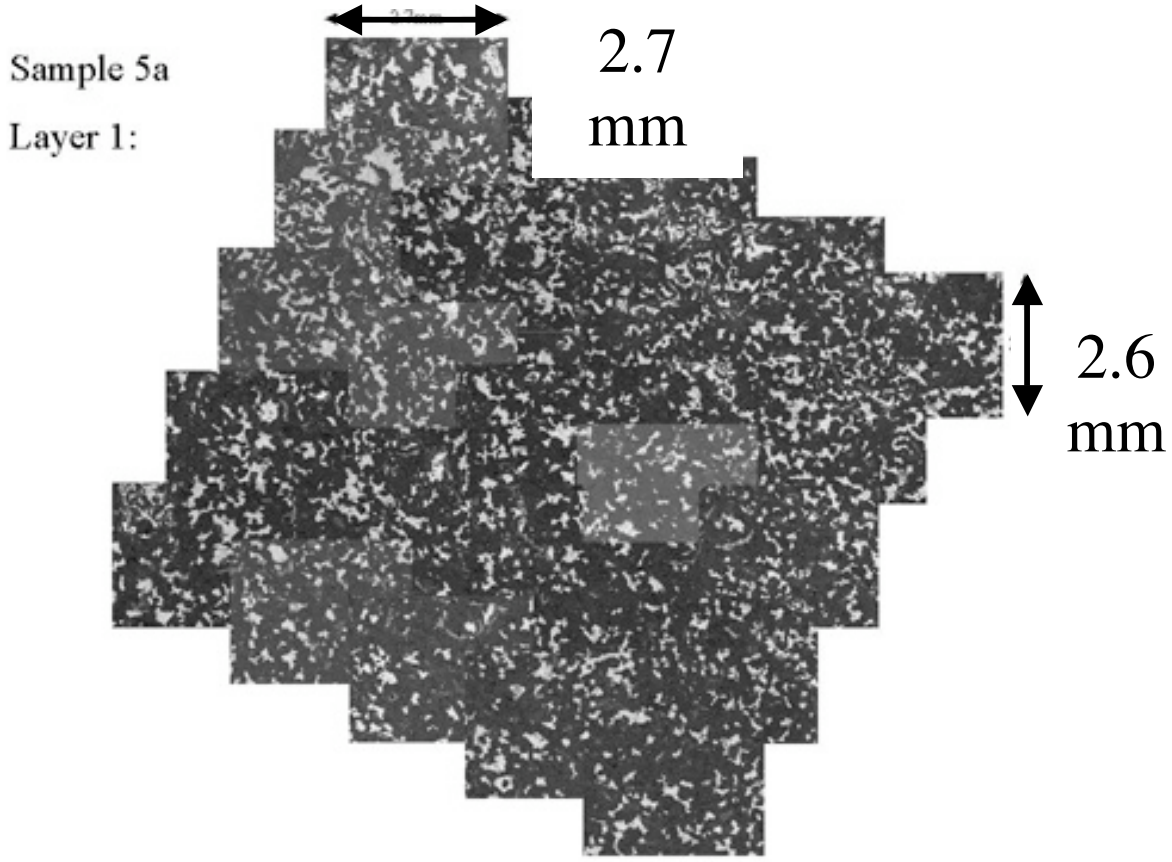

Figure 3.3.2 Mosaic made from 25 SEM images of sample 5a inject with Wood's metal. These images were acquired using the back-scattered electron method described in section 2.3.2 with 67x magnification for a 3.9 micron per pixel resolution.

we can calculate L12, L13, L23, the edge length between every pair of phases following the simple relations:

$$L12=(L1+L2-L3)/2$$
$$L13=(L1+L3-L2)/2$$
$$L23=(L2+L3-L1)/2.$$

The error in the value of edge length from image analysis is 10 percent. In this report, all values of IAV reported for the sandstone samples have an error of 10 percent. The values of area fractions (i.e., porosity or saturation) from image analysis are accurate to within one percent. In the following sections, each value of saturation, porosity and interfacial area is an average value based on the all of the images (~ 40 to 100 images) acquired from the faces of the sample that were perpendicular to the direction of injection.

3.3.2 PRESSURE, SATURATION AND PORE SIZES

Unlike the micro-model experiments (see section 3.2), one Wood's metal experiment and the subsequent image analysis produces one data point for the interfacial area per volume, saturation and capillary pressure curve. In the micro-model experiments, one experiment can produce 100-200 points of data.

We analyzed the images obtained from the samples listed in Table 3.1 and Table 3.2. Table 3.1 and Table 3.2 list the sample name, the porosity of the sample, the injection pressure, and the estimated minimum aperture (pore radius) penetrated by the Wood's metal for the imbibition and drainage experiments, respectively. The porosity of the sample was obtained from image analysis of SEM micrographs. The estimated minimum aperture is based on the surface tension of Wood's metal (480 dynes/cm) and LaPlace's equation ($P_{cap} = \sigma \cos\theta / r$, where P_{cap} is taken to be the injection pressure, σ is the surface tension, θ is the contact angle, and r is the radius of the pore). For the drainage experiments, the sample was initially injected with Wood's metal at a pressure of 0.68 MPa. Then the pressure was lowered (to the injection pressure listed in Table 3.2) which enabled the Wood's metal to drain from the sample. During drainage, as the pressure is lowered, the Wood's metal retracts first from the smallest pores.

Table 3.1. Porosity, injection pressure and estimated minimum pore size penetrated for each sample for imbibition experiments.

Sample number	0	1a	4a	5a	6a	6bs1	6bs3	2bs1	2bs3
Porosity (%)	19.4	20.4	20.6	20.4	19.8	18.3	19.6	18.9	18.9
Injection pressure (MPa)	Zero	0.10	0.17	0.34	0.034	0.016	0.021	0.028	0.69
Minimum pore size penetrated (microns)	Not Appl-icable	4.8	2.8	1.4	14	30	23	17	0.7

Table 3.2. Porosity, injection pressure and estimated minimum pore size penetrated for each sample for drainage experiments.								
Sample number	2bs4	1cs1	1cs2	2cs2	3cs1	3cs2	4cs1	4cs2
Porosity (%)	20.2	20.1	20.7	20.0	20.0	20.0	19.9	21.2
Injection pressure (MPa)	0.34	0.17	0.1	0.034	0.028	0.021	0.014	0.17
Minimum pore size penetrated (microns)	1.7	2.8	4.8	14	17	23	34	2.8

Figure 3.3.3 is a graph of the fraction of pore space saturated with Wood's metal as a function of capillary pressure (i.e., the difference in pressure between the Wood's metal and the ethylene gylcol). Each data point in Figure 3.3.3 corresponds to one sample listed in Table 3.1 (red solid-circles for imbibition) or Table 3.2 (blue open-circles for drainage). There is a sharp transition from the pore space being 10% filled with Wood's metal to being filled with 80% Wood's metal. The difference in pressure between the 10% and 80% saturations of pore space with Wood's metal is 6.9×10^{-3} MPa which corresponds to a 3 micron change in the radius of the pore. Based on the minimum radius of the aperture penetrated, the connectivity of the pore space in the sandstone samples is controlled or dominated by pore throats with radii in the range of 14 microns to 17 microns. Another way to view the pressure versus Wood's metal saturation data is that 80% of the sample's void space is connected when pores with radii greater than 14 microns are penetrated. To achieve 98.6% metal saturation requires that all pores greater than 0.696 microns in radius must be penetrated.

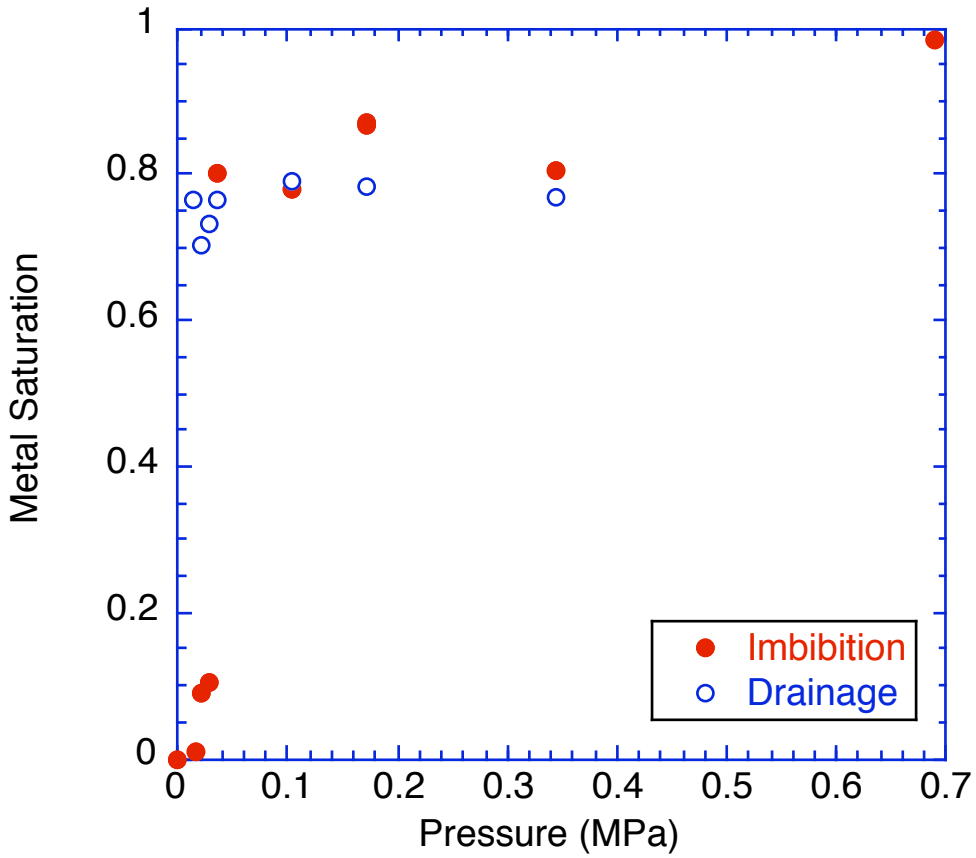

Figure 3.3.3 Fraction of pore space saturated with Wood's metal as a function capillary pressure (i.e., the difference in pressure between the Wood's metal and the ethylene gylcol). The line is shown to guide the eye.

3.3.3 Interfacial Area per Volume for Sandstone

This work represents the first experimental data for interfacial area per volume on real rock, i.e., sandstone. In our case, the images being analyzed are in two dimensions which produces an interfacial length per area. To be consistent with common usage, we will still use IAV (interfacial area per volume) as per the micro-model work (see section 3.2).

For the samples listed Tables 3.1 & 3.2, IAV values were calculated for the interfaces between the wetting and nonwetting phases (IAVwn ethylene glycol and Wood's metal), between the non-wetting phase and the solid (IAVns - Wood's metal and sandstone) and between the wetting phase and solid (IAVws - ethylene glycol and sandstone). The resolution of the SEM micrographs used in the analysis was ranged from 3.9 microns per pixel to 5.5 microns per pixel for a magnifications of 67x to 48x, repsectively. This magnification was chosen so that each image was a representative elementary area, i.e. the porosity measured from the image analysis was consistent with that determined experimentally (on the order of 20% void fraction). Thus, interfaces are only resolved to 3.9 microns to 5.5 microns, unlike the micro-model work (section 3.2) which had a resolution of 0.6 microns per pixel. Our values of IAVwn are therefore under-resolved.

Figures 3.3.4 and 3.3.5 are graphs of IAVns and IAVws as a function of pressure, while Figures 3.3.6 and 3.3.7 are graphs of IAVns and IAVws as a function of wetting phase saturation. Each point in these Figures repesents on sample from either Table 3.1 or Table 3.2. IAVws increases (and IAVns decreases) as a function of wetting phase saturation (Figures 3.3.6 & 3.3.7). IAVws decreases (and IAVns increases) as a function of pressure (Figuresd 3.3.4 & 3.3.5) because as the injection pressure is increased the metal can penetrate into smaller and smaller pore sizes. The value of IAVws is larger than IAVns because the rock had micro-porosity. From SEM images, it is observed that the surfaces of the sandstone grains are pitted, leading to micro-porosity. This micro-porosity appears to be unconnected and is rarely observed to be filled with Wood's metal. Because Wood's metal is never observed in the micro-porosity in the SEM images, IAVns never obtains values as high as IAVws at low pressures. By assuming that the micro-porosity is filled with ethylene gylcol, this increases the values of IAVws at low injection pressures.

A three dimensional surface of the relationship among capillary pressure, saturation and IAVwn was not constructed because the surface would be under-resolved. Instead, we present the data as two-dimensional prohjections of the relationship in Figures 3.3.8-3.3.10. These graphs are the same projections that can be examined for the micro-model work (see section 3.2.4.1). From Figures 3.3.8 & 3.3.9, it can be seen that IAVwn is much smaller in value than IAVns and IAVws, by approximately two orders of magnitude. IAVwn never obtains high values because of the sharp transition in the metal saturation as a function of pressure (Figure 3.3.3). This is an indication that the value of IAVwn is closely linked with the pore geometry and the connectivity of the pore geometry. As described in section 3.3.2, the metal saturation jumped from 10% to 80% in 6.9 x 10^{-3} MPa. If the transition exhibited a smoother slope, IAVwn would increase as the fraction of voids filled with wetting and non-wetting phase approached 50%.

Conceptaully, IAVwn should start out at a low value when the pores are mainly filled with wetting phase (ethylene gylcol) and increase to a maximum value with increasing pressure. After a maximum is reached, IAVwn should begin to decrease as the ethlyene gylcol is displaced from the pore space by the Wood's metal (non-wetting phase) under high pressure. In Figure 3.3.8, the maximum value of IAVwn occurred during drainage as was also observed in the micro-model work.

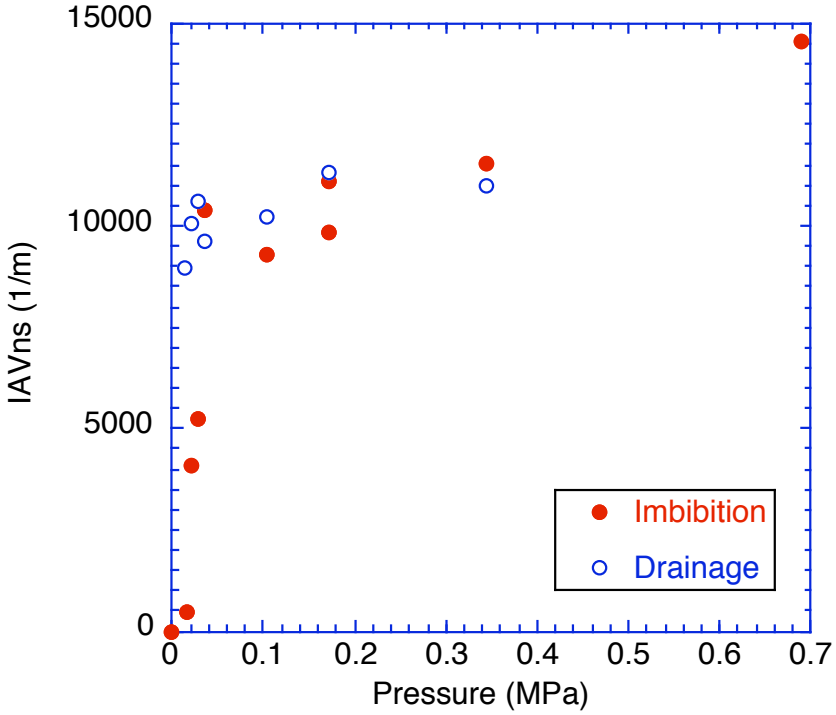

Figure 3.3.4 Interfacial area per volume between the non-wetting phase and the solid as a function of pressure for imbibition (solid cirlces) and drainage (open circles).

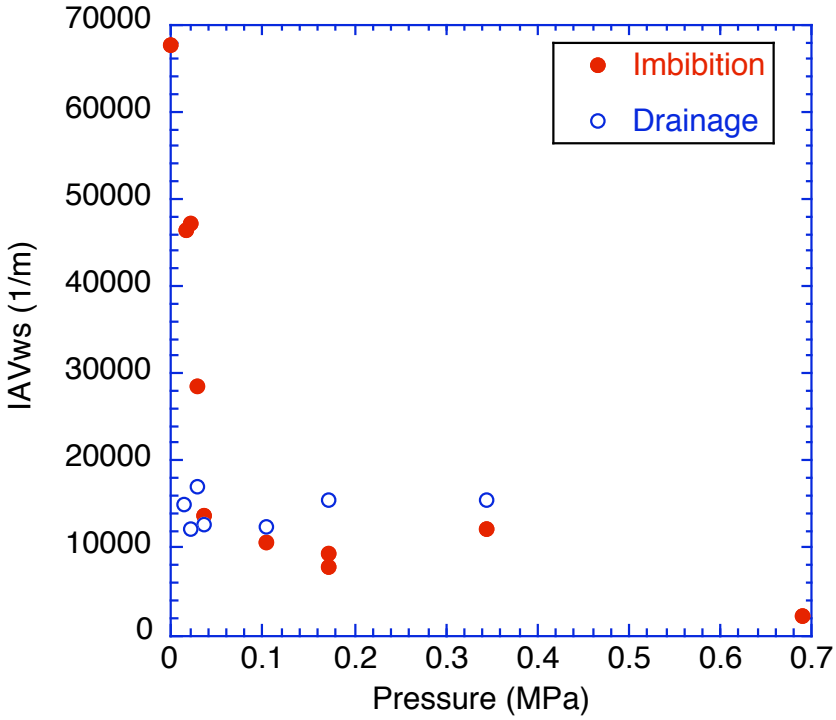

Figure 3.3.5 Interfacial area per volume between the wetting phase and the solid as a function of pressure for imbibition (solid cirlces) and drainage (open circles).

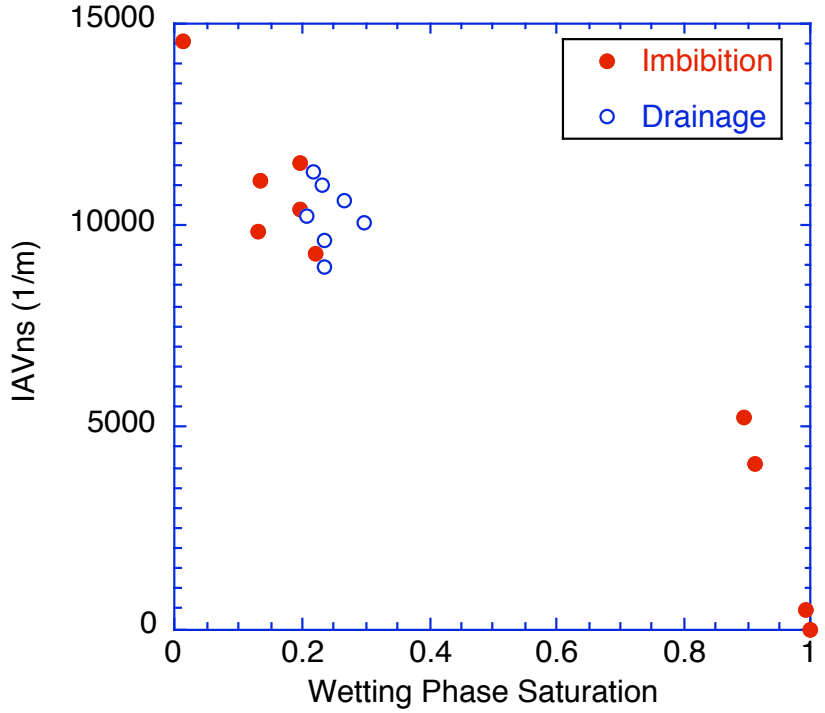

Figure 3.3.6 Interfacial area per volume between the non-wetting phase and the solid as a function of wetting phase saturation for imbibition (solid cirlces) and drainage (open circles).

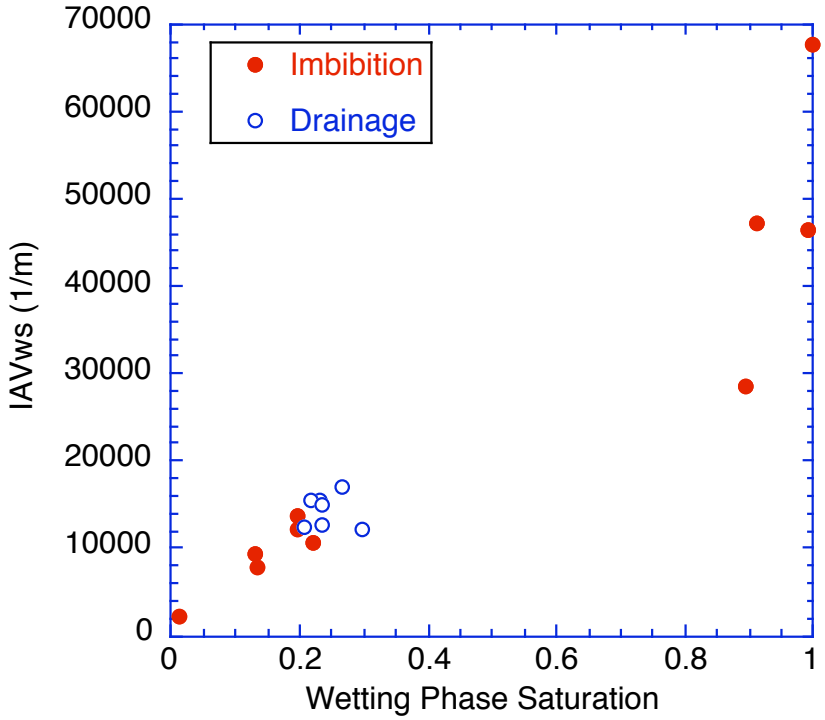

Figure 3.3.7 Interfacial area per volume between the wetting phase and the solid as a function of wetting phase saturation for imbibition (solid cirlces) and drainage (open circles).

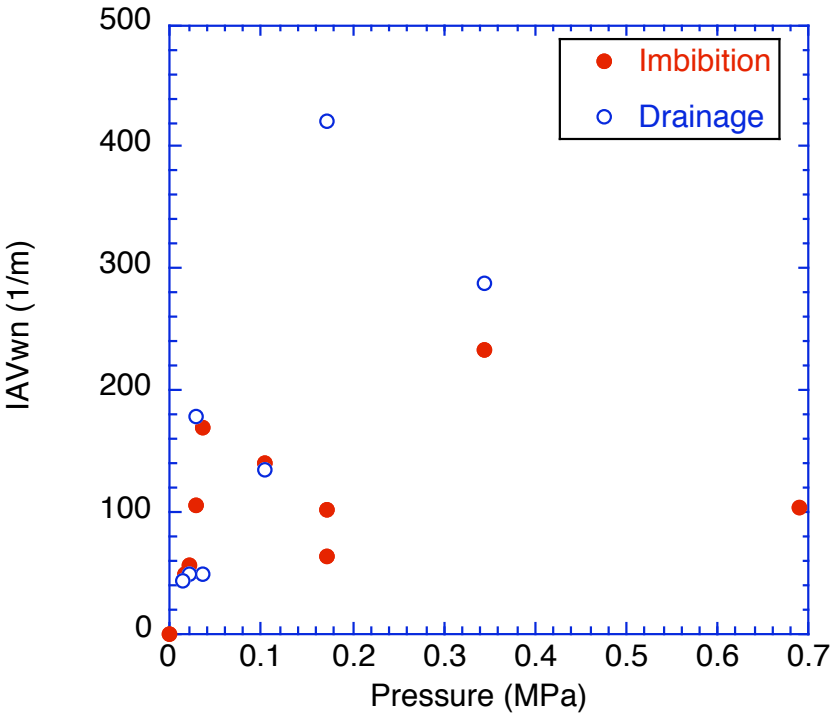

Figure 3.3.8 Interfacial area per volume between the wetting phase and non-wetting phase as a function of pressure for imbibition (solid cirlces) and drainage (open circles).

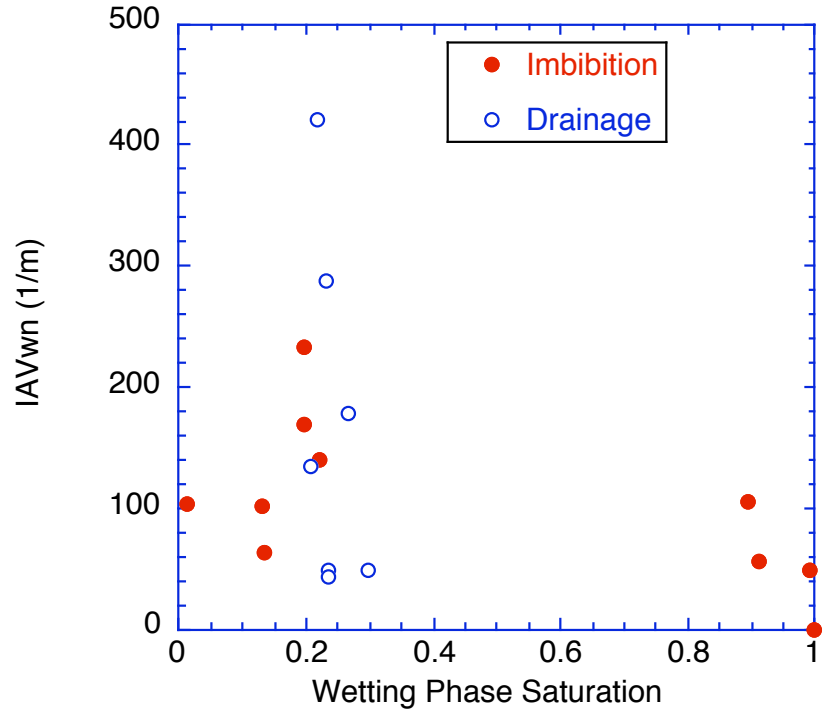

Figure 3.3.9 Interfacial area per volume between the wetting phase and the non-wetting phase as a function of wetting phase saturation for imbibition (solid cirlces) and drainage (open circles).

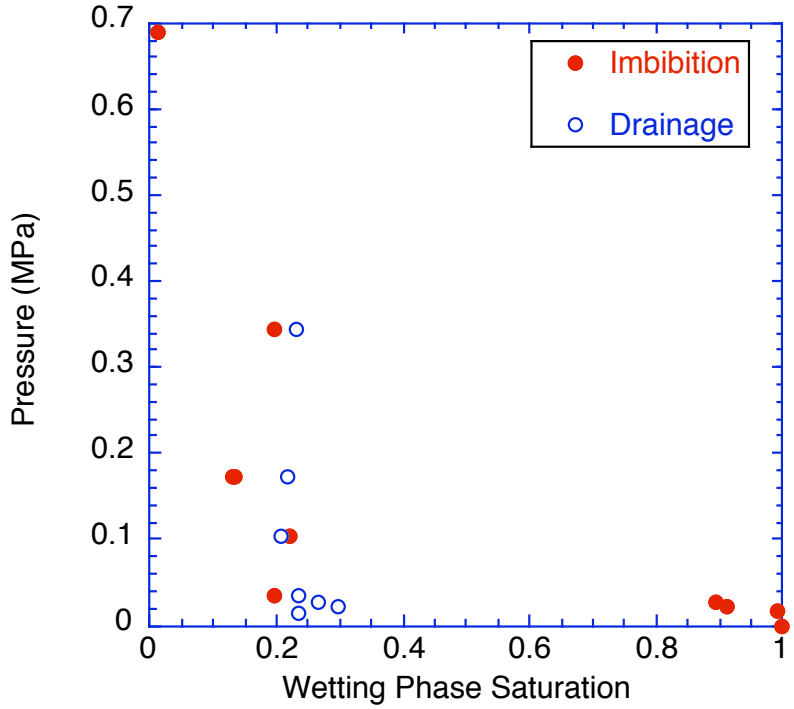

Figure 3.3.10. Pressure as a function of wetting phase saturation for imbibition (solid cirlces) and drainage (open circles).

3.3.4 Comparison of pore/grain size from OCI and Wood's Metal Injection Method Applied to Sandstone.

As described in section 3.1, the pores and grains in OCI images are observed but extracting quantatitive informations proved challenging. At this time, OCI can image into sandstone up to 1 mm and detect the reflected light from grain boundaries. Facet drop-out proved to be major challenge and requires algorithmic developments that are beyond our current capabilities. However, by performing statistical analyses on the datasets (see section 3.1.4) average grain size and average pore size were extracted. The statistical analysis involved auto-correlation and cross-correlation analyses on three-dmensional datasets taken when the samples were in a wet condition and in a dry condition. From this, the average pore size from OCI imaging was obtained to be ~180 microns. (section 3.1.4.2) and grain sizes were extracted to be in the range of 100 microns-200 microns (section 3.1.4.1 & 3.1.5). SEM analysis performed in conjunction with OCI (Figure 3.1.4 in section 3.1.1) also found that the grain scale was on the order of 100 microns.

We used image analysis to extract the pore size from images of sandstone. An autocorrelation analysis was performed on an SEM image from a sample fully-saturated with Wood's metal. Figure 3.3.11 shows the SEM image as well as an image of the two-dimensional autocorrelation function of the SEM image. The magnification of the image is 48x and was chosen so the image would represent an elementary area, i.e., a porosity that matched the measured data. The value of the auto-correlation function at the center (Figure 3.3.12) is 0.195 (19.5%) which is approximately the measured value of the porosity of this

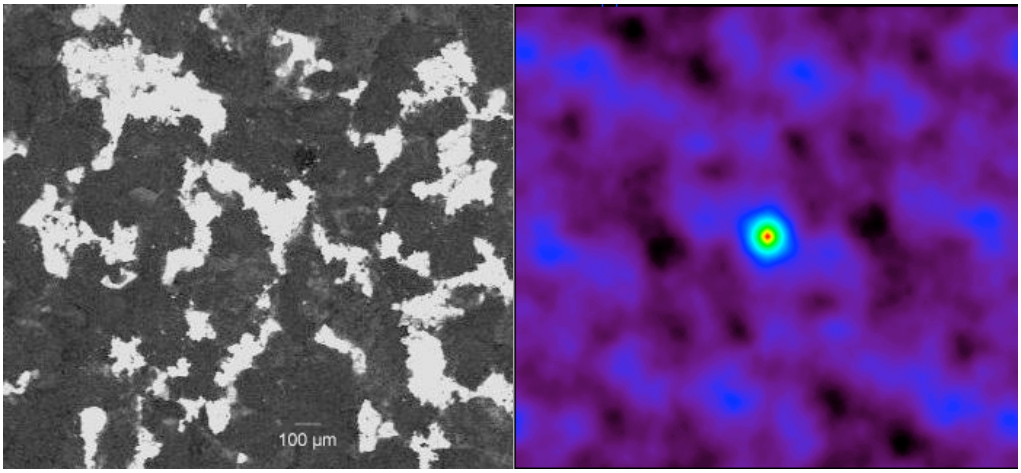

Figure 3.3.11 On the left is an SEM image from a sample saturated with Wood's metal. On the right is the two-dimensional autocorrelation function for the SEM image on the left.

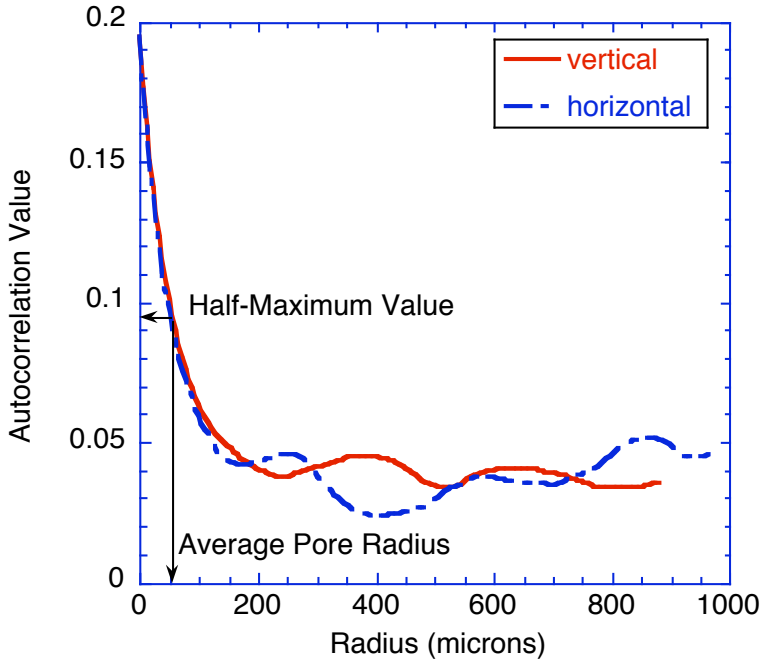

Figure 3.3.12 Autocorrelation curves takend from center of the two-dimensional autocorrelation function shown in Figure 3.3.11 for the vertical direction and horizontal. Only half ot the curve is graphed. The average pore diameter (~110 microns) is estimated from the value of the radius at half the maximum value of the autocorrelation function.

core. The central peak of the autocorrelation function is fairly isotropic though the banding in the image indicates the pores spacing. By taking slices through the autocorrelation (Figure 3.3.12), the average pore radius of the Wood's metal pores can be determined by taking the value of the radius at half the maximum value of the autocorrelation function. The average pore diameter obtained in this manner is approximately ~110 microns. The spacing between the pores can be estimated from the distance between the oscillation in the autocorrelation curves. The spacing is approximately 200 μm to 300 μm between the center of the pores. This spacing cannot be taken as the grain size because between each pores there are often several grains. Examination of the SEM images finds the grain size to be on the order of 100 -200 microns. Thus, OCI was successful at extracting the average grain size and the average pore size from statistical analyses.

3.3.5 Comparison of Interfacial Area per Volume from the Micro-Models and from Sandstone.

Multiphase flow through sandstone is a three-dimensional problem because it is the third dimension that enables the connection of pores to form a flow path. A challenge of this project was to compare the IAV results from the two-dimensional (2-D) micro-models to the IAV results from the three-dimensional (3-D) sandstone cores. There is no known rigorous formalism for scaling between different dimensionalities. We linked the 2-D and 3-D information in an approximate manner using a percolation approach.

The percolation threshold P_c is the concentration of open pore space at which a fully connected open region that spans the entire sample is first formed. Flow is only possible when the concentration of open pore space P is greater than or equal to P_c. The value of P_c depends on the dimensionality and structure of the system. Since the micro-models are 2D while sandstone is 3D it is not meaningful to compare the two at the same value of P. It makes more sense to compare the two types of samples if they have the same value of P- P_c , since they are then the same distance from P_c , i.e., the same distance from the onset for flow.

In a 3D close packed structure (as appropriate for sandstone) the theoretical value is P_c = 0.18 (Stauffer, 1984). The porosity of the sandstone was measured experimentally using the wet/dry method. In the wet/dry method, the sample is vacuum saturated and the weight difference before and after saturation is used to calculate the porosity. The porosity of sixteen sandstone samples was approximately 19.25% $\pm$ 0.11%, which is confirmed by the measurements from image analysis (See Tables 3.1 & 3.2 in section 3.3). Hence they are approximately 1% above the percolation threshold. We therefore constructed our micro-models to have P- P_c = 0.01. We first determined P_c by making a series of samples of different P using the one tier fractal geometries described by Nolte and Pyrak-Nolte (1991), and measuring the value of P at which flow first appeared. The measured value of P_c was 0.51 $\pm$ 0.01 which is very close to the expected value of 0.50 (Stauffer, 1984).

Figure 3.3.13 is a bar chart comparing the maximum measured values of IAVwn, IAVns and IAVws for the two micro-model patterns described in section 3.2 and the sandstone. For both micro-models and the sandstone, IAVws is larger than IAVns. The maximum value of IAVws is a measure of the total surface area of the void space, i.e. specific surface area. The maximum value of IAVns should be equal to that of IAVws but the micro-models and the

sandstone samples were never 100% saturated with the non-wetting phase. The difference between the maximum values for IAVns and IAVws reflect trapped regions or undisplaced regions of wetting phase in the micro-models, and micro-porosity in the sandstone. Our percolation approach to link the micro-models to a physical parameter of the sandstone (i.e., the percolation threshold) appears to be a reasonable choice as the IAVws is roughly similar.

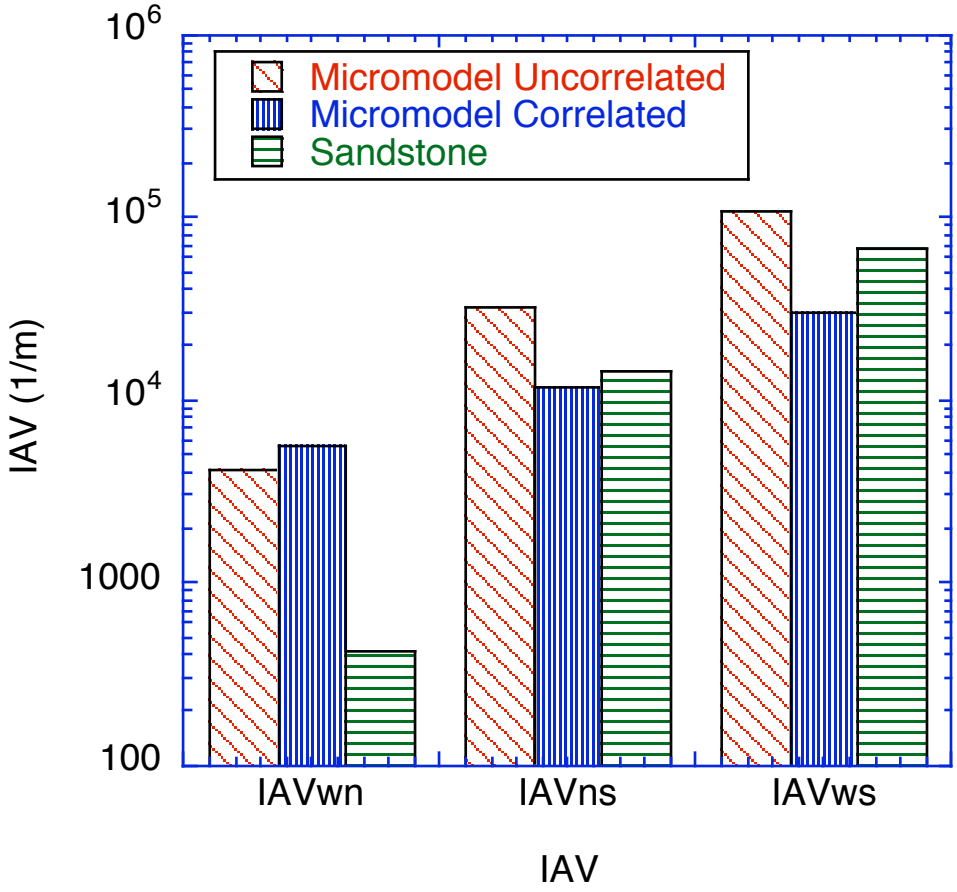

Figure 3.1.13. Comparison of IAV mesaured for the micro-models and the sandstone samples.

However, the IAVwn (between the wetting and non-wetting phase) is roughly two-orders of magnitude smaller for the sandstone samples than the micro-models. So, while the percolation threshold approach captured the total pore length, IAVwn is dominated by connectivity. The sandstone samples exhibited a sharp transition in the pressure versus saturation (Figure 3.3.3) compared with the behavior observed in the micro-models (Figures 3.2.4 & 3.2.5). The flow paths in the sandstone samples have an average critical neck or critical throat size that is between 28 microns to 34 microns in diameter. When these critical throats were penetrated, the pores in the sample were 80% connected. In the micro-models, the saturation changed more smoothly. Future work would need to include a connectivity parameter to link the properties of the two-dimensional and three-dimensional work.

4.0 Conclusions and Future Work

This project on the experimental investigation of relative permeability upscaling has produced a unique combination of three quite different technical approaches to the upscaling problem of obtaining pore-related microscopic properties and using them to predict macroscopic behavior. Several important "firsts" have been achieved during the course of the project. 1) Optical coherence imaging, a laser-based ranging and imaging technique, has produced the first images of grain and pore structure up to 1 mm beneath the surface of the sandstone. 2) Woods metal injection has connected for the first time microscopic pore-scale geometric measurements with macroscopic saturation in real sandstone cores. 3) The micro-model technique has produced the first invertible relationship between saturation and capillary pressure—showing that interfacial area per volume (IAV) provides the linking parameter. IAV is a key element in upscaling theories, so this experimental finding may represent the most important result of this project, with wide ramifications for predictions of fluid behavior in porous media. Furthermore, these three significant findings are reinforced by comparison among each other.

In the following sections, we present technological assessment and potential future directions of this work.

4.1 Optical Coherence Imaging

Table 4.1 is a comparison of OCI to other downhole imaging technologies. This table indicates the advantages and disadvantages of each technique. From our study, we have reached the following conclusions about OCI as a viable method for imaging pore/grains in sandstone:

(a) Volumetric data of grains and pores in sandstone can be constructed from xy frames at successive depths. Coherent laser ranging can penetrate up to 1 mm into sandstone.
(b) Only grain facets that are oriented approximately perpendicular to the probe axis are visible. This makes grain/pore identification/reconstruction complicated.
(c) Voids can be differentiated from grains by comparing wet sandstone to dry. But facet drop-out still makes specific identification of grains and pores complicated.
(d) The difficulty in identifying whole grains, because of facet dropout complicates the analysis of OCI data.
(e) Statistical analysis of OCI data *does* provide average or most probable pore size and grain size.
(f) Point-scan data (one-dimensional signal) are easy to interpret but volumetric data (in two- or three- dimensional form) proves to be more challenging. Future work requires the development of topological or statistics-based algorithms and tools for using wet/dry stretching images and performing facet reconstruction to get three-dimensional grain/pore structure. This aspect of the work is the most challenging future development.
(g) Borehole data from a borescope was obtained as a point-scan without images and interpretation of point-scan (A-scan) data is simple. It is easy to pick out the reflections from the interfaces. However, the limitation of point scanning is time. If time is not an issue this is a feasible method for borehole logging.

(h) OCI full-frme iamges were obtained in a borehole in the laboratory. OCI is possible in a borehole provided the borehole is large enough to fit the necessary equipment.

Table 4.1 Comparison of competing technologies with Optical Coherence Imaging (OCI).

Technology	Advantages	Disadvantages
Optical Coherence Imaging	- penetrates turbid water - ~10 micron resolution - penetrates ~ millimeter	- complicated optics
Down-hole Video	- direct imaging	- only shows surface of borehole - no penetration in drilling mud
Neutron Logger	-deep penetration	- non-imaging - sensitive only to density
Ultrasound Methods	- deep penetration	- resolution ~ millimeter - need to scan to get images - provides moduli information not just pores

4.2 Micro-Models

Table 4.2 give a comparison of other micro-model techniques that could be used to address the issues of IAV in porous medium. However, it is our conclusion that the photolithographic technique provided high-quality micro-models with well-known geometry. The micro-model study proved the theoretical hypothesis that IAV is an important parameter in understanding the capillary pressure-saturation relationship. Saturation provides an indication of how much fluid is in a sample. Interfacial area per volume indicates how the fluids are distributed within a pore medium. The micro-model provided direct images of how interfacial structure is linked to the imbibition and drainage process. In comparing the micro-model results with the sandstone samples, we found we could match total pore area between our two-dimensional and three-dimensional systems. However, the comparison showed that the connectivity of the pore size distribution plays a key role in determining the final values of interfacial area between the wetting and non-wetting phases.

Future directions for the this work include:

(a) To determine if an ensemble-averaged relationship among capillary pressure, saturation and interfacial area per volume may be universal for statistically similar pore distributions. We found that the values of IAV differed depending on the spatial correlations of the pore structure. If no universal relationship can be found, this would require measurement of IAV for all pore structures of interest (i.e., all rocks).

Table 4.2 Comparison of Photolithographic micro-models and other micro-model technology.		
Technology	Advantages	Disadvantages
Photolithographic Micro-Models	- high resolution ~0.6 micron/pixel - precise channel geometry - direct imaging of IAV and saturation	- two-dimensional -three-dimensional structures difficult or impossible
Micro-Models in Glass	- good for studying fingering - good for studying saturation of multiple fluid phases	- rough channels with roughness not measured - no measurements of IAV - low resolution
Shower Door Glass Models	- inexpensive	- poor calibration to light transmission - no distribution information - no measurements of IAV

(b) To quantify the relationship between interfacial geometry, saturation and relative permeability for steady-state flow conditions. The displacement-technique used with the micro-models quantified the relationship among capillary pressure, saturation and interfacial area per volume. The link between IAV and relative permeability needs to be established experimentally.

(c) To determine if the relaxation coefficient associated with dynamic flow conditions depends on the evolution of the interfacial geometry with time. All our measurements were performed at equilibrium. It needs to be established experimentally what role, if any, IAV has in dynamic behavior of multiphase flow.

4.3 Wood's Metal Method

Table 4.3 lists the advantages and disadvantages of the Wood's metal method for studying interfacial area per volume in real systems, i.e. rock. The IAV results obtained with the Wood's metal injection technique are the *first data* of this type acquired on any rock. The drawback of the technique is the destructive nature of obtaining the images. The uniqueness of the IAV, capillary pressure and saturation relationship for sandstone cannot be determined because sixteen samples is not enough to construct a surface. However, by comparing the micro-model results and the sandstone results, we conjecture that the essential features of the sandstone pore geometry can be captured by the micro-models if we designed the micro-models to have the same connectivity parameter.

Table 4.3 Comparison of Wood's metal injection method to other laboratory techniques.

Technology	Advantages	Disadvantages
Wood's metal injection	- high resolution images through Scanning Electron Microscopy ~ 5 microns	- destructive sampling
Advanced Photon Source Imaging	-non-destructive imaging	-trade-off in resolution versus sample size -image reconstruction issues
Neutron Source	-good for saturation	-no distribution information - no IAV

5.0 References

Bear, J., 1979, Hydraulics of Groundwater, McGraw-Hill, New York.

Bradford, S. A. and F. J. Leij, 1997, Estimating interfacial areas for multi-fluid soil systems, Journal of Contaminant Hydrology, 27, p83-105.

Cheng, J.-T., L. J. Pyrak-Nolte, D. D. Nolte and N. J. Giordano,2004, Linking Pressure and Saturation through Interfacial Areas in Porous Media, Geophysical Research Letters, in press.

Darcy, H., Determination of the laws of flow through sane, Les fontaines publiques de la ville de Dijon, Victor Dalmont, Paris, 1856, 590-594, (translated and reprinted in Physical Hydrology, edited by R. A. Freeze and W. Back, Hutchinson Ross Publishing Company, Stroudsburg, PA, 1983).

Deriagin, Boris Vladimirovich, Churaev, N. V., Muller, V. M., Kitchener, J. A., 1987, Surface Forces, English translation, New York, Consultants Bureau.

Dullien, F. A. L., 1992, Porous Media; Fluid Transport and Pore Structure, Academic, San Diego, Calif.

Gray, W. G., General conservation equations for multi-phase systems: 4. Constituitive theory including phase change, Adv. Water Resources **6**, 130-140 (1983).

Gray, W. G. and S. M. Hassanizadeh, 1998, Averaging theorems and averaged equations for transport of interface properties in multiphase systems, International Journal of Multiphase Flow, 15, 81-95.

Gray, W. G. and S. M. Hassanizadeh, 1991, Unsaturated flow theory including interfacial phenomena, Water Resources Research, 27(8), 1855-1863.

Gray, W. G. and S. M. Hassanizadeh, 1998, Macroscale continuum mechanics for multiphase porous-media flow including phases, interfaces, common lines and common points, Advances in Water Res., 21, 261-281.14. Gvirtzman H. and P. V. Roberts, 1991, Pore scale spatial analysis of two immiscible fluids in porous media, Water Resources Research, v. 27, no 6, p 1165-1176.

Hassanizadeh, S. M. and W. G. Gray, General conservation equations for multi-phase systems: 1. Averaging procedure, Adv. Water Resources **2**, 131-144 (1979).

Hassanizadeh, S. M. and W. G. Gray, 1990, Mechanics and thermodynamics of multiphase flow in porous media including interphase boundaries, Water Resources Research, 13, 169-186.

Muccino, J. C., W. G. Gray, and L. A. Ferrand, 1998, Toward and improved understanding of multiphase flow in porous media, Rev. Geophys, 36, 401-422.

Nolte, D. D. ,"Photorefractive Effects and Materials,", (Kluwer Academic Publishers, Dordrecht, 1995).

Nolte, D.D, and L. J. Pyrak-Nolte, Stratified continuum percolation: Scaling geometry of hierarchical cascades, Phys. Rev. A **44**, 6320 (1991).

Powers, S. E., Loureiro, C. O., Abriola, L. M. and W.. J. Weber, Jr., 1991, Theoretical study of the significance of nonequilibrium dissolution of nonaqueous phase liquids in subsurface systems, Water Resources Research, v. 27, n 4, p463-477.

Rapoport, L. A. and W. J. Leas, 1951, Relative permeability to liquid in lquid-gas systems, Petroleum Transactions, v. 192, p83-98.

Reeves, P. C. and M. A. Celia, A functional relationship between capillary pressure, saturation, and interfacial area as revealed by a pore-scale network model, Water Resource Research **32**, 2345 (1996).

Shipley Microelectronic Product Guide, Shipley Co., Newton, MA, 1982

Stauffer, D., 1984, Introduction to Percolation Theory, Bristol, PA: Taylor and Francis.

Thompson, L.F., C.G. Willson, and M.J. Bowden, Introduction to Microlithography, 2nd edition, American Chemical Society, Washington, DC, 1994